Dissertation
submitted to the
Combined Faculties of the Natural Sciences and Mathematics
of the Ruperto-Carola-University of Heidelberg. Germany
for the degree of
Doctor of Natural Sciences

Put forward by
Raúl Esteban Domínguez Figueroa
born in: Santiago, Chile
Oral examination: 23 November 2022

Embedded star clusters surviving gas expulsion with low star formation efficiencies.

Referees:

Prof. Dr. Ralf S. Klessen

Priv. Doz. Dr. Geneviève Parmentier

First edition, September 2022

This PhD thesis has been carried out by Raúl Esteban Domínguez Figueroa under the supervision of Prof. Dr. Ralf S. Klessen at Institut für Theoretische Astrophysik, Zentrum für Astronomie der Universität Heidelberg.
Printed and/or published with the support of the German Academic Exchange Service.

Abstract

Star clusters which are about to or have finished the process of star formation are commonly found still immersed in their natal gas clouds. This coexistence is known as embedded star clusters. During this state, the stars are continuously injecting energy to the surrounding gas due to feedback processes such as ultraviolet radiation and massive stellar winds from OB stars, or supernovae explosions which will eventually remove the natal gas. The bare star clusters expand, which in most cases, can lead to their complete dissolution.

Observations and simulations agree about the strong effect that gas gravitational potential removal produces on the dynamics of the stars. However, recent observations of massive young bound star clusters challenge the idea that most embedded star clusters do not overcome the gas expulsion phase.

In this thesis, we study the outcome of the interaction between stars and gas for different star cluster masses. By means of N-body simulations we explore several combinations of initial conditions. We let the simulated star clusters evolve until the moment when all the gas has been pushed away. We characterise the star remnants either by quantifying them by the bound fraction or by comparing their radial expansion with destroyed star clusters.

Zusammenfassung

Sternhaufen, die kurz vor dem Ende ihrer sternenbildenden Phase stehen oder diese bereits abgeschlossen haben, sind häufig noch von ihrer ursprüngliche Gaswolke umgeben. Sie werden dann als eingebetteter Sternhaufen bezeichnet. Durch Rückkopplungsprozesse wie ultraviolette Strahlung und massereiche stellare Winde von OB-Sternen oder Supernovae-Explosionen, führen die Sterne dem umgebenden Gas kontinuierlich Energie zu. Hierdurch wird das ursprüngliche Gas letztendlich entfernt. Die nackte Sternhaufen dehnen sich aus, was in manchen Fällen zu ihrer vollständigen Auflösung führen kann.

Beobachtungen und Simulationen zeigen übereinstimmend, dass das Entfernen des Gravitationspotenzials des Gases einen starken Einfluss auf die Dynamik der Sterne hat. Dennoch wurden in jüngster Zeit massereiche junge gebundene Sternhaufen beobachtet. Dies stellt die Hypothese in Frage, dass die meisten eingebetteten Sternhaufen diese Phase des Abstreifens von Gas nicht überleben.

In dieser Arbeit untersuchen wir das Ergebnis der Wechselwirkung zwischen Sternen und Gas für unterschiedliche Sternmassen. Mit Hilfe von N-body Simulationen untersuchen wir verschiedene Kombinationen von Anfangsbedingungen. Wir lassen die simulierten Sternenhaufen sich entwickeln bis das gesamte Gas verdrängt worden ist. Wir charakterisieren die Sternüberreste, indem wir sie entweder durch den gebundenen Anteil quantifizieren oder ihre radiale Ausdehnung mit zerstörten Sternhaufen vergleichen.

PUBLICATIONS

The following first author's publications are used in this thesis:

Domínguez, R., Farias, J. P., Fellhauer, M., Klessen R. S., 2021, "Are hierarchically formed embedded star clusters surviving gas expulsion depending on their initial conditions?". In MNRAS, 508, 5410

Domínguez R., Pellegrini E. W., Klessen R. S., Rahner D., 2022, "Discovery of self-consistent survival of low star-formation efficiency clusters in evolving clouds: The coupling NBODY6 and WARPFIELD ". In MNRAS (submitted).

Domínguez R., Pellegrini E. W., Klessen R. S., Rahner D., 2022, "30 Doradus, the double stellar birth scenario by N -body & WARPFIELD clouds". In MNRAS (submitted).

Contents

List of figures

List of tables

1 Introduction

The thesis consists of five chapters. The first chapter serves as an introduction to the classical hypothesis of star clusters' life evolution. We continue in chapter 2 and 3 with two studies aiming to improve the understanding of how embedded star clusters can survive after destroying their molecular clouds. As we apply different approaches, we explain the respective methods in each chapter. We continue in chapter 4 with an observational test of the code framework developed in chapter 3. We finalize in chapter 5 with a global summary and future work.

1.1 Star clusters

Young star clusters are usually found embedded in molecular clouds from which they were recently born (see e.g.. Lada and Lada 2003; Gutermuth et al. 2009). They are usually characterized by their values of the instantaneous star formation efficiency (ϵ_{SF}), which means the fraction of gas that is converted into stars:

$$\epsilon_{SF} = \frac{M_{\text{stars}}}{M_{\text{stars}} + M_{\text{cloud}}}, \tag{1.1}$$

where M_{stars} is the total mass of stars and M_{cloud} is the mass of the gas remaining in the embedded star cluster. Observations has measured values of ϵ_{SF} smaller than 0.30 (Lada and Lada 2003). After stars are formed, the gas and the stellar component do not remain together for long, the surrounded cloud is expelled by the combination of ultraviolet radiation, massive stellar winds from OB stars, jets from low mass stars. In the case of ineffective early feedback, supernovae (SNe) explosions will also play a role as massive stars die. As a result of gas expulsion, stars rapidly find a lack of gravitational potential, as the outgoing gas carries

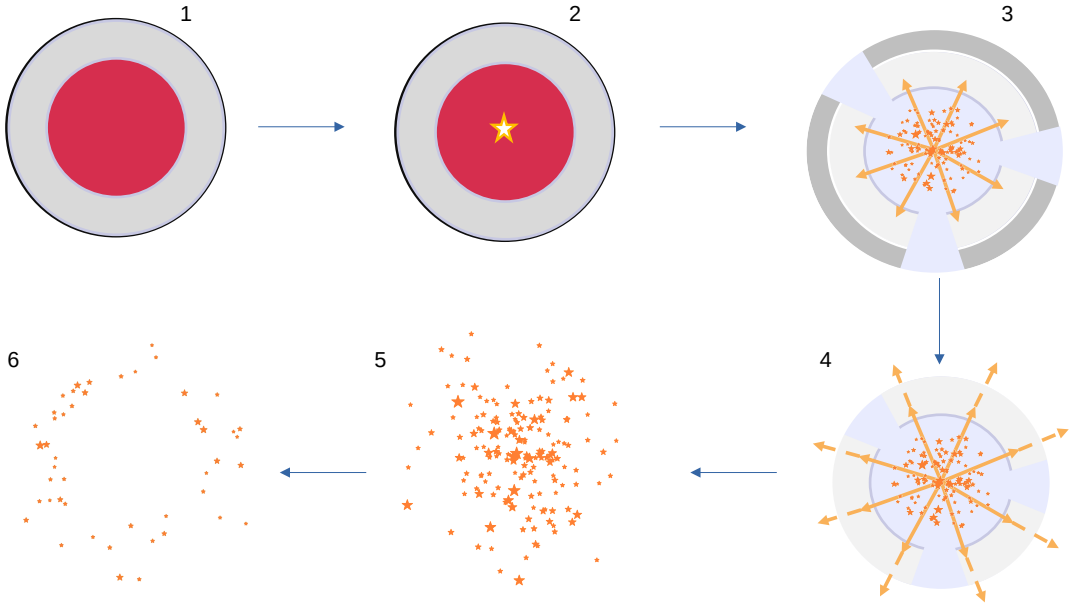

Figure 1.1.1: Life cycle sketch of an embedded star cluster as classical the picture describes.

it away, becoming supervirial, which is leading to its future dissolution into the field. The process is sketched in Fig. 1.1.1. At left top (phase 1), we show a molecular cloud which has reached enough density to start to form stars as top center figure shows (phase 2). The star formation process occurs along the cloud and the stars continuously push out the surrounding gas as top right (phase 3) and bottom right (phase 4) figures show. The cloud expansion continues until a bare expanding cluster is left which can lead to its possible dissolution as we show in bottom center (phase 5) and bottom left (phase 6) figures.

1.2 Classical picture

The question of how clusters can or cannot survive gas expulsion is still under exploration, despite a long history of studies and the exact lower limit of ϵ_{SF} where an embedded star cluster can survive after instantaneous gas expulsion is not clear. After consecutive studies, the limit has been changing and decreasing. Hills (1980) found a $\epsilon_{SF} = 0.5$ from virial theorem. Later in time, Baumgardt and Kroupa (2007) taking advantage of computer improvements developed a grid of N-body simulations showing that if gas expulsion happens instantly, e.g., by a SNe explosion, only star clusters with global ϵ_{SF} higher than 0.33 can retain a fraction of bound stars after the gas is gone (see e.g.. Tutukov 1978; Hills 1980; Margulis et al. 1984; Goodwin 1997; Adams 2000; Geyer and Burkert 2001; Boily and Kroupa 2003a,b; Fellhauer and Kroupa 2005; Bastian and Goodwin 2006; Baumgardt and Kroupa 2007; Brinkmann et al. 2017; Shukirgaliyev et al. 2017, 2018, 2020).

We show in Fig. 1.2.1 the ϵ_{SF} ranges covered by Hills (1980) (blue line) and Baumgardt

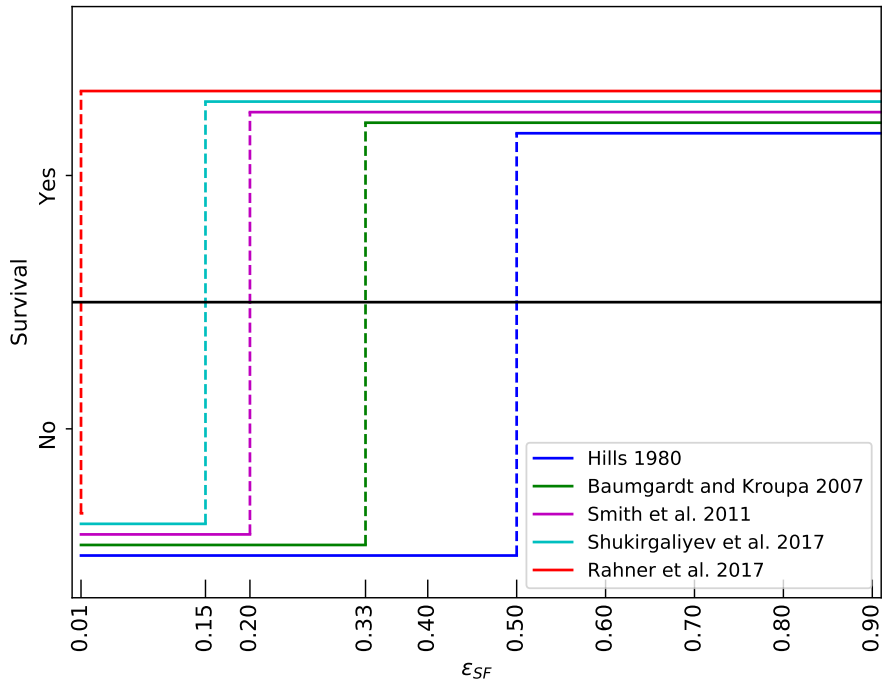

Figure 1.2.1: Summary of different minimum ϵ_{SF} values where embedded star clusters can overcome the violent instantaneous gas expulsion found in different studies.

and Kroupa (2007) (green line).

1.3 Posterior studies

Latter studies have slightly varied this method by exploring different initial conditions and found that embedded star clusters can also survive with lower values of ϵ_{SF}. Instead of starting with spherical stellar distributions, (Smith et al. 2011; Lee and Goodwin 2016; Farias et al. 2017, 2018a) used substructured (fractal) stellar distributions and a value of $\epsilon_{SF} = 0.2$ was found, represented with a magenta line in Fig. 1.2.1. The minimum ϵ_{SF} value went even lower down to $\epsilon_{SF} = 0.15$ (Shukirgaliyev et al. 2017) with a shallower gas density profile (Parmentier and Pfalzner 2013), represented with cyan line in Fig. 1.2.1. It is important to highlight that most of the referred studies were designed to emulate an extreme scenario, in which the gas is violently and immediately expelled. Survivability at low limits can be improved if the gas is removed slower where the embedded star clusters can respond to the change in the potential with more time to exchange internal energy, thus surviving longer.

1.4 WARPFIELD

The classical picture has shown that with simplistic approaches is possible to disentangle different parts of the wide parameter space of initial conditions in affordable CPU-time. More realistic simulations which account for each feedback process in detail are expensive. A recent approach to this problem has been proposed by Wall et al. (2019), where they use the AMUSE framework (Pelupessy et al. 2013) to coupled the magneto-hydrodynamics code FLASH (Fryxell et al. 2000) with the N-body code ph4 (McMillan et al. 2012). They focused their study on examining the binary population formed from the core or disk fragmentation. Besides that result, it is possible to use this framework to follow more accurately the pre- and post-evolution of the molecular cloud and stars formed out but using much larger amounts of CPU-time.

Rahner et al. (2017) introduced the code WARPFIELD (Winds And Radiation Pressure: Feedback Induced Expansion, colLapse and Dissolution), which is based on a semi-analytic 1D model for isolated massive clouds with mass $\gtrsim 10^5$ M$_\odot$. This approach is able to follow the dynamics and structure of the expanding molecular clouds due to winds, SNe, and radiation pressure or, if it is the case, the collapse of a molecular cloud when the feedback is not enough to keep it expanding. It is possible to explore a large range of parameters of ϵ_{SF}, initial cloud density, and metallicity in a reasonable quantity of CPU time. The treatments of the thermal evolution of the gas were improved in version 2 (Rahner et al. 2019), which we use in this thesis.

In existing studies which follow closely the classical picture, stellar feedback is often assumed to be strong enough to completely disrupt the molecular cloud and consequently avoid any further star formation (Murray 2011; Wang et al. 2010). Another possible scenario is positive feedback. Here, injected energy is forcing the cloud to expand, while higher pressures also lead to an increase in the density resulting in the cloud to collapse and trigger another star birth event (Koenig et al. 2012). We sketch this scenario in Fig. 1.4.1 starting from phase number 4. Phases 1, 2 and 3 are occurring as we have previously described in Sec. 1.2. The collapsing cloud is shown in phases 4 to 6 until the new star formation event is occurring. From phase 7 to 9 the molecular cloud expand to the ISM as consequence of the feedback generated by the stars, in this case, by the two stellar generations. WARPFIELD allows to have more than two star formations events if the feedback of the complete star cluster is not enough to disrupt the surrounded gas.

For a long time it was thought that stellar multiples generations were limited to globular clusters as they are largely found in these relics of the Universe, but multiples generations have also been observed in young star clusters. For example, Sandage-96 shows a bi-modal age separation of at least 10 Myr (Palla et al. 2005, 2007; Vinkó et al. 2009) or even smaller than 1 Myr in the Orion nebula cluster (Beccari et al. 2017) with three generations. Another example is 30 Doradus where the older population in NGC 2070 seems to fail to take apart its molecular cloud and retaining or re-accreting enough gas to form a second massive star cluster on its centre known as R136 (Massey and Hunter 1998a; Doran et al. 2013). The last has been supported by simulation, e.g., Silich and Tenorio-Tagle (2017) showed that under

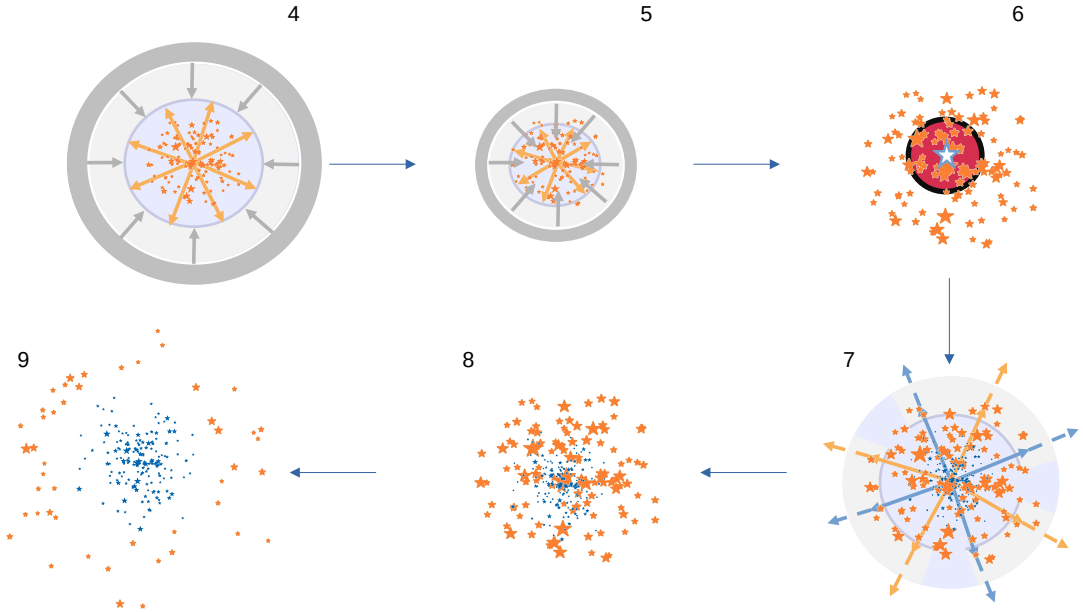

Figure 1.4.1: Life cycle sketch of an embedded star cluster as WARPFIELD describes. Phases 1, 2 and 3 are shown in Fig. 1.1.1.

dense conditions ($n \gtrsim 10^5$ cm^{-3} for a cloud of $M_{\rm cloud} = 10^6$ M$_\odot$), the feedback produced by stellar winds may not be as stronger as it is needed to disperse the cloud.

According to Rahner et al. (2017) results, the massive embedded star clusters can overcome the process of gas expulsion in the range of ϵ_{SF} =0.01-0.15, as the classical picture describes, which fully complete the possible ϵ_{SF} range (red line in Fig. 1.2.1). On the other hand, the classical picture does not take into account the multiple stellar generations scenario and new studies can be developed using this out the box mode to evolve molecular clouds.

2

Hierarchically formed embedded star clusters under instantaneous gas expulsion

In this chapter, we investigate the dissolution process of young embedded star clusters with different primordial mass segregation levels using fractal distributions by means of N-body simulations. We combine several star clusters in virial and subvirial global states with Plummer and uniform density profiles to mimic the gas. The star clusters have masses of $M_{\rm stars}$ = 500 $M_{\odot}$ which follow an initial mass function where the stars have maximum distance from the centre of $r = 1.5$ pc. The clusters are placed in clouds which at the same radius have masses of $M_{\rm cloud}$ = 2000 $M_{\odot}$, resulting in star formation efficiency of 0.2. We remove the background potential instantaneously at a very early phase, mimicking the most destructive scenario of gas expulsion. The evolution of the fraction of bound stellar mass is followed for a total of 16 Myr for simulations with stellar evolution and without. We compare our results with previous works using equal-mass particles where an analytical physical model was used to estimate the bound mass fraction after gas expulsion. We find that independent of the initial condition, the fraction of bound stellar mass can be well predicted just right after the gas expulsion, but tends to be lower at later stages, as these systems evolve due to the stronger two-body interactions resulting from the inclusion of a realistic initial mass function. This discrepancy is independent of the primordial mass segregation level.

2.1 Motivation

Farias et al. (2015) and Farias et al. (2018b) proposed two predictions to estimate the bound mass fraction remaining after violent gas expulsion for models which were representing embedded star clusters using as a first approach, equal-mass particles (mimicking stars), in

order to study one parameter at time. However, in reality, the stars have a wide range of masses, and their preferred locations in the cluster is still an open question (Zinnecker 1982; Murray and Lin 1996; Elmegreen and Krakowski 2001; Klessen 2001; Bonnell et al. 2001; Bonnell and Bate 2006; Girichidis et al. 2012). The main streams for this star formation output are the following:

- The most massive stars form in the densest gas-rich areas where they can continuously accrete material, hence, competing with neighbour stars, a scenario referred as competitive accretion (Larson 1982; Murray and Lin 1996; Bonnell et al. 1997). Evidence supporting this scenario has been detected in embedded star clusters (see e.g.. Lada et al. 1996; Hillenbrand 1997; Hillenbrand and Hartmann 1998; Bonatto and Bica 2006; Chen et al. 2007; Er et al. 2013; Dib and Henning 2019).
- On the other hand, Parker and Goodwin (2015) point out that stars formed by competitive accretion rarely result in a segregated cluster. This is motivated by the large theoretical and observational evidence that star clusters are formed in hierarchical distributions (Könyves et al. 2010; Whitmore et al. 1999; Johnstone et al. 2000; Kirk et al. 2007; Schmeja et al. 2008; Gutermuth et al. 2009; di Francesco et al. 2010; Maury et al. 2011; Wright et al. 2014),
- Mass segregation has also been shown to develop dynamically (McMillan et al. 2007; Allison et al. 2009b; Yu et al. 2011) and on short time scales (Allison et al. 2010; Parker et al. 2016), e.g., within $\sim$ 1 Myr. In some systems, dynamical processes are not fast enough to explain the observed high level of mass segregation, therefore some degree of primordial mass segregation is needed to explain such high concentration of massive stars (Bonnell and Davies 1998; Raboud and Mermilliod 1998). Domínguez et al. (2017) found mass segregation in the early stages of the embedded phase even starting with non-segregated substructured clusters, and also that a very high artificial level of mass segregation is not stable and it is quickly decreased by dynamical processes followed by a lower segregated state (see also e.g., Allison et al. 2009a, 2010).

It is still an open question whether different levels of mass segregation could affect the posterior evolution of clusters after gas expulsion or not. In this chapter, we address this question by testing if the fractions of cluster survival predicted by Farias et al. (2015, 2018b) are still valid with the inclusion of different mass particles and mass segregation. As an extra parameter, we study the same sample also by considering the stellar evolution (SEv), i.e., the individual star masses are decreasing during their life.

2.2 Method

We investigate the dissolution process of young embedded star clusters with different primordial mass segregation levels using fractal distributions by means of N-body simulations. We combine several star clusters in virial and subvirial global states with Plummer and uniform density profiles to mimic the gas. The star clusters have masses of $M_{\rm stars}$ = 500 $M_{\odot}$ which follow an initial mass function (IMF) where the stars have maximum distance from the centre of $r = 1.5$ pc. The clusters are placed in clouds which at the same radius have

masses of $M_{\rm cloud}$ = 2000 M$_\odot$, resulting in star formation efficiency of 0.2. We remove the background potential instantaneously at a very early phase, mimicking the most destructive scenario of gas expulsion. The evolution of the fraction of bound stellar mass is followed for a total of 16 Myr for simulations with stellar evolution and without. We compare our results with previous works using equal-mass particles where an analytical physical model was used to estimate the bound mass fraction after gas expulsion.

2.2.1 Fractal distributions and initial mass function

We follow the setup described in Farias et al. (2015, 2018b) and Domínguez et al. (2017), which is described in this section.

Following the method described in Goodwin and Whitworth (2004), we generate initially substructured distributions with a fractal dimension of $D = 1.6$, with a maximum radius of 1.5 pc and a total stellar mass of 500 M$_\odot$.

We assign individual stellar masses using the modified[1] IMF Kroupa (2002) given by:

$$N(M) \propto \begin{cases} M^{-1.30} & m_0 \leq M/\mathrm{M}_\odot < m_1 \\ M^{-2.30} & m_1 \leq M/\mathrm{M}_\odot < m_2 \\ M^{-2.35} & m_2 \leq M/\mathrm{M}_\odot < m_3 \end{cases} , \tag{2.1}$$

with $m_0 = 0.08$, $m_1 = 0.5$, $m_2 = 1.0$, $m_3 = 50$ M$_\odot$. Using this IMF, we obtain a total number of stars of ~ 1000, and a average stellar mass of 0.5 M$_\odot$.

2.2.2 Quantification of mass segregation using the $\Lambda_{\rm MSR}$ parameter

The focus of this study is to examine if primordial levels of mass segregation influence the later evolution of star clusters. We define all stars with $M \geq 4$ M$_\odot$ as massive stars while the rest are considered low-mass stars. We quantify the different levels of mass segregation using the "mass segregation ratio" parameter ($\Lambda_{\rm MSR}$) introduced by Allison et al. (2009b). $\Lambda_{\rm MSR}$ is calculated by first finding the length of the shortest path joining the $N_{\rm MST}$ most massive stars, i.e., the minimum spanning tree (MST) length, $l_{\rm massive}$. Secondly, the average MST length of $N_{\rm massive}$ random stars $\langle l_{\rm norm} \rangle$ is calculated with its associated standard deviation $\sigma_{\rm norm}$. Finally, $\Lambda_{\rm MSR}$ is defined as:

$$\Lambda_{\rm MSR} = \frac{\langle l_{\rm norm} \rangle}{l_{\rm massive}} \pm \frac{\sigma_{\rm norm}}{l_{\rm massive}}, \tag{2.2}$$

where a value of $\Lambda_{\rm MSR} \sim 1$ indicates no mass segregation, i.e., low and high mass stars are uniformly distributed. $\Lambda_{\rm MSR} \gg 1$ indicates strong mass segregation, i.e., massive stars are located close to each other. $\Lambda_{\rm MSR} < 1$ means inverse mass segregation, i.e., high mass stars are more dispersed than low mass stars. In this work, we explore different levels of mass segregation. These are achieved by locating the massive stars:

[1] We avoid the substellar mass range below 0.08 M$_\odot$ for brown dwarfs

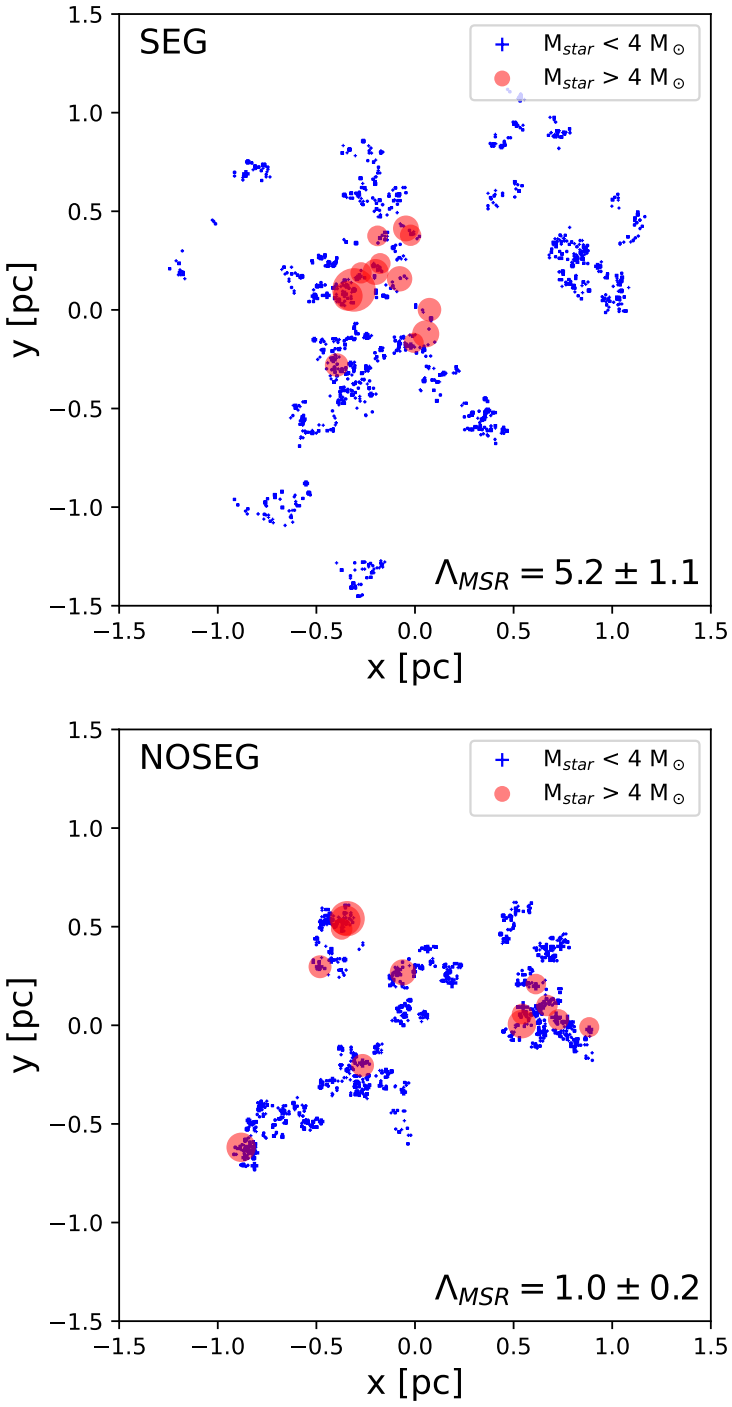

Figure 2.2.1: Two different fractal distributions. The top panel shows a cluster with mass segregation (SEG) and bottom panel a cluster non-segregated (NOSEG). Low mass stars ($M < 4$ M$_\odot$) are represented with blue plus symbols (+) and massive stars ($M \geq 4$ M$_\odot$) with red circles. The sizes of the points are associated to the mass of the stars. The size of the massive stars is multiplied by 5 times for a better appreciation of their location.

i) randomly in a radius $r > 0.5$ pc until finding $\Lambda_{\rm MSR} \sim 1$, i.e., a cluster without mass segregation which hereafter is refereed as NOSEG.

ii) We force all massive stars to be located in a radius $r < 0.5$ pc until obtaining $4 < \Lambda_{\rm MSR} < 5$, i.e., primordial mass segregated clusters, hereafter refereed as SEG.

An example of two fractal distributions with different levels of mass segregation is shown in Fig. 2.2.1. The top panel shows a strongly mass segregated (SEG) fractal star cluster, for this case we have $\Lambda_{\rm MSR} = 5.2 \pm 1.1$. The bottom panel shows a non-segregated (NOSEG) fractal star cluster with $\Lambda_{\rm MSR} = 1.0 \pm 0.2$ where massive stars are spread along the distribution. In both panels, blue plus symbols (+) represent low mass stars ($M < 4$ M$_\odot$) and red circles represent massive stars ($M > 4$ M$_\odot$). The sizes of the symbols are proportional to the mass of the stars, but for massive stars the sizes have been multiplied by 15 for better appreciation.

2.2.3 Background potential

We use two different descriptions for the distribution of the background gas (BG). One, assuming the gas is centrally concentrated, represented by a Plummer (1911) sphere, with a density radial profile, $\rho(r)$, described by

$$\rho(r) = \frac{3M_{\rm Pl}}{4\pi R_{\rm Pl}^3}\left(1+\frac{r^2}{R_{\rm Pl}^2}\right)^{-\frac{5}{2}} \tag{2.3}$$

with $M_{\rm Pl}$ and $R_{\rm Pl}$ the Plummer Mass and Plummer radius respectively, and r being the distance to the centre of the cloud. The enclosed mass $M(r)$ within Plummer sphere is

$$M(r) = M_{\rm Pl}\frac{r^3}{R_{\rm Pl}^3}\left(1+\frac{r^2}{R_{\rm Pl}^2}\right)^{-\frac{3}{2}}, \tag{2.4}$$

which produces a BG potential $\phi(r)$ as follows:

$$\phi(r) = -\frac{GM_{\rm Pl}}{R_{\rm Pl}}\left(1+\frac{r^2}{R_{\rm Pl}^2}\right)^{-\frac{1}{2}}, \tag{2.5}$$

where G is the gravitational constant.

The second set of models assumes the background gas is uniformly distributed within the cloud. In this case, the density profile is constant with a value:

$$\rho(r) = \frac{3M_{\rm tot}}{4\pi r_c^3},\ r < r_c \tag{2.6}$$

with $M_{\rm tot}$ the total mass of the sphere and r_c the radius of the sphere truncated to be 1.8 pc.

Initial mass distribution	Initial virial ratio	Fractals	IMF	BG potential	Virial time	Number of simulations	Stellar evolution
SEG	0.5	10	10	Plummer/Uniform	1/2/3/4	100/100/100/100	No
SEG	0.2	10	10	Plummer/Uniform	1/2/3/4	100/100/100/100	No
SEG	0.5	10	10	Plummer/Uniform	1/2/3/4	100/100/100/100	Yes
SEG	0.2	10	10	Plummer/Uniform	1/2/3/4	100/100/100/100	Yes
NOSEG	0.5	10	10	Plummer/Uniform	1/2/3/4	100/100/100/100	No
NOSEG	0.2	10	10	Plummer/Uniform	1/2/3/4	100/100/100/100	No
NOSEG	0.5	10	10	Plummer/Uniform	1/2/3/4	100/100/100/100	Yes
NOSEG	0.2	10	10	Plummer/Uniform	1/2/3/4	100/100/100/100	Yes
EQUAL	0.5	100	0	Plummer/Uniform	1/2/3/4	100/100/100/100	No
EQUAL	0.2	100	0	Plummer/Uniform	1/2/3/4	100/100/100/100	No

Table 2.2.1: Summary of initial conditions used for our study. The first column shows the initial stellar distribution, the second column shows the value of the initial virial ratio, the third and fourth columns indicate the number of different fractal distributions and IMF samples, respectively. Background gas (BG) profile is provided in the fifth column. The sixth column indicates the different virial times when the gas is expelled, and the seventh column shows the number of realizations for each set. The eighth column shows cases where stellar evolution is included.

The enclosed $M(r)$ within a uniform sphere is described by:

$$M(r) = \frac{M_{\rm tot}}{r_c^3} r^3, \; r < r_c \tag{2.7}$$

and its respective BG potential $\phi(r)$ inside and outside of the sphere as follows:

$$\phi(r) = \frac{GM_{\rm tot}}{2r_c^3} \left(r^2 - 3r_c^2\right), \; r < r_c, \tag{2.8}$$

$$\phi(r) = \frac{GM_{\rm tot}}{r}, \; r > r_c. \tag{2.9}$$

The total mass for the background sphere of gas is chosen ensuring a global SFE $= 0.2$ within a radius if 1.5 pc where the total mass in stars is ~ 500 M$_\odot$. For the case of the Plummer sphere this is achieved by setting $M_{\rm Pl} = 3472$ M$_\odot$ and $R_{\rm Pl} = 1.0$ pc. For the uniform sphere case, $M_{\rm tot} = 3455$ M$_\odot$. We use these values in order to have a direct comparison with Farias et al. (2015, 2018b) and Domínguez et al. (2017), which are justified following a similar setup as in the classical picture of Baumgardt and Kroupa (2007) and observations (see e.g. Megeath et al. 2016).

2.2.4 Initial virial state

The virial ratio is defined as:

$$Q = \frac{T}{|\Omega|}, \tag{2.10}$$

where T and Ω are the total kinetic and potential energy of the system respectively[2].

In this work, we investigate two different initial dynamical states of star clusters, a sub-

[2]In latest literature Q value is also found referred to α but we keep the symbol to be consistent with Farias et al. (2015, 2018b) and Domínguez et al. (2017) which are referred in this chapter.

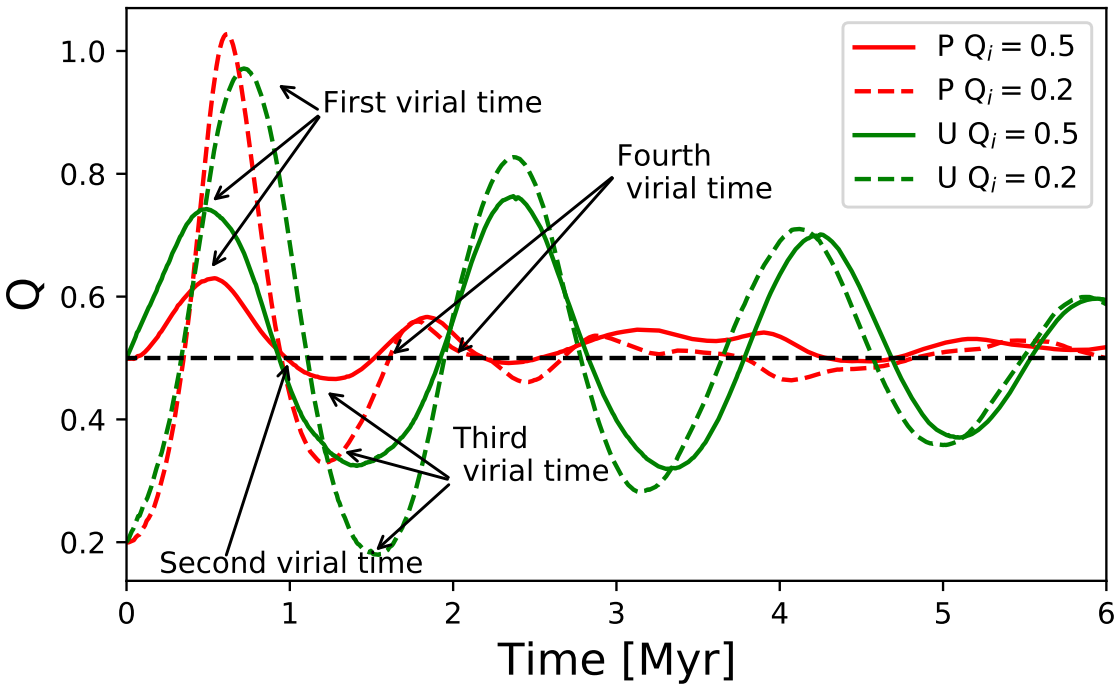

Figure 2.2.2: Example of Q evolution in time with different initial virial states under different background gas distributions. Red line shows the evolution of Q for a model under a Plummer (P) background gas profile and green line for a model with an uniform (U) distribution. Solid and dashed lines shows models with virial ($Q_i = 0.5$) and sub-virial ($Q_i = 0.2$) initial velocities. First, second, third and fourth virial times are pointed with arrows and they are the moments when the background gas is removed. Dashed black line shows the virial equilibrium value of $Q = 0.5$.

virial state represented by $Q = 0.2$ and virial equilibrium state with $Q = 0.5$. We note, however, that the latter does not represent a system in equilibrium, rather a system with velocities that match virial equilibrium. The fractal distributions used here are far from an equilibrium system, therefore, these systems will pursuit an equilibrium distribution. The rearrangement of stars and energy causes the measured virial ratio to oscillate around an equilibrium value as the clusters evolve. An example of the evolution of Q with time under different conditions can be seen in Figure 2.2.2 where the red line shows the evolution of one fractal cluster in a Plummer BG and the green line for the same fractal cluster but now under the influence of a uniform background gas distribution. Solid and dashed lines represent the initial states $Q_i = 0.5$ and $Q_i = 0.2$, respectively. The horizontal dashed black line represents the virial state $Q = 0.5$. As expected sub-virial star clusters show a larger amplitude of the oscillation of Q with time relative to the $Q_i = 0.5$ case. Stars in a cluster with $Q_i = 0.2$ tend to have orbits that fall through the center of potential of the system, reaching high velocities as they cross the potential minimum. While stars in systems with $Q_i = 0.5$ tend to have more circular and stable orbits.

2.2.5 Virial evolution and gas expulsion

In Figure 2.2.2 we point out different locations of the evolution of Q. At the selected points, we emulate rapid gas expulsion by removing the influence of the background gas. Different locations on the oscillation of the virial ratio are referred as virial time (VT). We call the first peak in the evolution of Q "First virial time". At this point, star clusters are supervirial and we can obtain star clusters with pre-gas expulsion virial ratio of $Q_{\rm f} > 0.5$. The exact values of $Q_{\rm f}$ vary between the different models. After this first maximum, the cluster passes through a state with $Q = 0.5$, we term this point "Second virial time". All star clusters at this point have the same value of $Q_{\rm f}$. Then, star clusters reach a first minimum of Q, the "Third virial time". Here, star clusters have sub-virial velocities and therefore we can obtain star clusters with $Q_{\rm f} < 0.5$ within a range of values. Finally, star clusters reach $Q = 0.5$ again, after the first minimum, we call this point "Fourth virial time". By simplicity, we refer to them as VT $= 1, 2, 3, 4$, respectively. Note that these four points in the evolution of star clusters are different for each individual cluster. Therefore, for each set of initial conditions, we run 4 simulations removing the BG potential at these four different times.

2.2.6 Bound mass

We refer as the bound mass $f_{\rm bound}$ to the fraction of stellar mass that is gravitationally bound ($M_{\rm bound}$) relative to the initial stellar mass $M_{\rm init}$:

$$f_{\rm bound} = \frac{M_{\rm bound}}{M_{\rm init}}. \tag{2.11}$$

We measure this value at different times in the evolution of the simulation. We compare the results with the two predictive models introduced by Farias et al. (2015) and Farias et al.

Parameter	This study	Baumgardt and Kroupa (2007)
Background potential	Plummer and uniform	Plummer
Virial ratio	0.5 and 0.2	0.5
Stars distribution	Fractal	Plummer
Mass segregation	Yes and no	No
Stars' effective radius	0.8-1.2	1.0
Gas expulsion	Instantaneous	Instantaneous
Initial star formation efficiency	0.20	0.33
Star formation events	1	1

Table 2.2.2: Parameter comparison used in this study and by Baumgardt and Kroupa (2007) (classical picture).

(2018b). The first model is given by

$$f_{\rm bound} = {\rm erf}\left(\sqrt{\frac{3}{2}\frac{\rm LSF}{Q_{\rm f}}}\right) - \sqrt{\frac{6}{\pi}\frac{\rm LSF}{Q_{\rm f}}}\exp\left(-\frac{3}{2}\frac{\rm LSF}{Q_{\rm f}}\right), \tag{2.12}$$

where LSF is the local stellar fraction introduced by Smith et al. (2011) defined as the SFE measured within the stellar half-mass radius centered on one of the clumps and $Q_{\rm f}$ is the pre-gas expulsion virial ratio, including the contribution of the BG to the potential felt by the stars. These two quantities are time dependent which contain more information about the stellar distribution at the time when they are measured.

The second model neglects the contribution of the gas to the system. It estimates the amount of bound stellar mass using the virial ratio at the moment of gas expulsion ($Q_{\rm a}$), assuming that all gas is expelled instantaneously. The bound stellar fraction is estimated as:

$$f_{\rm bound} = {\rm erf}\left(\sqrt{\frac{3}{2}\frac{1}{Q_{\rm a}}}\right) - \sqrt{\frac{6}{\pi}\frac{1}{Q_{\rm a}}}\exp\left(-\frac{3}{2}\frac{1}{Q_{\rm a}}\right). \tag{2.13}$$

In practice, this model simplifies the estimation of $f_{\rm bound}$ as it only requires information from the stellar component.

These models were successfully tested in a scenario were all stars have the same mass. We also refer to these models as first and second prediction. In this work, we test the reach of these models in a scenario where stars follow a realistic IMF and mass loss by stellar evolution is included.

2.3 Comparison of the initial conditions with the classical picture

As in previous studies (see Sec. 1.3), we do not vary our initial conditions very far from the classical picture. In Tab. 2.2.2 we summarize the differences between this study and Baumgardt and Kroupa (2007). The main reason to stay close to the classical picture is to be able to make comparisons and to understand why the inclusion of new initial conditions is or is not changing the previous results.

2.4 Set of simulations

For the SEG sample, we create 10 fractal distributions and 10 different IMF samples associated with them. For each pair of positions and masses, we generate 10 different random assignments of the masses to the positions getting mass segregated clusters, which leads to a total number of 100 simulations. We double the number of simulations scaling the velocities of the particles in order to obtain embedded star clusters starting with $Q_i = 0.5$ and with $Q_i = 0.2$. For each Q_i the sample is multiplied by four as we have four different VT where we remove the BG finalizing with 800 simulations. We add another sample of 800 simulations as we proceed in the same way to produce the NOSEG sample. We evolve the simulations for 16 Myr using the direct N-body code NBODY6++GPU (Wang et al. 2015) which includes stellar mass loss from stellar evolution. We double the 1600 SEG and NOSEG simulations running again the same sample, but this time with SEv activated. As we employ the latest version of the code used by Farias et al. (2015, 2018b), we also introduce a third sample with other 800 simulations, but this time based on equal-mass particles as a control method reproducing the results from our previous works. For the equal-mass particle sample, in order to have the same sample size, we use 100 different fractals and we proceed as before ending up with the same number of simulations. We do not use SEv for equal-mass particles simulations. Altogether, we perform a total number of 4000 simulations. The full sample is summarized in Table 2.2.1.

2.5 Results

As in previous works, we are mostly interested in the fraction of stars that remain bound at a late stage, when any sign of initial structure is already lost, specifically we measure $f_{\rm bound}$ at 16 Myr which corresponds to ~ 14.6 initial crossing times. We reproduce the same plots as already shown in Farias et al. (2015) and Farias et al. (2018b) for a direct comparison. However, we notice that $f_{\rm bound}$ is not constant after gas expulsion, and therefore we also measure it at early stages in the evolution, i.e., we determine $f_{\rm bound}$ at the precise moment of gas expulsion (TEXP) and at times $t = 4.8$, 6.4, 8, 9.6, 11.2, 12.8 and 13.4 Myr. In this way we can see how fast dynamical evaporation is affecting the surviving systems. Note that the exact value of TEXP is different for every cluster, since it is calculated based on their specific virial ratio evolution (see § 2.2.4). We use the same times, and $t = 0$ Myr, to observe what value of $\Lambda_{\rm MSR}$ is achieved relative to the imposed initial conditions.

2.5.1 Equal-mass simulations

The results of our first 800 simulations sample are used as the control sample and for comparison with the new parameter space introduced in this work.

We reproduce the same plot as shown in Farias et al. (2015) which contains only VT = 1 and VT = 3. In Fig. 2.5.1, we show the resulting bound fractions for this set, measured at 16 Myr for star clusters with different $Q_{\rm f}$ and background gas distributions. Black solid line shows Eq. 2.12 using the central value of $Q_{\rm f}$ described in each panel and the LSF value from

x-axis. Blue triangles are simulations under a Plummer BG potential (P) and red triangles are simulations under a Uniform BG potential (U). Filled and empty symbols are representing the initial virial ratios $Q_{\rm i} = 0.5$ and $Q_{\rm i} = 0.2$, respectively. The triangles have the average values for $f_{\rm bound}$ at 16 Myr for the simulations with values of LSF and $Q_{\rm f}$ in the respective range. Note that for the cases where $Q_{\rm f}$ is sub and super-virial, the exact value of Q is not possible to fix, since each cluster reaches a different peak in Q depending of the initial distribution of stars. Therefore, we can not fill each panel with the same quantity of points, with the most extreme values of $Q_{\rm f}$ being the rarest.

We observe that the first prediction (Eq. 2.12) is more accurate in top panels (star clusters with $Q_{\rm f} < 0.5$) whereas there is no clear trend in the bottom panels. The reason of this is due to the high levels of substructure still present in the bottom panels. Gas expulsion at VT = 1 is very early and therefore substructure had not had time enough to be erased. The LSF value is sensible to this effect as it needs to find the half-mass star radius centered in one of these sub-clusters. We also include the results with VT = 2 and VT = 4 in Fig. 2.5.2 (left panel). In this case, early and late gas expulsion are mixed and a large dispersion is measured, but the prediction still matches the results in 1 σ error range. To see the effect of early and later gas expulsion more clearly, we show in Fig. 2.5.3, top panels, the average difference between the $f_{\rm bound}$ measured ($f_{\rm measured}$) and the predicted value from Eq. 2.12 ($f_{\rm predicted}$) divided by VT from left to right. The gray area represents the 1 σ error including all the cases, showing less dispersion for VT = 3 and VT = 4. In Fig. 2.5.6 (left panel) the blue squares represent the values from the gray zone in Fig. 2.5.3 shown independently for a better appreciation. Farias et al. (2015) mostly explored gas expulsion times with VT $>$ 3 when the initial substructure is mostly erased by dynamical processes (Allison et al. 2009a; Parker et al. 2014). The prediction gets much closer to the results at VT $\geq$ 3 and it is expected to get even closer when gas expulsion happens later. Nevertheless, the moment of gas expulsion is kept as shown to make the study more realistic as it has been constrained that gas expulsion occurs very early for low mass clusters (Dinnbier and Walch 2020).

In Fig. 2.5.4 (left panel) we show the same models, again measured at 16 Myr, but as a function of the virial ratio right after gas expulsion, $Q_{\rm a}$. Black solid line shows the prediction from Eq. 2.13, i.e., using $Q_{\rm a}$ as single parameter estimator. In this plot, all VT are included. Most of the clusters after gas expulsion become highly super-virial ($Q_{\rm a} \gg 1$) because of the instant removal of the BG potential. Triangles represent the same initial conditions described before and the values are grouped in bins of $\Delta Q_{\rm a} = 0.5$. The model corresponding to Eq. 2.13 describes the results within the whole $Q_{\rm a}$ range and it is not sensitive to the VT when the gas expulsion is measured. The latter can be seen in Fig. 2.5.6 (top panels), where a similar scatter is present when gas-expulsion happens at different VT with only a few exceptions falling outside the gray zone. The dispersion of the results is less for these results as 1 σ error is smaller than before. Figure 2.5.6 (left panel) shows the width of the gray area for this prediction, with the green circles being smaller for three of the four VT. Therefore, the description provided by Eq. 2.13 is more suitable for our work since most of our simulations in this work expel the gas at very early times when high levels of substructure are still present.

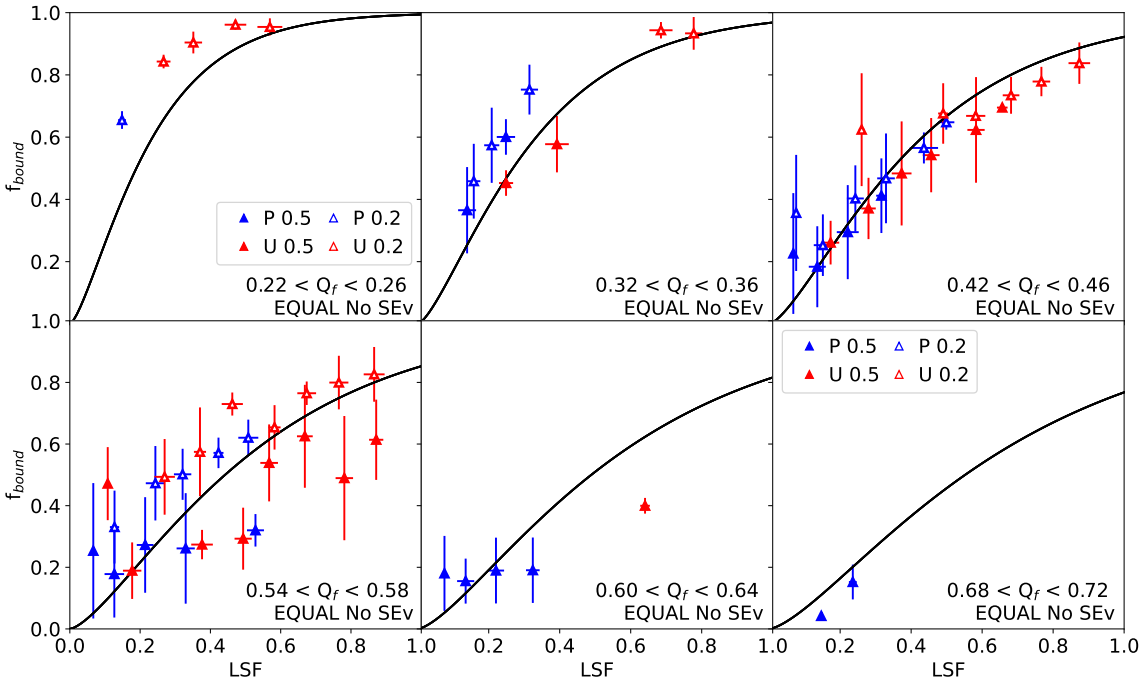

Figure 2.5.1: $f_{\rm bound}$ vs LSF for equal-mass particles simulations without stellar evolution at 16 Myr for VT = 1 (bottom row) and VT = 3 (top row). Blue and red triangles are simulations with Plummer (P) and Uniform (U) BG potential, respectively. The initial virial ratios $Q_{\rm i} = 0.5$ and $Q_{\rm i} = 0.2$ are represented by filled and empty symbols, respectively. The solid black line shows the predictive model introduced by Farias et al. (2015), i.e., Eq. 2.12, using the central value of $Q_{\rm f}$ in each respective panel

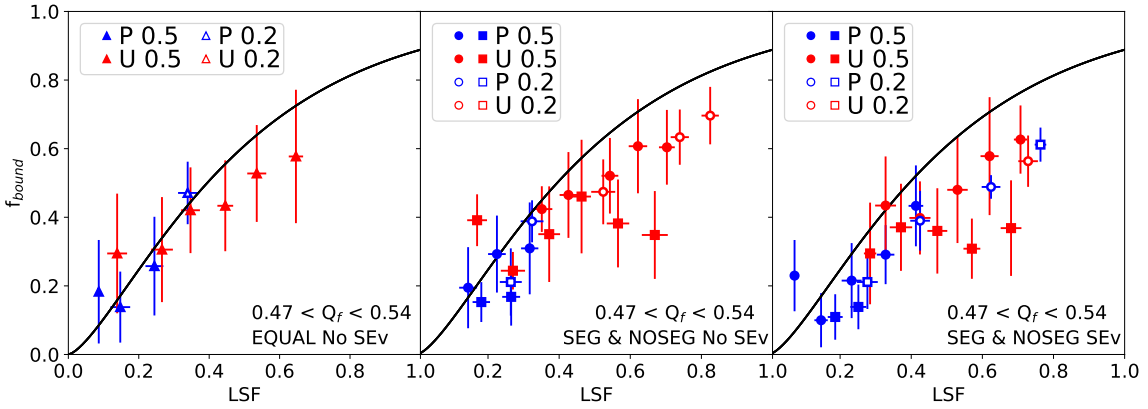

Figure 2.5.2: $f_{\rm bound}$ vs LSF only for $Q_{\rm f} = 0.5$ (only reached when VT = 2 and VT = 4). The left panel is for equal mass simulations and it uses the same colours and symbols as in Fig. 2.5.1 where the black line is Eq. 2.12. The central panel shows results for simulations using IMF and non stellar evolution. SEG simulations are shown with circles and NOSEG simulations are shown with squares. The right panel is similar as the central one, but now for simulations using stellar evolution.

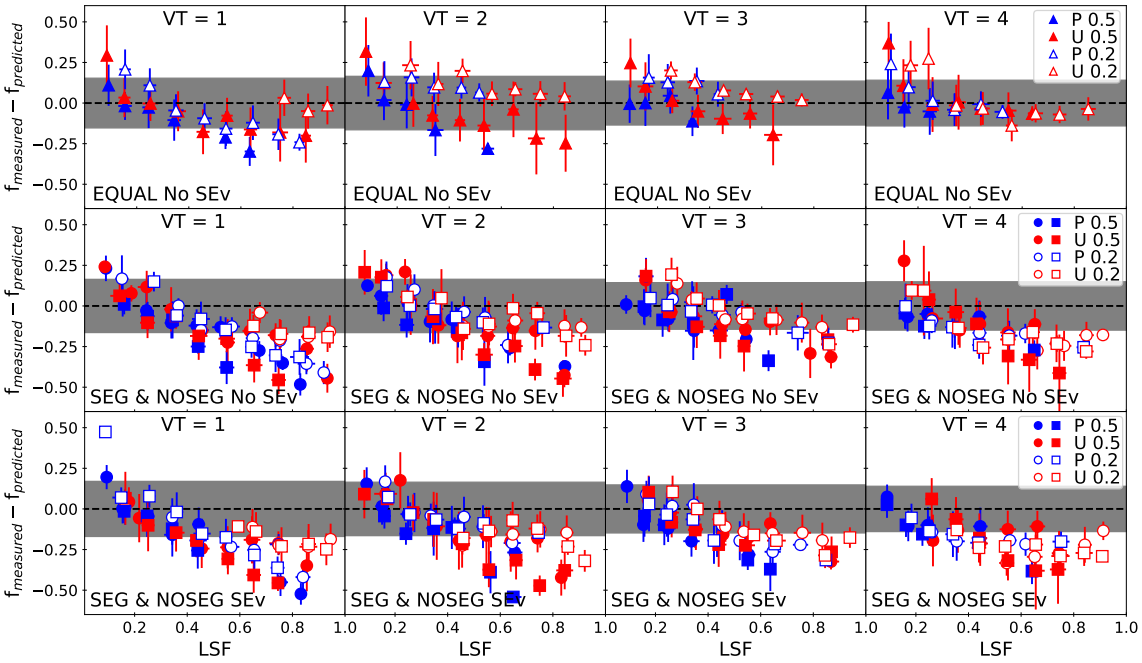

Figure 2.5.3: Average difference between the measured bound fraction ($f_{\rm measured}$) and the predicted bound fraction ($f_{\rm predicted}$) from Eq. 2.12 vs LSF. The black dashed line represents a zero difference with the prediction. The panels are ordered from left to right by virial time (VT) and from top to bottom as in Fig. 2.5.2 (now vertically) with the respective colour and symbols. The gray area represents the average 1 σ error for all the result in each panel.

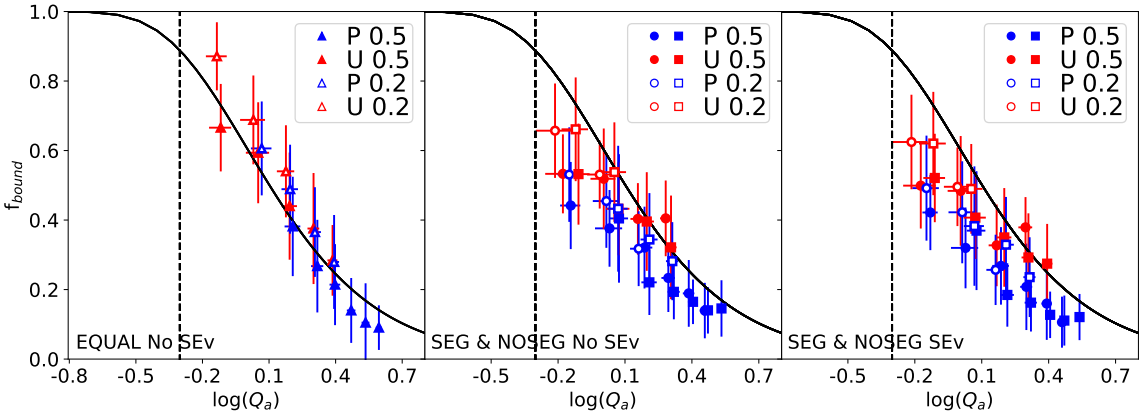

Figure 2.5.4: $f_{\rm bound}$ vs log($Q_{\rm a}$). The order, colour and symbols are the same as Fig. 2.5.2. The solid black line shows the Eq. 2.13. Dashed black line is the equilibrium value of $Q = 0.5$ as a reference.

2.5.2 SEG-NOSEG simulations with no SEv

The results for SEG and NOSEG simulations with No-SEv at 16 Myr for VT = 1 and VT = 3 are shown in Fig. 2.5.7. The symbols are the same as before. For these cases, circles indicate simulations starting with SEG and squares for simulations starting with NOSEG.

We observe that in most cases Eq. 2.12 over-estimates $f_{\rm bound}$, especially at higher values of LSF. We also include the results when $Q_{\rm f} = 0.5$ (VT = 2 and VT = 4) in Fig. 2.5.2 (central panel), where we observe the same behaviour.

We test Eq. 2.13 in Fig. 2.5.4 with the same symbols as before, where all VT are included. Again, at 16 Myr, most of the simulations have lower values of $f_{\rm bound}$ than expected. SEG and NOSEG simulations show the same behaviour, with both analytical models over estimating the bound fraction. When using Eq. 2.12 many dots are outside the one-sigma error bars, while Eq. 2.13 does a better job with estimations mostly within error bars.

The question of how early and late gas expulsion influence the accuracy of the prediction is addressed in Fig. 2.5.3 and Fig. 2.5.5 (second row) for the first prediction and second prediction, respectively. For Eq. 2.12, we observe that independent of the VT, the results are mostly out of the gray zone especially for higher LSF. For Eq. 2.13, more results are falling inside 1 σ error zone with exceptions for low Q_a. This behaviour is better appreciable in Fig. 2.5.6, where the dispersion for the results of the first prediction (blue squares) compared to the second prediction (green circles) is larger for VT ≤ 2 and in the same range for VT ≥ 3. Besides the *individual results*, in most of the cases, $f_{\rm bound}$ is found below the predictions.

2.5.3 SEG-NOSEG simulations with SEv

The results for SEG and NOSEG simulations with SEv at 16 Myr for VT = 1 and VT = 3 are shown in Fig. 2.5.8. The symbols are the same as before. The values of LSFs are not expected to be identical for all pairs of simulations started with SEv and No-SEv due to small changes in the orbit calculations done in a N-body simulation. We observe as before that the prediction Eq. 2.12 over estimates $f_{\rm bound}$. The number of simulations far from the curve is higher for this sample and the same is observed for $Q_{\rm f} = 0.5$ (VT = 2,4) in Fig. 2.5.2 (right panel).

The prediction from Eq. 2.13 is shown in Fig. 2.5.4 with the same symbols as before. The values of $f_{\rm bound}$ at the end of most simulations are even smaller than when we do not use SEv.

As in the previous cases, we test early and late gas expulsion in Fig. 2.5.3 and Fig. 2.5.5 (bottom panels). The same description previously mentioned for the simulations without SEv is applicable for these results but now with a larger number of simulations outside of the gray area. In Fig. 2.5.6 we observe a small improvement in the dispersion of the results when VT = 4, if we compare with its pair in the central panel.

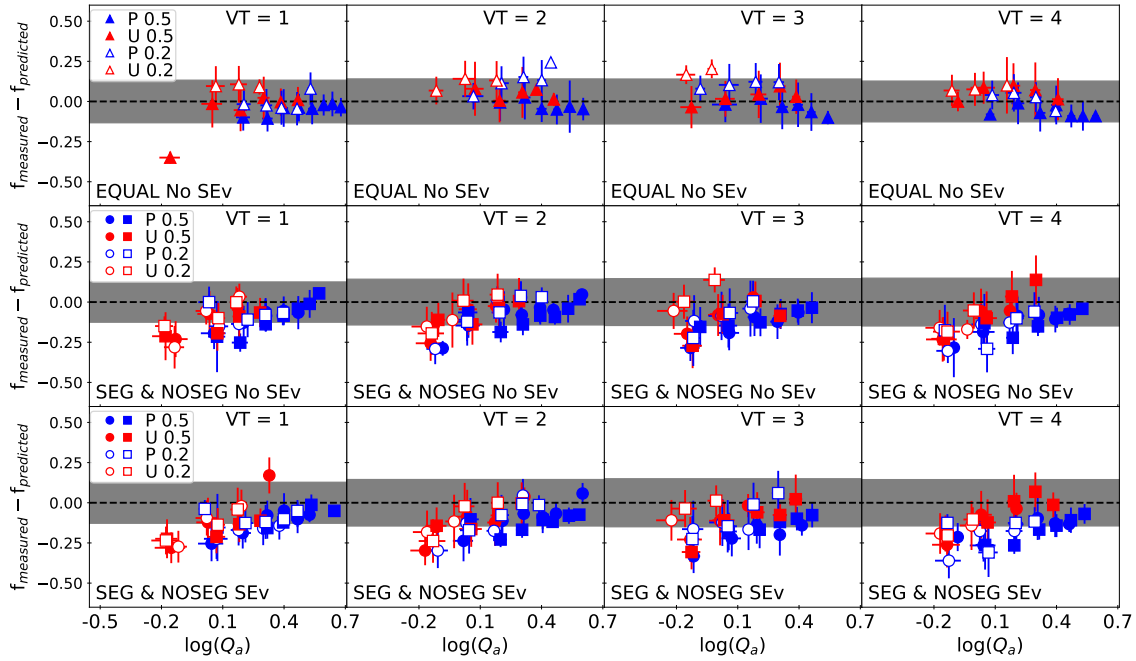

Figure 2.5.5: Average difference between the measured bound fraction ($f_{\rm measured}$) and the predicted bound fraction ($f_{\rm predicted}$) from Eq. 2.13 vs $Q_{\rm a}$. The order, colour and symbols are the same as in Fig. 2.5.3.

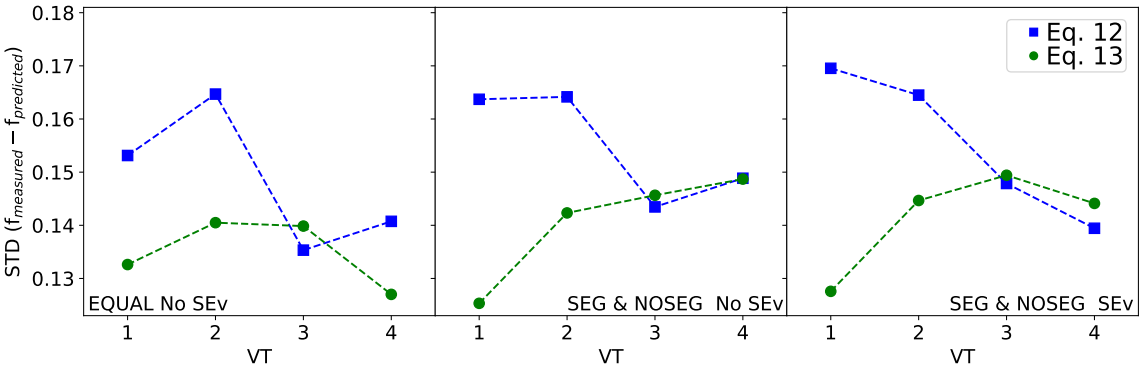

Figure 2.5.6: 1 σ error value (STD) of the difference between the predicted bound fraction ($f_{\rm predicted}$) vs virial time. The squares with blue lines are for Eq. 2.12 and circles with green line are for Eq. 2.13. The panel order is the same as in 2.5.2.

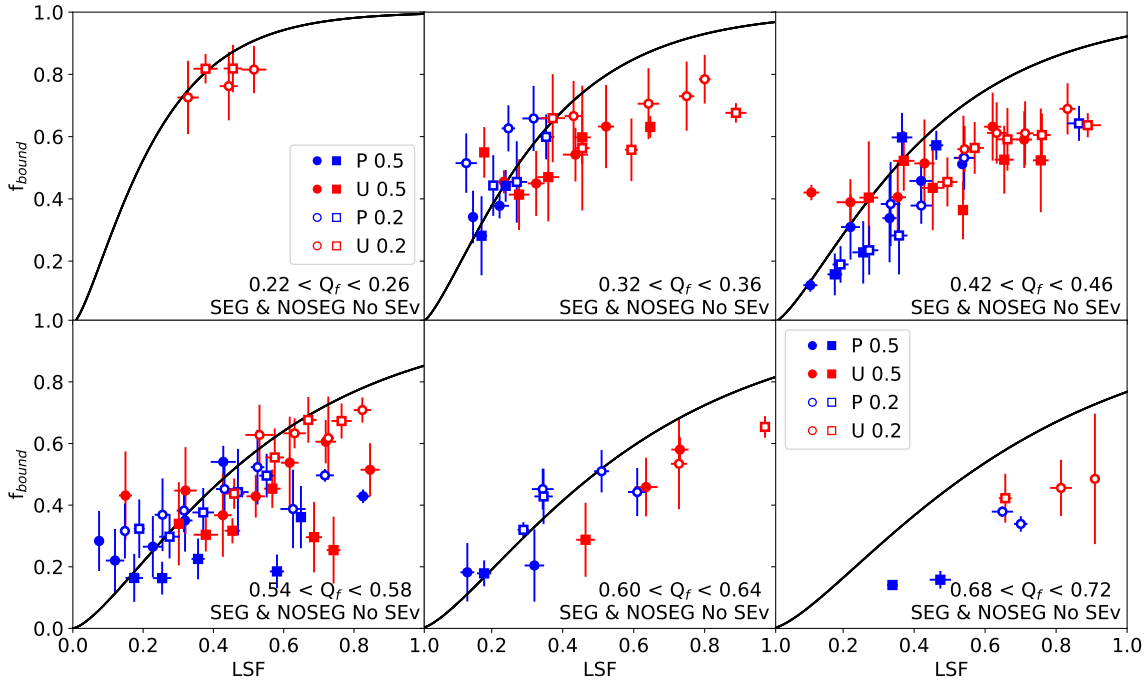

Figure 2.5.7: $f_{\rm bound}$ vs LSF for simulations with non stellar evolution at 16 Myr for VT = 1 (bottom row) and VT =3(top row). Colour and symbols are the same as in Fig. 2.5.2 where the black line is Eq. 2.12.

2.5.4 Mass segregation

We show in Fig. 2.5.9 the time evolution of $\Lambda_{\rm MSR}$. The symbols are the same as before and the solid black line is $\Lambda_{\rm MSR} = 1$ which means a stellar distribution where massive stars are distributed the same way as low mass stars, i.e., without mass segregation.

The left top panel is the evolution of mass segregation for simulations starting with SEG initial stellar distribution, and No-SEv. At the beginning, $\Lambda_{\rm MSR} = 4.05 \pm 0.77$ for all cases as they are the same fractals with the same IMF samples. At the moment of gas expulsion, which happens typically at a time of 1.18 ± 0.50 Myr, the level of mass segregation decreases until it reaches $\Lambda_{\rm MSR} = 3.02 \pm 1.49$. On the other hand, the simulations in the right panel at $t = 0$ Myr have $\Lambda_{\rm MSR} = 1.00 \pm 0.02$. At the moment of gas expulsion at $t = 1.25 \pm 0.55$ Myr the level of mass segregation increases to an average value of $\Lambda_{\rm MSR} = 1.32 \pm 0.35$. The same behaviour is observed in the bottom panels, where stellar evolution is activated. Initial values are the same as they are from the same clusters. Small differences can appear due to the randomness of choosing the sample of low mass stars for the calculation of $\Lambda_{\rm MSR}$ (see § 2.2.2). The evolution of the virial ratio is very similar since only SEv mass loss from winds acts on timescales $\lesssim 1$ Myr for most of the stars. In the left panel at $t = 1.19 \pm 0.50$ the mass segregation on average is $\Lambda_{\rm MSR} = 3.01 \pm 1.48$ and in right panel at $t = 1.25 \pm 0.55$ it is $\Lambda_{\rm MSR} = 1.32 \pm 0.37$. The values for each of the cases are summarized in Tab. 2.5.1. The gas expulsion for simulations with uniform BG potential is slightly later than simulations with

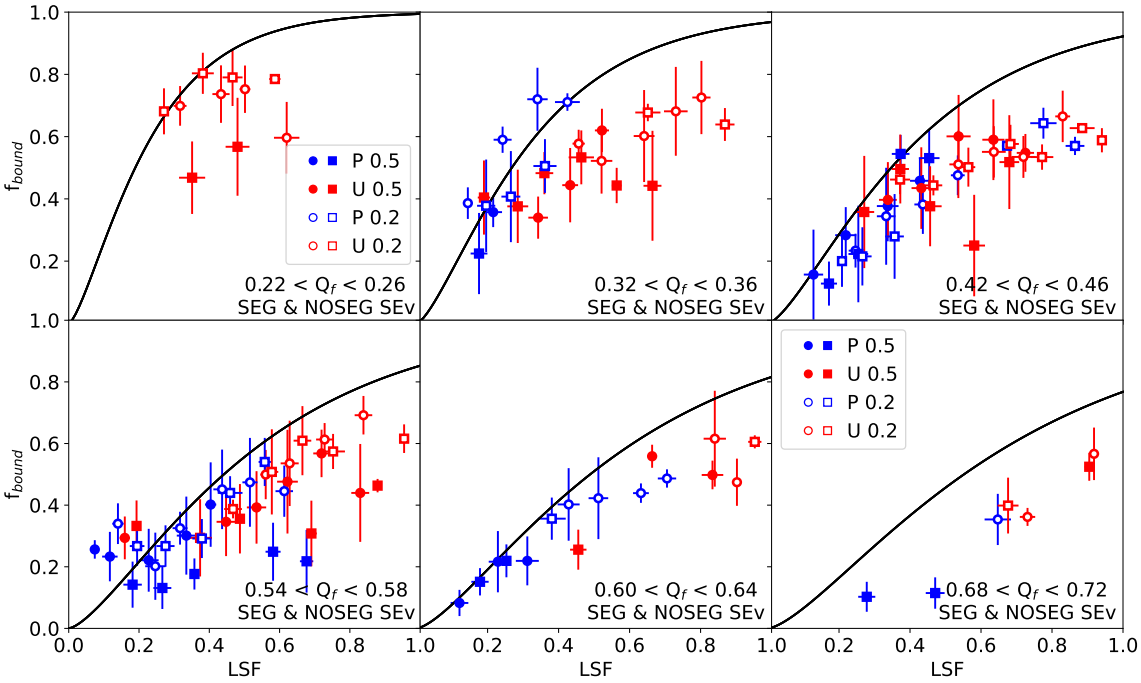

Figure 2.5.8: $f_{\rm bound}$ vs LSF for simulations with stellar evolution at 16 Myr for VT = 1 (bottom row) and VT = 3 (top row). Colour and symbols are the same as in Fig. 2.5.2.

Plummer BG potential.

As reported in Domínguez et al. (2017) and Pavlík et al. (2019), we see that clusters with initial mass segregation rapidly decrease their levels during the embedded phase, as they relax into a more stable configuration. On the other hand, clusters with NOSEG initial stellar distribution start raising their mass segregation levels until gas-expulsion happens.

We include a linear fit for times ≥ 4.8 Myr to each pair of initial conditions with the form:

$$\Lambda_{\rm MSR}(t) = m_\Lambda t + \Lambda_{{\rm MSR},t=4.8}, \qquad t \geq 4.8, \tag{2.14}$$

where m_Λ is the slope of the fit in units of Myr^{-1} and $\Lambda_{{\rm MSR},t=4.8}$ is the $\Lambda_{\rm MSR}$ at 4.8 Myr, which is shown in Tab. 2.5.1, last column. As the clusters expand after gas expulsion, the value of $\Lambda_{\rm MSR}$ shows a continuous decrease ($m_\Lambda < 0$), being steeper for SEG simulations. Simulations with SEv are shown in the bottom panels. In this case, the decrease of $\Lambda_{\rm MSR}$ is steeper as the more massive stars explode as SNe.

2.5.5 Dynamical evaporation

As we have introduced different masses, stronger interactions between the stars are expected, leading to the ejection of stars. In addition, SEv adds another source of mass loss. In

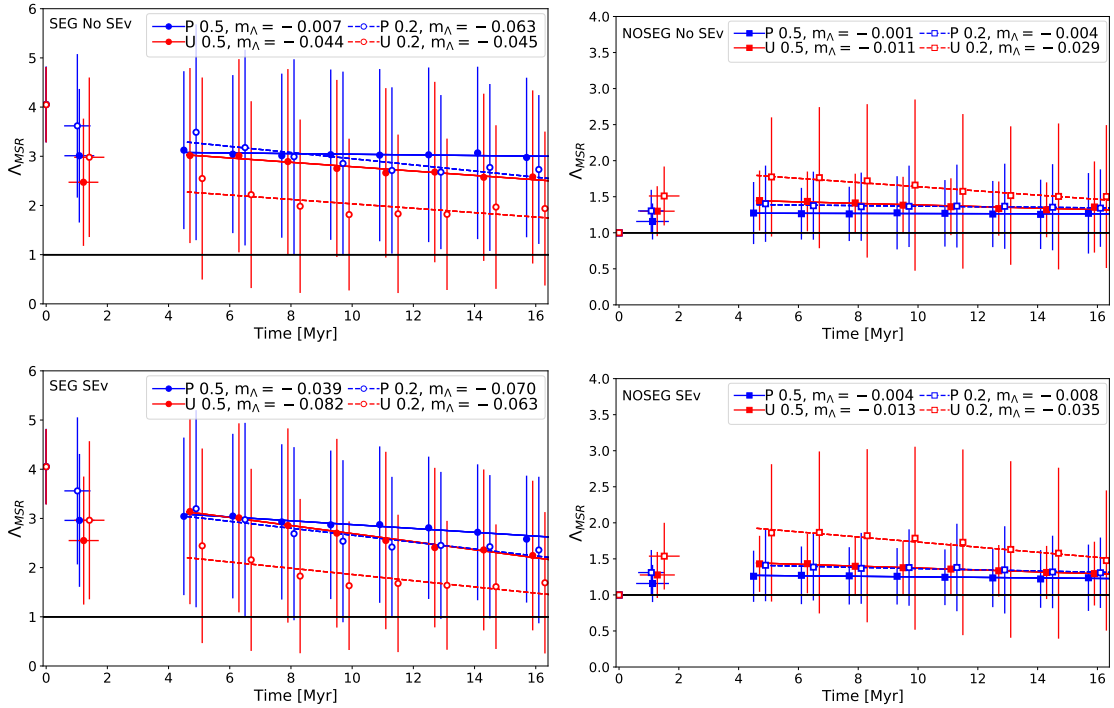

Figure 2.5.9: $\Lambda_{\rm MSR}$ vs time. Colours and symbols are the same as in the previous figures. The solid black line is $\Lambda_{\rm MSR} = 1$ which means a star cluster not segregated. Simulations in top panels are with No-SEv and bottom panels with SEv. The lines show linear fit according to Eq. 2.14 where the slopes m_Λ are indicated respectively in the legends.

Table 2.5.1: Summary of $\Lambda_{\rm MSR}$. First and second columns indicate the BG potential (P = Plummer, U = uniform) with its respective initial virial ratio. The third column refers to the sample initial stellar distribution and if the stellar evolution is on. The fourth column shows the initial $\Lambda_{\rm MSR}$ value and fifth column is the average time when gas expulsion is done. Sixth column is the $\Lambda_{\rm MSR}$ at the moment of gas expulsion and last column shows the $\Lambda_{\rm MSR}$ at 4.8 Myr.

BG	$Q_{\rm i}$	Sample/SEv	Initial $\Lambda_{\rm MSR}$	Time TEXP	$\Lambda_{\rm MSR,ge}$	$\Lambda_{{\rm MSR},t=4.8}$
P	0.5	SEG/No	4.05 ± 0.77	1.08 ± 0.49	3.01 ± 1.36	3.12 ± 1.61
P	0.2	SEG/No	4.05 ± 0.76	1.02 ± 0.43	3.62 ± 1.46	3.49 ± 2.19
P	0.5	SEG/Yes	4.06 ± 0.77	1.09 ± 0.49	2.96 ± 1.35	3.04 ± 1.60
P	0.2	SEG/Yes	4.05 ± 0.76	1.02 ± 0.43	3.56 ± 1.49	3.20 ± 2.00
U	0.5	SEG/No	4.05 ± 0.76	1.22 ± 0.49	2.47 ± 1.29	3.01 ± 1.78
U	0.2	SEG/No	4.05 ± 0.77	1.41 ± 0.49	2.98 ± 1.62	2.55 ± 2.05
U	0.5	SEG/Yes	4.05 ± 0.76	1.23 ± 0.49	2.55 ± 1.30	3.14 ± 1.88
U	0.2	SEG/Yes	4.05 ± 0.77	1.41 ± 0.49	2.96 ± 1.61	2.44 ± 1.98
P	0.5	NOSEG/No	1.00 ± 0.02	1.12 ± 0.55	1.16 ± 0.25	1.27 ± 0.43
P	0.2	NOSEG/No	1.00 ± 0.03	1.08 ± 0.45	1.30 ± 0.29	1.40 ± 0.53
P	0.5	NOSEG/Yes	1.00 ± 0.02	1.12 ± 0.55	1.16 ± 0.26	1.26 ± 0.36
P	0.2	NOSEG/Yes	1.00 ± 0.03	1.08 ± 0.44	1.31 ± 0.31	1.41 ± 0.50
U	0.5	NOSEG/No	1.00 ± 0.03	1.28 ± 0.58	1.30 ± 0.35	1.45 ± 0.42
U	0.2	NOSEG/No	1.00 ± 0.02	1.51 ± 0.51	1.51 ± 0.41	1.77 ± 0.83
U	0.5	NOSEG/Yes	1.00 ± 0.02	1.28 ± 0.59	1.28 ± 0.32	1.43 ± 0.39
U	0.2	NOSEG/Yes	1.00 ± 0.02	1.51 ± 0.52	1.54 ± 0.46	1.86 ± 0.95

Fig. 2.5.10 we show the $f_{\rm bound}$ evolution using the same symbols as in the previous figures. We include a linear fit to each pair of initial conditions with the form:

$$f(t) = m_f t + f_{\rm bound,ge}, \qquad t \geq \mathrm{TEXP}, \tag{2.15}$$

where m_f is the slope of the fit in units of Myr^{-1} and $f_{\rm bound,ge}$ is the bound fraction at the moment of gas expulsion. A summary table of both parameters is shown in Table 2.5.2. While all measurements are taken at the same times, i.e., at $t = 4.8$, 6.4, 8, 9.6, 11.2, 12.8, 13.4 and 16 Myr, they are slightly shifted for clarity.

In the top panel, the time evolution of $f_{\rm bound}$ is shown for simulations with equal-mass particles (triangles). For the four cases are observed practically constants $f_{\rm bound}$ values, as we measure two slopes with $m_f = -0.001$ for Plummer BG (P) and two slopes with $m_f = 0$ for uniform BG (U).

In the panels where simulation with No-SEv are shown, we observe in both cases negative slopes with values $-0.003 \leq m_f \leq -0.009$ independent on the initial conditions. SEG simulations under uniform BG potential with $Q_{\rm i} = 0.2$ show the steepest slope.

In the bottom panels, where simulations with SEv are shown, we observe even steeper slopes with values $-0.005 \leq m_f \leq -0.011$ also independent of the initial conditions. As in the central panels, we measure the steepest slope in the left panel under the same initial conditions.

The highest values of $f_{\rm bound}$ are shown in all cases at the moment of gas expulsion, and continuously decrease thereafter (SEG-NOSEG). In Fig. 2.5.11 and Fig. 2.5.12, we show again the average difference with the prediction but now compared with the value of $f_{\rm bound}$ measured at the moment of gas expulsion. At this moment, both Eq. 2.12 and Eq. 2.13 can closely describe our results, with the first prediction, compared with equal-mass results, still showing larger dispersion for early VT, but in the same range for later gas expulsion and, this is independent of the inclusion or not of SEv. The dispersion observed for the different cases at the moment of the gas expulsion are shown in Figs 2.5.6 and 2.5.6. We summarize in Tab. 2.5.2 the different fitting line slopes together with their respective $f_{\rm bound}$ at the moment of gas expulsion. We find that independent of the intrinsic characteristics in our sample, they show decreasing slopes, as stars are ejected. On a first order, models with a Plummer background potential have stronger slopes than uniform background potential. And to second order, star clusters with $Q_i = 0.5$ have steeper slopes than initially cold star clusters.

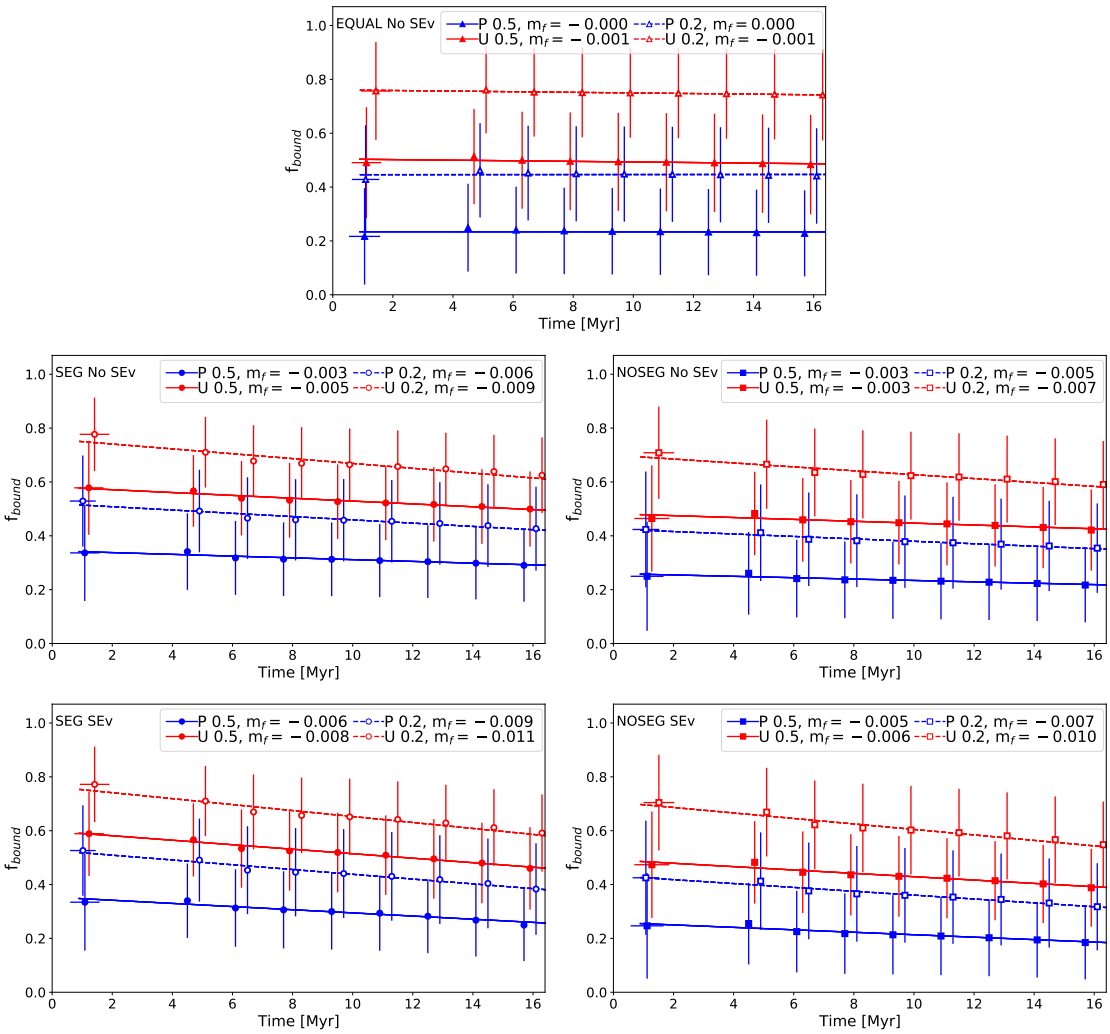

Figure 2.5.10: $f_{\rm bound}$ evolution in time. Colours and symbols are the same as in previous figures. The lines show linear fit according to Eq. 2.15 where the slopes m_f are indicated respectively in the legends.

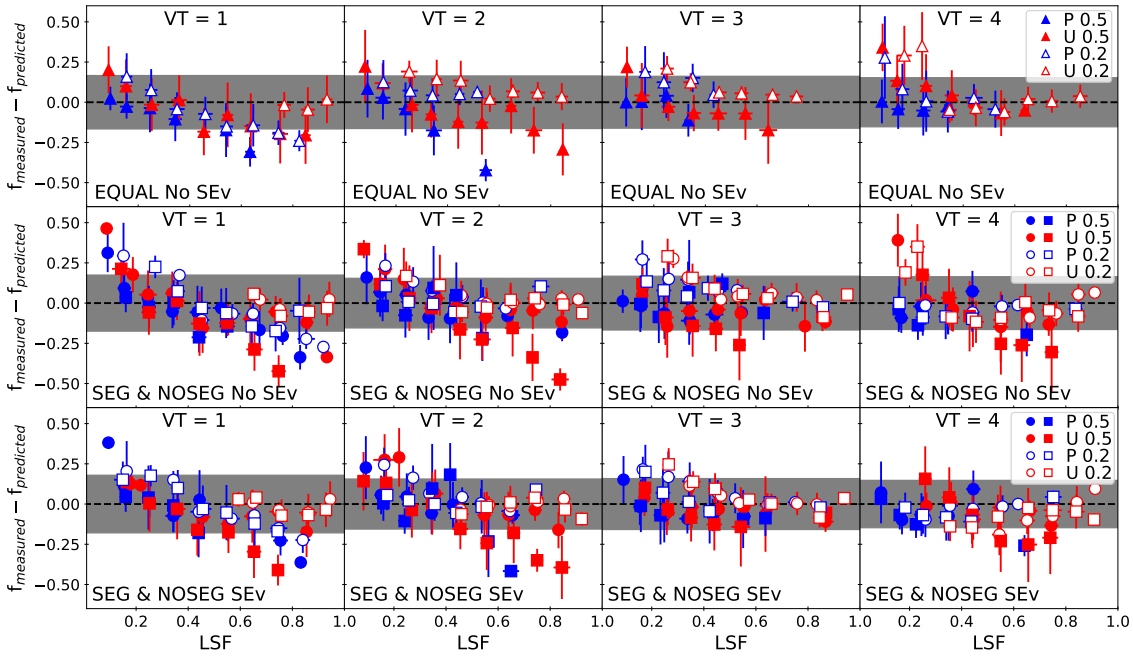

Figure 2.5.11: Same as Fig. 2.5.3 but for the moment of the gas expulsion.

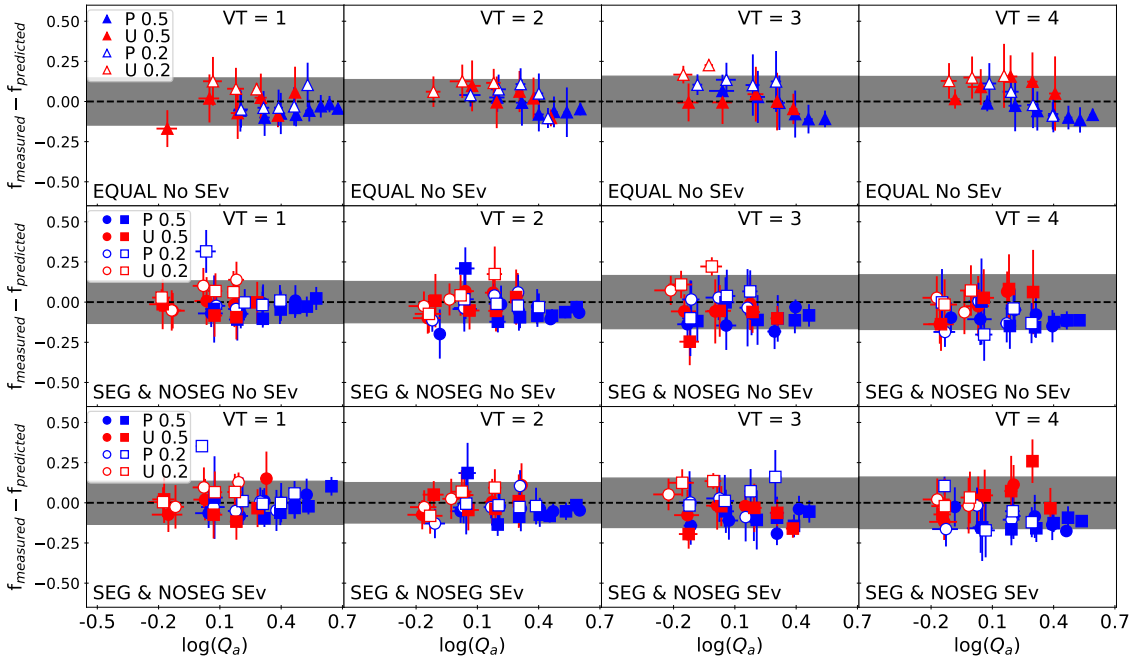

Figure 2.5.12: Same as Fig. 2.5.5 but now for the moment of the gas expulsion.

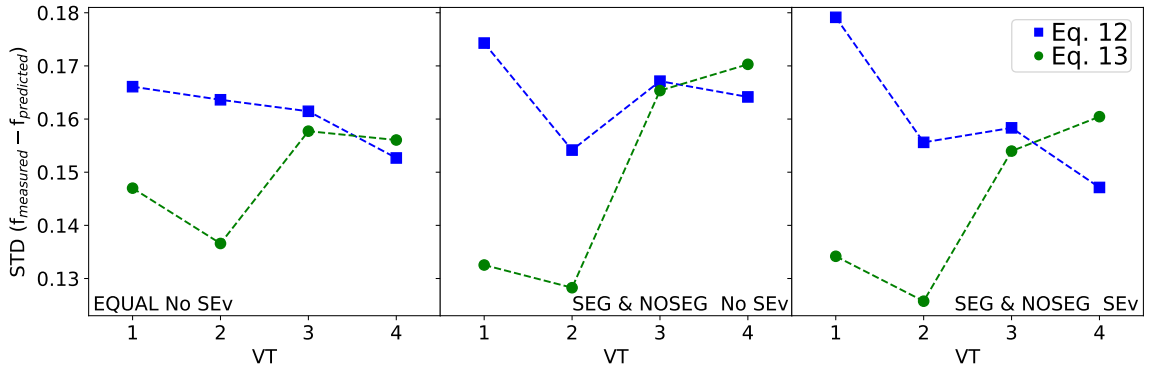

Figure 2.5.13: Same as in Fig. 2.5.6 but now $f_{\rm bound}$ is measured at the moment of the gas expulsion.

Table 2.5.2: Summary of fitting line slopes for $f_{\rm bound}$ time evolution. First and second columns indicate the BG potential (P = Plummer, U = uniform) with its respective initial virial ratio. The third column refers to the sample initial stellar distribution and if the stellar evolution is on. The fourth column shows the slope of the fitting line measured for each case. Last column shows $f_{\rm bound}$ at the moment of gas expulsion.

BG	$Q_{\rm i}$	Sample/SEv	m_f	$f_{\rm bound,ge}$
P	0.5	EQUAL/No	-0.003	0.23 ± 0.16
P	0.2	EQUAL/No	-0.006	0.44 ± 0.18
U	0.5	EQUAL/No	-0.003	0.48 ± 0.18
U	0.2	EQUAL/No	-0.006	0.74 ± 0.17
P	0.5	SEG/No	-0.003	0.29 ± 0.14
P	0.2	SEG/No	-0.006	0.43 ± 0.16
U	0.5	SEG/No	-0.005	0.50 ± 0.14
U	0.2	SEG/No	-0.009	0.62 ± 0.14
P	0.5	NOSEG/No	-0.003	0.22 ± 0.14
P	0.2	NOSEG/No	-0.005	0.35 ± 0.17
U	0.5	NOSEG/No	-0.003	0.42 ± 0.15
U	0.2	NOSEG/No	-0.007	0.59 ± 0.16
P	0.5	SEG/Yes	-0.006	0.25 ± 0.13
P	0.2	SEG/Yes	-0.009	0.38 ± 0.17
U	0.5	SEG/Yes	-0.008	0.46 ± 0.15
U	0.2	SEG/Yes	-0.011	0.59 ± 0.14
P	0.5	NOSEG/Yes	-0.005	0.18 ± 0.14
P	0.2	NOSEG/Yes	-0.007	0.32 ± 0.16
U	0.5	NOSEG/Yes	-0.006	0.39 ± 0.14
U	0.2	NOSEG/Yes	-0.010	0.55 ± 0.16

2.6 Summary & Conclusion

In this work, we test two models introduced by Farias et al. (2015) and Farias et al. (2018b), that predict the fraction of bound mass that star clusters can retain after explosive gas expulsion. These models were previously tested only using equal mass particle and fractal star clusters. Here, we explore how these models work on a more realistic scenario, introducing an IMF with two different particle distribution for the primordial location of massive stars. We first assume massive stars are born in random locations within the star cluster (NOSEG), and models with high levels of primordial mass segregation (SEG). In both cases, we also investigate the effects of SEv. We create a sample of 800 simulations to minimize stochastic fluctuations for every set and combination of the new parameters.

Since we use the latest version of the Nbody6++ code, we start by reproducing the previous results with equal-mass particles. In order to be consistent with recent evidence of a very early release of gas in low mass clusters ~ 1 Myr (Dinnbier and Walch 2020), we set the moment of gas expulsion at an early time.

The first predictive model, which depends on the local stellar fraction (LSF) and the pre-gas expulsion virial ratio, we find that the results are more accurate when star clusters expel their gas at later stages, i.e., when the level of substructure is reduced by dynamical processes, in agreement with our previous works. The second predictive model, that only depends of one parameter, the post-gas expulsion virial ratio, is not sensible to substructure, confirming previous results tested with highly substructured background gas models, and indicating that the nature of the background gas makes no difference for this specific model.

We introduce random IMF samples with different levels of primordial mass segregation as quantified by $\Lambda_{\rm MSR}$ and contrast with previous work. Star clusters with no primordial mass segregation, show a lower concentration of massive stars at the moment of gas expulsion compared to clusters with primordial segregation. Non segregated star clusters are still raising their concentration of stars when gas is removed, as reported in previous work using similar frameworks (see e.g.. Allison et al. 2010; Yu et al. 2011; Domínguez et al. 2017). We find an average $\Lambda_{\rm MSR} \sim 1.32$ implying that all clusters in this study are mass segregated at the moment of gas expulsion, regardless of the initial conditions.

After gas expulsion, $\Lambda_{\rm MSR}$ is observed for a short time to be even higher, followed by a continuous decrease due to cluster expansion. For the case of simulations with SEv, the SNe occurring in the second half of the simulation results in a steeper decrease.

By introducing random IMF samples, $f_{\rm bound}$ measurements at 16 Myr are in most of the cases below the predicted curves and with larger deviations when SEv is included. By examining the evolution in time of $f_{\rm bound}$, we observe a continuous decrease or a negative slope, also known as dynamical evaporation. The average values of $f_{\rm bound}$ are much closer to the predictions when they are measured at the moment of gas expulsion. For equal-mass particles the evaporation slopes are close to be zero, i.e., the predictions from the model are matched independent of the time we measure $f_{\rm bound}$ as it stays practically constant.

For simulations with SEv, at the moment of gas expulsion, we observe a similar trend. While SEv mass loss should decrease the bound mass, our simulations show that this is not

the case at early times. Our low mass clusters contain only a few very massive stars ($M > 20$ $M_\odot$) and only stellar winds change the mass at an early phase. These few massive stars evolve as SNe in the second part of the simulation and thus we only observe differences at later times.

We conclude that independent of the initial conditions, the predictive analytical models introduced by Farias et al. (2015, 2018b) can describe our results when measuring close to the gas expulsion time, but they overestimate $f_{\rm bound}$ at later stages. Dynamical evaporation due to two-body interactions is stronger in stellar systems having different stellar masses and it is the main reason for the continuous decrease of $f_{\rm bound}$. The inclusion of SEv can only decrease $f_{\rm bound}$ at later stages due to SNe mass loss. Moreover, no significant differences are observed at early times when only stellar winds take action. Initial mass distribution (SEG or NOSEG) does not play a role in our results. This is due to the fact that all clusters studied have rapidly become dynamically mass segregated, irrespective of the details of the initial conditions. We emphasize that the gas expulsion scheme studied here is the most destructive scenario and any smoothing applied to the process would improve the chances to find larger $f_{\rm bound}$.

Whether or not our initial conditions are a realistic state of an embedded star cluster is a matter of discussion. It has been shown that the pre-gas expulsion of a young massive star cluster ($M > 10^4$ $M_\odot$) is very compact (Marks and Kroupa 2012) and the number of substructures weakly depend on their total mass. An example of this is R136 in the 30 Doradus nebula with a total mass $> 2.2 \times 10^4$ $M_\odot$ with a radius poorly constrains to be ~ 2 pc. Authors (see e.g. Silich and Tenorio-Tagle 2017) also suggest that this object is not result of a single starburst and probably a (re)-collapse of gas which already gave birth to an older generation of stars where both together are part of NGC2070, and this scenario differs with the one developed here. In this work, the low mass embedded star clusters ($M = 2.5 \times 10^3$ $M_\odot$) show substructures at the moment of gas expulsion and these are decreasing as we wait to remove the gas. The aim of this chapter is to study if this non-spherical distribution helps the cluster to deal better with the violent gravitational potential change and to survive with SFE = 0.20 otherwise if we wait until the substructures are erased we would reproduce the same scenario largely study in Baumgardt and Kroupa (2007) with non-surviving clusters in this range of SFE.

3

Discovery of self-consistent survival of low star-formation efficiency clusters in evolving clouds: The coupling NBODY6 and WARPFIELD

In this chapter, we investigate the combined dynamical evolution of star clusters and their parent molecular clouds taking into account all relevant forms of stellar feedback. To do so, we couple the high-precision N-body code NBODY6++GPU with the one-dimensional stellar feedback model WARPFIELD which provides the time-varying background potential for the stellar dynamical evolution. This approach is considerably more realistic than the frequently used assumption of instantaneous gas removal. We model star cluster formation in molecular clouds of masses 10^5, 10^6, and 10^7 $M_\odot$, and study a large range of star formation efficiencies. We explore two key scenarios. The first one is the classical model, in which stars form in a single event and stellar feedback is able to disperse the surrounding cloud. In the second scenario, the star formation efficiency is smaller and the first cluster does not generate enough energy and momentum to disperse the cloud. Consequently, the cloud (re)-collapses, forming a new generation of stars. For the first scenario, we find that clusters can survive cloud dispersal even with global star formation efficiencies as small as $\epsilon_{SF} \lesssim 0.10$, which is contrary to the suggestions based on instantaneous gas expulsion. When (re)-collapse occurs, the dynamical evolution of the first generation of stars is strongly affected by the very high gas densities reached towards the centre. The change in the gravitational potential during the second expansion phase is larger than the initial one and leads to more rapid and further expansion of both stellar populations compared with the first scenario.

3.1 Motivation

As discussed in Sec. 1.3, studies have shown that embedded star clusters can survive instantaneous gas expulsion until approximately a minimum value of $\epsilon_{SF} = 0.15$. On the other hand, by ignoring the internal stellar dynamics, WARPFIELD has claimed that the star cluster embedded in massive uniform density molecular clouds can survive at any ϵ_{SF} value. In this chapter, we test their conclusion by adding responsive star clusters by means of N-body simulations reacting to the WARPFIELD evolving clouds. We keep our simulations as close as possible to the classical picture (see Sec. 1.2). In this sense, the main parameter changed is the gas and it evolutionary path but we also explore if different levels of mass segregation can change the output of surviving cluster at the moment when all the molecular cloud has been taken apart. WARPFIELD also allows consecutive star formation events when the specific initial conditions are achieved, i.e., some clouds are able to (re)-collapse and give birth to a second stellar generation. We also explore for this scenario which was not studied in the classical picture. In particular, we explore whether star clusters can survive after a second event of star formation and its posterior gas expulsion.

3.2 Method and Initial Conditions

We select different expansion and (re)-collapsing scenarios from WARPFIELD molecular clouds. The evolution of every cloud is followed using the code WARPFIELD 2.1 (Rahner et al. 2017). As the cloud is evolving, the gravitational potential is changing, which is included in the dynamics of the stars as an external potential. The trajectories of the stars are followed using the code NBODY6++GPU (Wang et al. 2015) modified for this purpose to read the information from the WARPFIELD output. WARPFIELD calculates the overall feedback produced by a star cluster located and remaining in the centre of the cloud. The amount of energy injected from the stars into the cloud produces its subsequent expansion. After that, the cloud can follow two different paths:

(i) The cluster injects enough energy dispersing the cloud.

(ii) The cluster does not produce sufficient energy and momentum, and consequently the cloud (re)-collapse after an initial expansion phase, giving birth to a new generation of stars.

(iii) The cloud (re)-collapse can be repeated several times until feedback disrupts the cloud.

In our current study, we focus on initial cloud conditions which lead to scenarios (i) and (ii). Our parameter space consists of molecular clouds with masses of 10^5, 10^6 and 10^7 $M_\odot$. The spherical clouds initially have uniform number density with values 1000 cm^{-3} $\leq n_0 \leq$ 10000 cm^{-3}, where the upper is due to current limitations of WARPFIELD. Since we are interested in embedded star clusters that survive with low ϵ_{SF}, for scenario (i), we choose the lowest ϵ_{SF} for which the specific cloud is not (re)-collapsing according to WARPFIELD calculations. The latter can be translated as slower or less disruptive gas ejection compared to the classical picture. We restrict our parameter space for ϵ_{SF} between 0.01 and 0.10, filling a zone where embedded star clusters have classically not survived after instantaneous

Table 3.2.1: Summary of parameter space explored in this chapter. The first column indicates the initial cloud masses and the second column shows the initial density of the clouds. We describe the first sample of simulation (expansion) between columns three to five and the second sample ((re)-collapse) between columns six to nine. The identifier (ID) is enumerated in columns three and six. The initial radii of the molecular clouds are shown in columns four and seven. The ϵ_{SF} for the embedded star clusters are shown in columns five and eight.

$M_{\rm cloud}$ ($M_\odot$)	n_0 (cm^{-3})	ID	R_i (pc) expansion	ϵ_{SF}	ID	R_i (pc) (re)-collapse	ϵ_{SF}	$T_{\rm col}$ (Myr)
10^5	10000	1	4.15	0.06	16	4.16	0.05	3.30
10^5	9000	2	4.30	0.06	17	4.31	0.05	5.68
10^5	8000	3	4.49	0.05	18	4.50	0.04	3.38
10^5	7000	4	4.69	0.05	19	4.71	0.04	5.58
10^5	6000	5	4.96	0.04	20	4.97	0.03	3.60
10^5	5000	6	5.27	0.04	21	5.28	0.03	6.18
10^5	4000	7	5.69	0.03	22	5.71	0.02	3.95
10^5	3000	8	6.27	0.03	23	6.29	0.02	7.67
10^5	2000	9	7.20	0.02	24	7.22	0.01	4.89
10^5	1000	10	9.10	0.02				
10^6	4000	11	12.05	0.08	25	12.13	0.07	5.63
10^6	3000	12	13.36	0.07	26	13.40	0.06	13.22
10^6	2000	13	15.34	0.05	27	15.40	0.04	9.55
10^6	1000	14	19.47	0.03	28	19.53	0.02	9.25
10^7	1000	15	41.21	0.08	29	41.35	0.07	13.69

gas expulsion. In this work, we only study scenarios (i) and (ii).

From WARPFIELD outputs we obtain the evolution of the boundary conditions between the wind-bubble expanding-shell and ambient inter stellar medium (ISM) pressures, accounting for varying H-ionization, density and temperature. We also solve for the self-consistent radiation which leaves the expanding-shell, heating the outer part of the molecular cloud over the cluster/cloud life-time, or the ambient ISM if the cloud is fully swept. The shell stature calculated by WARPFIELD assumes a quasi-hydrostatic evolution, the same as the 1D radiative transfer and chemistry code CLOUDY (Ferland et al. 2017). The density profile of the cloud is solved by assuming the hydrostatic-equation of state of Abel and Ferland (2006), which has been shown to explain the structure of nearby HII regions (Pellegrini et al. 2007, 2009, 2011a). However, the micro-physics within CLOUDY is more complete than WARPFIELD, and thus to get a more accurate shell radial profile of density, temperature and ionization fractions we recompute the physical conditions using CLOUDY taking as inputs the boundary conditions from WARPFIELD. This involves solving for the total sum of all forces including the gravity of the gas and star cluster, as well as the radial gradient in gas pressure and absorbed stellar radiation. The initial cloud conditions, such as inner radius and pressure/density are provided by WARPFIELD assuming the interior wind bubble is in pressure balance with the inner edge of the HII region. These force terms are matched internally so that the gradient in internal pressure sources from gas, magnetic field and turbulence exactly offset the local force due to gravity and external feedback. We use CLOUDY to solve for these again after WARPFIELD because the density and temperature of the cold gas depend on chemistry is not included in WARPFIELD. The densities are typically slightly higher than before, as the gas has more cooling channels with more complex chemistry. The WARPFIELD dynamics is unaffected by these modifications but we include the sharper density profiles as they may affect stellar dynamics.

We end up with radial density profile information, using the equation of hydrostatic balance (Abel and Ferland 2006; Pellegrini et al. 2007), for different times along the cloud evolution. To calculate the potential and the forces, we solve the Poisson equation:

$$\nabla^2\phi(r) = 4\pi G\rho(r), \tag{3.1}$$

where $\phi(r)$ is the radial gravitational potential produced by the cloud, G the gravitational constant and $\rho(r)$ is the radial density obtained from CLOUDY reduction. From the potential calculation, we obtain the radial force $F(r)$ as:

$$F(r) = -\frac{d}{dr}\phi(r). \tag{3.2}$$

As a way of illustration, we describe how WARPFIELD proceeds with an example of a cloud which initially has $M_{\rm cloud} = 10^6$ M$_\odot$ and $n_0 = 2000$ cm^{-3}. At $t = 0$, WARPFIELD forms a star cluster in the centre of the molecular cloud. The embedded star cluster for this example has a $\epsilon_{SF} = 0.05$, i.e., $M_{\rm cluster} = 50000$ M$_\odot$. The molecular cloud is now less massive as the cluster is taking mass from the gas. The WARPFIELD calculations continue assuming a stellar

distribution remaining close to the centre of the molecular cloud. All feedback from the most massive stars is injected into the surrounding gas which consequently is pushed outwards. The radial acceleration experienced by the expanding molecular cloud at different times is shown in the top panel of Fig. 3.2.1. The different colours refer to different times. At the very beginning, the initial density distribution of the cloud is uniform and the different cloud layers experience increasing acceleration with increasing radius. As the gas is getting expelled from the centre, an internal zone without gas or an empty bubble is produced. Inside this zone, the summation of forces is equal to zero, as we are working with a spherical model. Next to the bubble, a shocked wind zone is produced followed by the shell. This zone accumulates more as it expands outwards after ∼0.11 Myr. Next to the shell, there is a part of the cloud remaining not yet swept (for an illustration of this physical structure, see Figures 1 and 2 of Rahner et al. 2017). The bubble gets bigger until reaching the shell at ∼0.60 Myr. The cloud continues expanding until it gets dispersed ($\gtrsim$ 10 Myr). The bottom panel shows the corresponding shell and bubble radii as a function time. In this panel, it is better observable when the bubble (cyan dashed line) reaches the shell (green solid line) and the subsequent joint expansion. The different colour points show the times for forces calculations. The colours are related one to one with the lines in the top panel.

To model the evolution of the molecular clouds, we first run the 29 WARPFIELD models enumerated in Tab 3.2.1. To initiate the stellar dynamical evolution of the star clusters, we randomly create 10 different Plummer distributions (see 2.3) with a scale length of 1 pc using MCLUSTER (Küpper et al. 2011). We use this scale length as it was used by the studies presented in Section 3.1 and it is also supported by observations (Pfalzner et al. 2016). The star masses are generated according a Kroupa (2001) IMF as follows:.

$$N(M) \propto \begin{cases} M^{-0.30} & m_0 \leq M/\mathrm{M}_\odot < m_1 \\ M^{-1.30} & m_1 \leq M/\mathrm{M}_\odot < m_2 \\ M^{-2.30} & m_2 \leq M/\mathrm{M}_\odot < m_3 \end{cases} , \tag{3.3}$$

with $m_0 = 0.08$, $m_1 = 0.1$, $m_2 = 0.5$, $m_3 = 120$ $\mathrm{M}_\odot$. Using this IMF, we obtain a total number of stars between $10^3 - 10^6$, and a average stellar mass of 0.5 $\mathrm{M}_\odot$. For the most massive clusters, we exclude stars with masses smaller than m_1 to keep simulation time affordable. WARPFIELD do not include the exact feedback of the particular generated star clusters. WARPFIELD uses instead the average feedback of a generic star cluster with the same total mass.

After producing the mass sample we assign them to the N-body particles differently to obtain star clusters with initial mass segregation (SEG) and without (NOSEG). We define a SEG or NOSEG star clusters according to Allison et al. (2009b) using the Λ_{MSR} parameter where a value $\Lambda_{\mathrm{MSR}} \sim 1$ means no mass segregation and a value of $\Lambda_{\mathrm{MSR}} \gg 1$ means the clusters is mass segregated. The maximum values of mass segregation used is this study are $\Lambda_{\mathrm{MSR}} \sim 3$ as Allison et al. (2009b) found as realistic. The thread hold mass between low mass and massive stars is $M = 20$ $\mathrm{M}_\odot$. The star clusters for SEG and NOSEG stellar distributions have identical star masses. The masses resulting from the IMF samples are rearranged to

achieve the two different initial states.

We control the initial state of the embedded star clusters using the virial ratio [1] defined as:

$$\alpha = \frac{T}{|\Omega|}. \tag{3.4}$$

This means the ratio between the kinetic energy (T) and the total gravitational potential (Ω). For embedded star clusters the gravitational potential is also taking into account the interaction between stars and gas.

All our embedded star clusters start in viral equilibrium, with $\alpha = 0.5$ and consequently they should remain in this state or at least oscillate around the equilibrium state. However, expanding clouds remove a significant part of the system's gravitational energy, and as a consequence causes the naked star cluster to expand.

We run our simulations in different ways, depending on whether we are working with expanding or (re)-collapsing clouds. For expanding clouds we proceed as follows:

- We locate 10 different Plummer spheres with SEG mass distribution for each corresponding cloud model.
- We scale the star velocities in order that the embedded star clusters are in equilibrium with the gas.
- We run further in time for 14 Myr.
- We proceed as before but now with NOSEG mass distribution.

We run the simulations for 14 Myr because by this age all the stars with masses $M_{\rm star} > 20$ $M_\odot$ are gone as SNe, and the clouds have either large shell radii or else are already dissolved. We summarize the parameter space in Tab. 3.2.1 between columns first and fifth (ID 1-15).

For (re)-collapsing clouds, we proceed similarly but with a smaller sample. We reduce ϵ_{SF} in 0.01 and as a consequence the clusters do not produce enough amount of feedback to keep the clouds expanding, resulting in a (re)-collapse scenario. The timing of the second stellar generation depends on the initial conditions, (such as the initial gas and stellar mass) and it is an output from WARPFIELD modeling. The total mass of the new clusters are chosen to be the minimum required to do not produce a second (re)-collapse, i.e. the gas cloud is pushed away by the feedback produced by the two coexisting stellar generations. For this scenario, we use also 10 different Plummer distributions but 5 for the first generation and 5 for the second generation as follows:

- We locate 5 different Plummer spheres with SEG in each corresponding cloud model.
- We scale the star velocities in order that the clusters start in equilibrium with the gas.
- We run further in time until the cloud is just about to create the second stellar generation.
- We add a second Plummer sphere with SEG stellar distribution to the simulation.
- We scale their velocities so that the second cluster is in equilibrium.

[1] We use the symbol α in this and following chapter to agree with the latest literature.

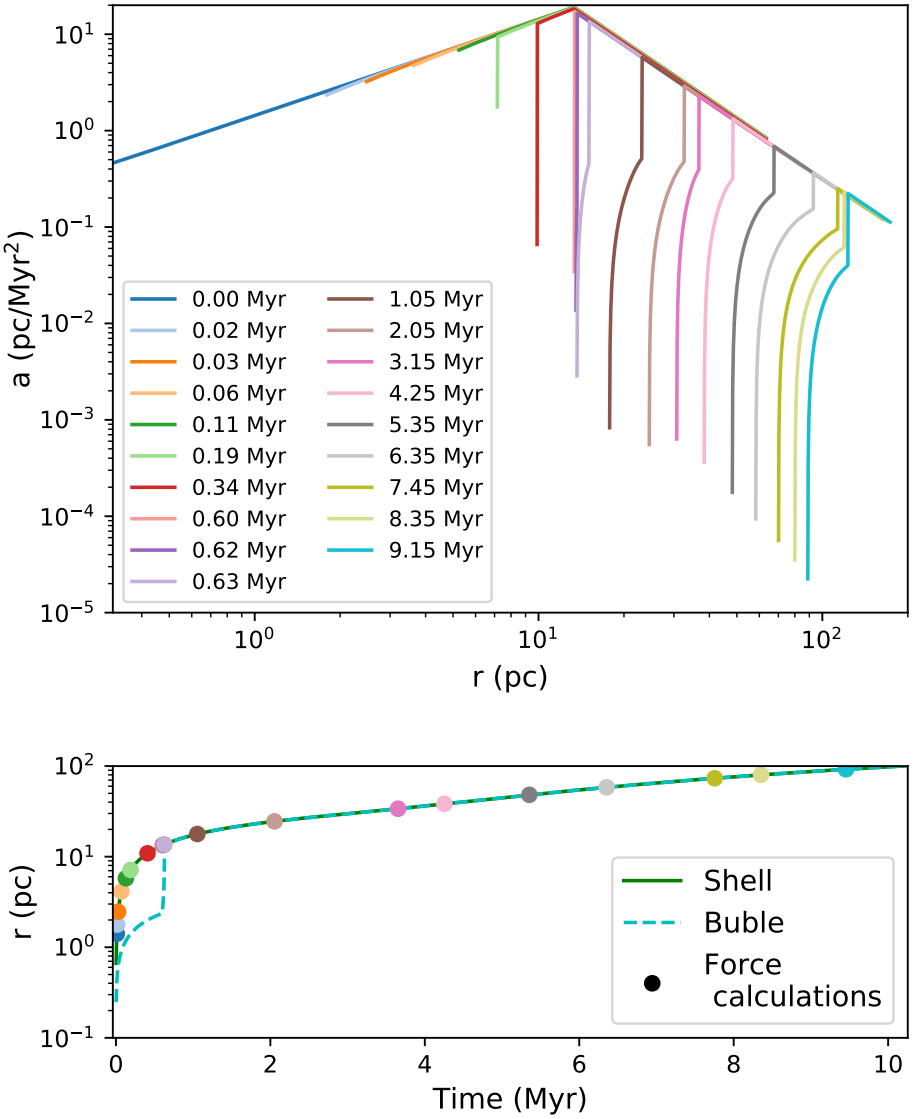

Figure 3.2.1: The top panel shows the radial acceleration that a particle experiences for different times in a cloud modelled by WARPFIELD. The example cloud has an initial mass of $M_{\text{cloud}} = 10^6$ M$_\odot$ with $n_0 = 2000$ cm^{-3}. There is a cluster with mass $M_{\text{cluster}} = 50000$ M$_\odot$. After the birth of the stars the global $\epsilon_{SF} = 0.05$. The different colours denote different times described in the legend. The bottom panel shows the radial evolution in time of the bubble (cyan dashed line) and the shell (green solid line). The colour points are one to one related with the line time values in the top panel.

- We continue the simulations until reach 20 Myr.
- We proceed again in the same way for clusters with NOSEG mass distribution.

At 20 Myr we observe, as before, that the shell has expanded far into the ambient ISM and has dissolved. In this scenario, if the (re)-collapse is early, the most massive stars from the first generation (1GEN) and second generation (2GEN) can coexist, producing larger quantities of feedback. On the other hand, when the (re)-collapse is late enough, the most massive stars from 2GEN dominate the injected energy into the cloud. We note again for the systems studied here, initial conditions do not lead to the formation of a third generation of stars. The information for this sample is summarized in Tab. 3.2.1 shown between columns six and nine, coupled with first and second (ID 16-29).

The total kinetic energy of the cluster after adding 2GEN is $T = T_{\rm 1GEN} + T_{\rm 2GEN}$ and the total gravitational potential is $\Omega = \Omega_{\rm 1GEN\text{-}2GEN} + \Omega_{\rm 1GEN\text{-}Gas} + \Omega_{\rm 2GEN\text{-}Gas}$ where the interactions between stars from different generations (1GEN-2GEN) and stars with gas (1GEN-Gas and 2GEN-Gas) are included. We scale the velocities only for 2GEN stars to achieve its equilibrium as:

$$\alpha_{\rm 2GEN} = \frac{T_{\rm 2GEN}}{|\Omega_{\rm 1GEN\text{-}2GEN} + \Omega_{\rm 2GEN\text{-}Gas}|} = 0.5, \tag{3.5}$$

excluding $T_{\rm 1GEN}$ and $\Omega_{\rm 1GEN\text{-}Gas}$ as they cannot influence the conditions at the moment of 2GEN birth.

To be consistent with WARPFIELD calculations, we modify the stellar evolution feature from NBODY6++GPU. Massive stars explode as SNe when they reach their maximum age according to Ekström et al. (2012). After that time, NBODY6++GPU locates a remnant according to its SNe scheme. A more complex scheme is also included in NBODY6++GPU based on (Hurley et al. 2000), which is not used in this study as WARPFIELD does not include this detailed evolution.

Although we are mostly interested in massive stars, which are producing most of the feedback ($M_{\rm stars} > 20$ M$_\odot$), we keep SNe treatment during the whole simulation, i.e., stars under this threshold are evolving as SNe if they reach their respective ages. In the N-body dynamics, we neglect stellar mass loss by winds, in consequence, the only source of mass loss that the star clusters experience is due to SNe or escaping stars.

3.3 WARPFIELD models

The quantity of energy injected into the cloud by the WARPFIELD modelling is mostly coming from the most massive stars (M $\geqslant$ 20 M$_\odot$) which are assumed to remain located close to the centre or at least inside of the molecular cloud shell. The last assumption is tested in this section.

3.3.1 Massive stars central distance

We use the simulations shown in Tab. 3.2.1, and measure the average distance of stars with $M \geqslant 20$ M$_\odot$ from the cluster centre weighted by their generic luminosity according to

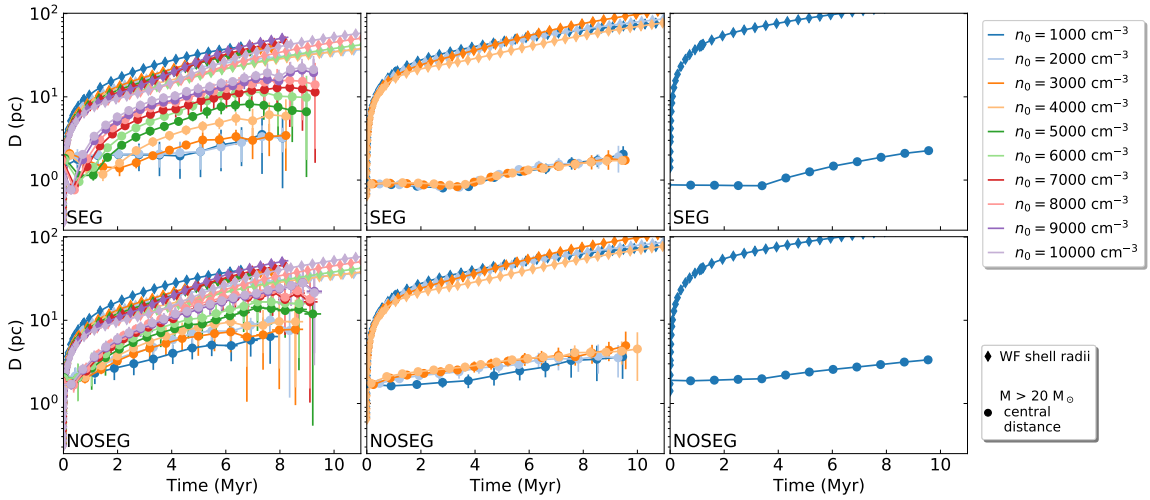

Figure 3.2.2: Central distance of massive stars ($M \geqslant 20$ M$_\odot$) evolving in time. Left panels show simulations for cloud with $M = 10^5$ M$_\odot$, middle panels for cloud with $M = 10^6$ M$_\odot$ and right panels for cloud with $M = 10^7$ M$_\odot$. In the top panels the clusters start initially segregated (SEG) and bottom panels are for simulations starting with non mass segregation (NOSEG). Top lines (diamond symbol) in every plot are the different shell radius evolution taken from WARPFIELD and the bottom lines (circle symbols) are the average massive stars central distance weighted by luminosity. Colour lines represent the different initial cloud densities.

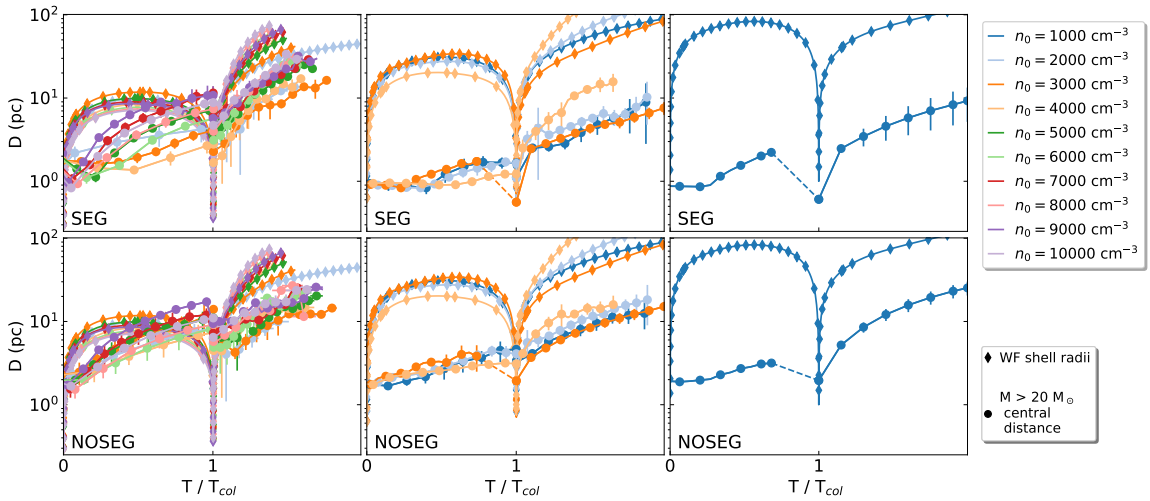

Figure 3.2.3: Colours and symbols are the same as in Fig. 3.2.2 but now for COL clouds. Simulation time is normalized by the (re)-collapsing time (T_{col}).

Gräfener et al. (2011) to compute the total feedback energy and momentum input. We study the time evolution of the central average weighted distances separately for the expanding and (re)-collapsing clouds.

In Fig. 3.2.2 we depict the result for the expanding models with the top row indicating the evolution of the mass-segregated (SEG) and the bottom row showing the non-segregated (NOSEG) clusters. The left, middle and right panels are for initial cloud masses of $M_{\rm cloud} = 10^5$ M$_\odot$, $M_{\rm cloud} = 10^6$ M$_\odot$ and $M_{\rm cloud} = 10^7$ M$_\odot$, respectively. The average central distances of the massive stars (bottom lines, circle symbols) are compared with the shell radius (top lines, diamond symbols). The different colours indicate the initial cloud density (n_0). In the beginning, the shell clouds are expanding faster than the massive stars in all cases. The average central distances in the left panel after a small oscillation are continuously increasing, getting closer to the shell in later times. In the middle and right panels, the average central distances appear to initially shrink, but they increase as soon as the SNe set in, which happens for stars of $M = 120$ M$_\odot$ at ∼3.6 Myr (Ekström et al. 2012). The average weighted central distances for these two cases are never approaching the radius of the driven wind/HII region shell interface. Also in the case of NOSEG initial stellar distributions, the clusters always remain inside the expanding shell. However, this expansion starts from larger initial central distances.

In the central and right panels, the expansion effect by stellar evolution observed in the top panels is not as visible as before. The NOSEG distributions produce that the SNe remove gravitational potential throughout the entire cluster, which is affecting the stellar distribution softer. For SEG distributions, the gravitational potential is removed from locations closer to the centre, which is more destructive for the star clusters. As their SEG pairs, the average weighted central distances are always much lower than the shell clouds. At the end of the simulations, both configurations show similar final central distance expansions for their massive stars.

In Fig. 3.2.3 are shown the results of central average weighted distances for (re)-collapsing clouds. As the (re)-collapses occur at different moments for each cloud (see Tab. 3.2.1 column nine), the simulation times are normalised by the (re)-collapsing time ($T_{\rm col}$). The evolution after the (re)-collapse is scaled as (20-$T_{\rm col}$)/$T_{\rm col}$. This is more suitable for direct comparison. The six panels follow the same order as Fig. 3.2.2. As the clouds expand, and their gravitational potential decreases, we observe that the central average weighted distances increases in all cases. On the left column, the central average weighted distance (circle symbols) for SEG and NOSEG models, can be larger than the cloud shell (diamond symbols), but this only occurs during the short phase of cloud (re)-collapse. After the formation of the second generations of stars, the clouds expand again and the shell quickly reaches larger radii. For the computation of the central average weighted distances after (re)-collapse, we include both stellar generations. Again, the massive stars remain comfortably within the expanding bubble. In central panels, independent of the initial stellar distribution, the central average weighted distances never reach values larger than the shell. This is also observed in the right panels. As before the final expansion is similar between SEG and NOSEG pairs.We clarify that in the middle and right panels, the dashed line connects the

Parameter	This study	Baumgardt and Kroupa (2007)
Background potential	Initially uniform	Plummer
Virial ratio	0.5	0.5
Stars distribution	Plummer	Plummer
Mass segregation	Yes and no	No
Stars' effective radius	1.0	1.0
Gas expulsion	Expanding or (re)-collapsing WARPFIELD cloud	Instantaneous
Initial star formation efficiency	0.01-0.10	0.33
Star formation events	1 and 2	1

Table 3.3.1: Parameter comparison used in this chapter and by Baumgardt and Kroupa (2007) (classical picture).

time evolution in simulation with $T_{col} > 10$ Myr. At these times, the first stellar generation (1GEN) has no more stars with masses M> 20 M$_\odot$, and so no information of central distance can be measured until the birth of the second stellar generation (2GEN).

We observe that independent of the cloud evolution (expansion or (re)-collapse), ϵ_{SF}, n_0 or stellar initial distribution the central average weighted distances are always smaller than the cloud shell, i.e., the most massive stars always remaining inside of the shell radius. This fact supports the spherical 1D approach adopted in the WARPFIELD model which injects all feedback energy and momentum at the centre of the system without taking into account the stellar dynamical evolution of the cluster.

3.4 Comparison of the initial conditions with the classical picture

In this chapter, two main variations from the classical picture are explored. We change the idea of an instantaneous gas expulsion, instead we leave that side of the embedded star cluster evolution to WARPFIELD which continuously update the shape of the gas. The gas initially start with an uniform density profile but it changes radially through the simulation as we previously show in Fig. 3.2.1. The second change, and barely explored in the literature, is the inclusion of a second star formation event, which is only possible to produce due to the WARPFIELD cloud evolution mode. In Tab. 3.3.1 we summarize the differences between this study and Baumgardt and Kroupa (2007). As before, we keep the rest of the global set up close to the classical picture to compare with previous results.

3.5 Results

In this section, we study the evolution of the Lagrangian radii (R$_f$) for all simulations considered in this study. We analyse what fraction of the clusters survive after realistic gas removal as modelled with WARPFIELD. It is important to mention that our sample is located in a ϵ_{SF} range where, as discussed in Section 3.1, the consensus of the literature is that embedded star clusters are not supposed to survive. We study the different behaviours divided by initial cloud mass, initial stellar distribution, and cloud evolution. We refer to an initial cloud mass

of $M_{\rm cloud} = 10^5$ M$_\odot$ as M5, $M_{\rm cloud} = 10^6$ M$_\odot$ as M6 and $M_{\rm cloud} = 10^7$ M$_\odot$ as M7. All figures in each expansion subsection show the Lagrangian radii evolving in time for 0.1, 0.3, 0.5, 0.6, 0.7, 0.8 and 0.9 from bottom to top denoted by different line colours and the respective shell radius. To connect to the existing literature, we compare with the R$_f$ values from gas-free star clusters and from clusters which are subject to the classical violent gas expulsion. One can consider these gas-free clusters as a means to assess a lower limit to expansion. Even gas-free clusters which are initially in equilibrium eventually expand, as a result of mass loss from SNe, but this effect is far too small to dissolve the clusters. As the clusters are continuously decreasing in mass by SNe mass loss, one or more of the outer R$_f$ can not be reached during the entire simulation time. We can not rule out ejections from dynamical interactions, but we assume they are negligible for gas-free clusters. We compare for each sample R$_f = 0.5$ and the outer R$_f$ which can be followed during the whole simulation. The outer R$_f$ varies depending on the initial $M_{\rm cloud}$. The mass loss by stellar evolution is higher when there are more massive stars and this happens when the IMF sample is better filled. The outer R$_f$ for M5, M6 and M7 are R$_f = 0.8$, 0.7 and 0.6, respectively. The initial values for R$_f = 0.5$ to 0.8 are $\sim$ 1.30, $\sim$ 1.56, $\sim$ 1.92 and $\sim$ 2.50 pc, respectively, and this is for all cases, as they are following Plummer distributions with the same scale length. The respective final values for the respective R$_f$ are summarized in Tab. 3.5.1 for a better appreciation. The first column shows the initial $M_{\rm cloud}$, the second column indicates the initial stellar distribution, and if the star clusters are embedded (Yes) or if they are free of gas (No). The third column shows n_0 for simulations with gas, the fourth column is R$_f = 0.5$ and the last column is the outer R$_f$. We first analyze R$_f$ behaviour for the expansion sample.

For the (re)-collapse sample, we analyze R$_f = 0.5$ separated by generation. We summarize the final values of R$_f = 0.5$ in Tab. 3.5.2. We do not have simulations with $n_0 = 1000$ and ϵ_{SF} = 0.01, because the (re)-collapse happens at $\sim$ 20 Myr, which is not giving information about 2GEN, as our simulation time is shorter. In order to do not overcrowd the figures, we skip some of R$_f$. For this sample, we only plot 0.1, 0.3, 0.5, 0.7 and 0.8 from bottom to top in different colours. Solid lines with filled symbols are for 1GEN and dashed lines with open symbols for 2GEN. As before, the cloud shell is plotted with a dashed black line.

3.5.1 M5 cloud expansion

Figure 3.5.1 shows in the left and central panels the average R$_f$ evolution for clusters with SEG (filled circles) and NOSEG (empty circles) initial stellar distributions under the influence of their respective WARPFIELD clouds. For M5, the same value of ϵ_{SF} is enough to expand clouds which differs in n_0 by 1000 cm^{-3}. The shell (dashed black line) dissolves faster for the simulations with lower n_0, which is expected since the same clusters encounter less resistance in a low density cloud. In order to study if the clusters survive under these conditions, we plot in the right panels R$_f$ evolution for gas-free clusters (triangles) and cluster with instantaneous gas expulsion (diamonds) also for SEG and NOSEG. For the cases with instantaneous gas expulsion, we use the classical picture and the gas follows also a Plummer profile. In this scenario, for this range of ϵ_{SF}, the gas expulsion is extremely violent and the clusters do not survive. This last scenario can be observed in each of the right panels, as the

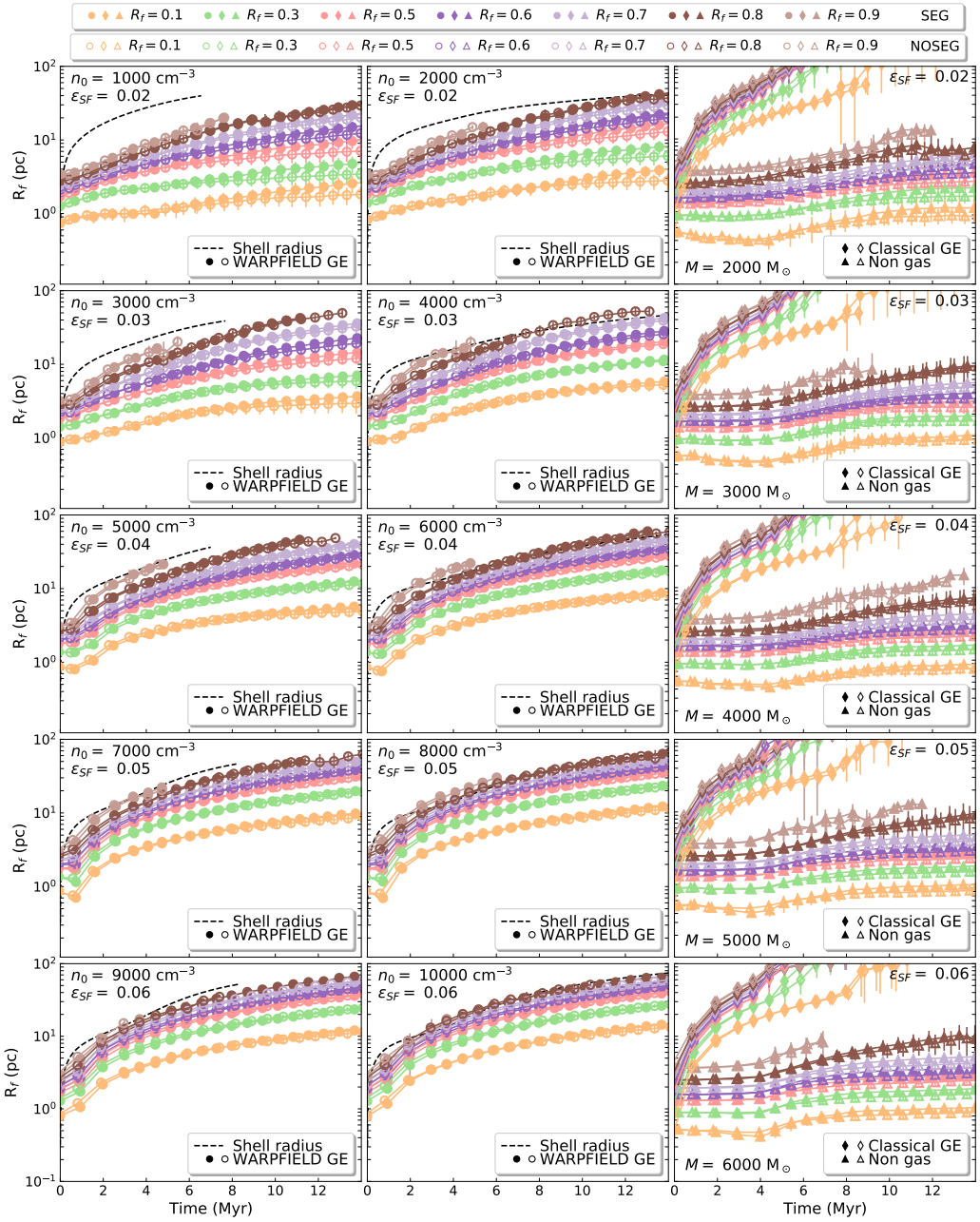

Figure 3.5.1: Left and central panels show the R_f evolution of a cluster under the influence of WARPFIELD gas expulsion (circle symbols) corresponding to each initial density (n_0) and ϵ_{SF} respectively for clouds with an initial mass of $M_{\rm cloud} = 10^5$ M$_\odot$. Right panels show, as a mode of comparison, the same clusters with non gas influence (triangle symbols). Right panels also show the same cluster under classical gas expulsion (diamonds symbols). The different colours refer to each Lagrangian radii ($R_f = 0.1$, 0.3, 0.5, 0.6, 0.7, 0.8 and 0.9) increasing from the bottom. The cluster starting with initial mass segregation (SEG) are shown with filled symbols and clusters without initial mass segregation (NOSEG) with empty symbols. Black dashed lines in left and central panels correspond to the shell radius.

different R_f reach much higher values than for gas-free clusters.

We observe that our clusters in the left and central panels expand due to WARPFIELD gas expulsion. Some stars escape due to expansion and this can be observed since $R_f = 0.9$ is cut off earlier than for the gas-free simulations. As they are the same clusters the stellar evolution by SNe mass loss is identical. In some cases, even $R_f = 0.8$ is gone in late stages. The expansions are universally less than the classical picture painted by instantaneous gas expulsion.

As we have a large sample, we divide M5 sample into two n_0 ranges. The first range is for $n_0 \leq 6000$ cm^{-3} and the second ranges is $n_0 \geq 7000$ cm^{-3}.

Star clusters in the first range can retain at 14 Myr. The 50% of their mass is inside of 19.31 $\pm$ 6.67 pc, in addition, they have a $R_f = 0.8$ of 35.21 $\pm$ 2.18 pc, which in comparison with the gas-free clusters, with the same masses, they can retain 50% of their mass inside of 3.14 $\pm$ 0.46 pc with a $R_f = 0.8$ of 9.14 $\pm$ 0.77 pc.

For clusters in the second range, the expansions are stronger. At 14 Myr, $R_f = 0.5$ is 31.51 $\pm$ 5.68 pc and $R_f = 0.8$ of 57.15 $\pm$8.66 pc. Gas-free clusters have a $R_f = 0.5$ of 2.82 $\pm$ 0.17 pc and $R_f = 0.8$ of 9.22 $\pm$ 0.76 pc.

All our embedded star clusters under WARPFIELD gas expulsion continuously expand but only in a few occasions, $R_f = 0.9$ reaches locations outside of the cloud shell. Our models expand more than gas-free star clusters but much less than embedded star clusters under violent gas expulsion.

SEG and NOSEG simulations (filled and empty symbols) show very similar behaviour as we observe both curves over-plotting them most of the time. The star clusters with NOSEG expand slightly less than their SEG pairs with average differences less than 5 pc for the outer skirts and less than 2.5 pc internally. We summarize the specific averages by ranges in Tab. 3.5.1 including embedded star clusters under instantaneous gas expulsion and gas-free clusters for direct comparison.

3.5.2 M6 cloud expansion

Figure 3.5.2 shows in left panels the R_f evolution for clusters with SEG (filled circles) and NOSEG (empty circles) initial stellar distributions under the influence of their respective WARPFIELD clouds. For M6, the ϵ_{SF} varies for the different cases n_0, in at least 1% to continuously expand the cloud. As before, we show in the right panels the R_f evolution for gas-free clusters (triangles) and under violent gas expulsion (diamonds). The difference between M5 and M6 violent gas expulsion is that in these cases are much stronger with $R_f = 0.1$ larger than 100 pc at $\sim$4 Myr. In most cases, the simulations do not continue as the clusters get dissolved. For these cases, the gas which is following a Plummer distribution is much denser, and when it is removed, it is taking a very large part of the gravitational potential leaving the clusters very out of equilibrium. It is possible to observe that for the gas-free clusters cases $R_f = 0.9$ and $R_f = 0.8$ are cut off before than in M5 case. For these massive clusters ($M_{\rm stars} \geq$ 30000 $M_\odot$), the IMF sample is fully completed, and more massive stars are present, which

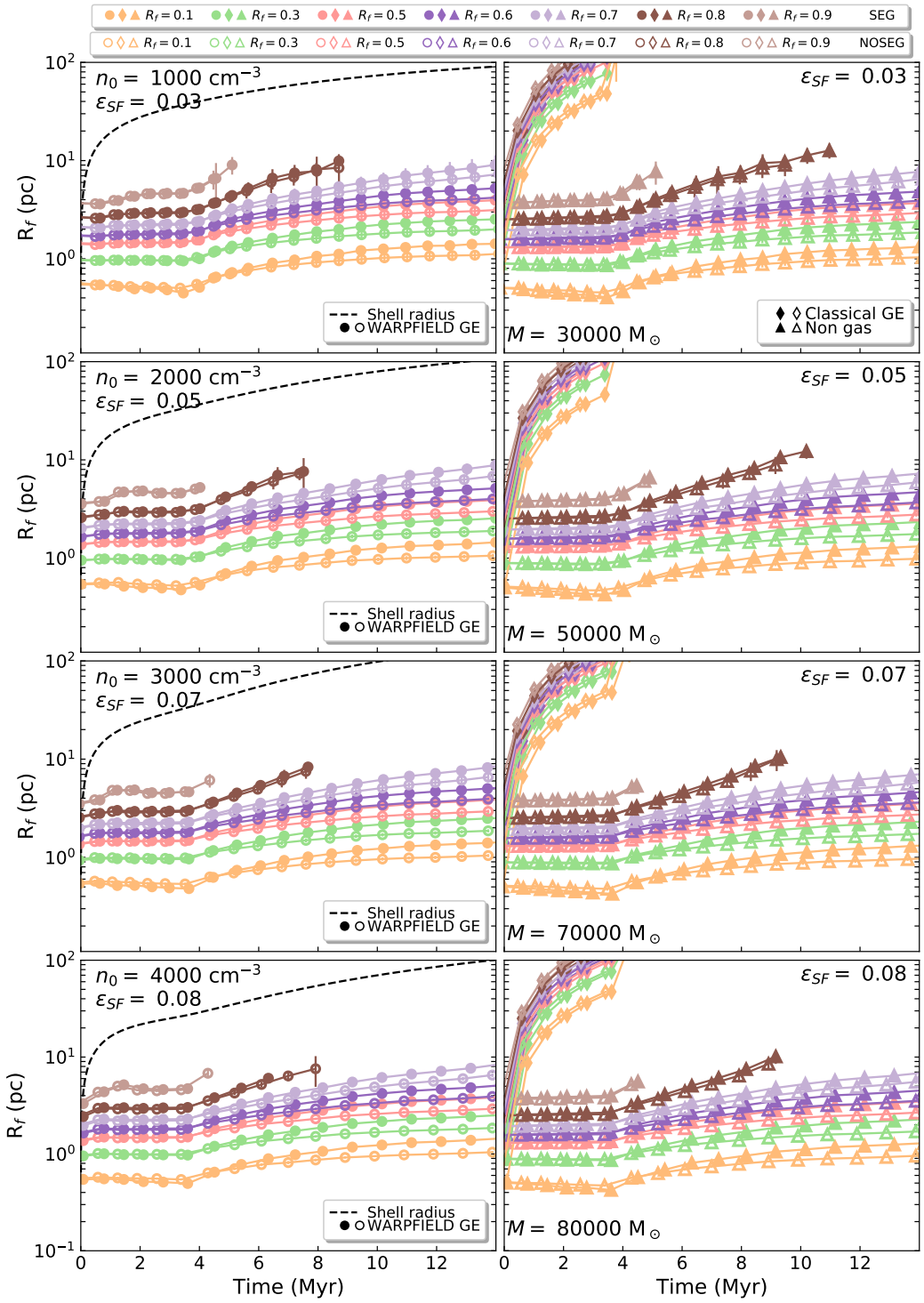

Figure 3.5.2: Left panels show the evolution of a cluster under the influence of WARPFIELD gas expulsion. Colours, symbols and right panels are as in Fig. 3.5.1 but now for M6 sample.

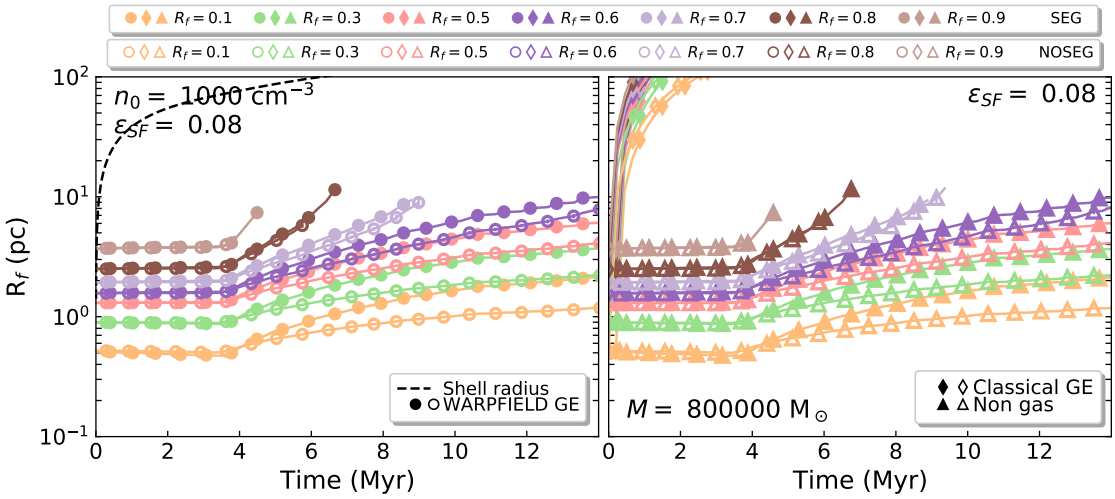

Figure 3.5.3: Colours and symbols are the same as in Fig. 3.5.2 but now for the M7 sample.

are producing more SNe and larger mass loss. The differences between left panels simulations and gas-free clusters evolution are difficult to observe. In every pair, $R_f = 0.9$ and $R_f = 0.8$ are cut earlier. In left panel are shorter by ∼2.0 Myr for the worst of the cases in the bottom left panel for SEG case. The expansion after gas expulsion is much less for these massive clusters and the effect of the WARPFIELD expanding clouds is not very appreciable. If the initial n_0 is making a difference as it does for M5 cases, it is not notorious. It may be necessary higher n_0, but for those densities, the ϵ_{SF} necessary to get an expanding cloud is larger than 0.10.

For these cases, a comparison instead of using $R_f = 0.8$ which is cut off before 14 Myr, is $R_f = 0.7$. For clusters under the influence of WARPFIELD clouds, the final average $R_f = 0.7$ value is 8.86 ± 0.30 pc and $R_f = 0.5$ is 3.92 ± 0.04.The final average $R_f = 0.5$ value for gas-free clusters is 3.69 ± 0.15 pc, i.e., an internal expansion of ∼2.8 times. The final average $R_f = 0.7$ value for gas-free clusters is 7.63 ± 0.62 pc. The expansions for all the embedded star clusters are slightly bigger in comparison with the gas-free clusters, which reflects a small effect of WARPFIELD gas expulsion. None of the R_f values get close to the shell clouds. The expansion due to stellar evolution is observable at ~ 3.5 Myr when the SNe start. A summary of the final $R_f = 0.5$ and $R_f = 0.7$ values is shown in Tab. 3.5.1.

By comparison, NOSEG sample (empty symbols) expands slightly less having or no gas, showing differences internally of less than 1 pc and outside less than 2 pc. The expansion effect by stellar evolution is not as strong as the SEG sample.

3.5.3 M7 cloud expansion

Figure 3.5.3 shows in left panels the R_f evolution for clusters with SEG (filled circles) and NOSEG (empty circles) initial stellar distributions under the influence of a WARPFIELD M7 cloud. We find that only a $\epsilon_{SF} = 0.08$ and $n_0 = 1000$ cm^{-3} can produce an expanding

cloud.In the right panel is shown the R_f time evolution for gas-free clusters starting in equilibrium and embedded star clusters suffering violent gas expulsion which are expanding and dissolving very fast in a time shorter than 6 Myr. For this case, the stellar mass is $M_{\rm cluster} = 800000$ $M_\odot$, a very massive cluster that coupled with the WARPFIELD cloud, produces an object whose gravitational potential is totally cluster dominated. The number of massive stars is bigger than the previous clouds, in consequence, even $R_f = 0.7$ is cut off before reaching 14 Myr because of SNe mass loss. For this reason, we analyze the final value of $R_f = 0.6$ for a better appreciation. The behaviour in the left and right panels are extremely similar. For clusters with WARPFIELD gas expulsion, $R_f = 0.5$ is 6.47$\pm$0.13 pc and $R_f = 0.6$ is 11.32 $\pm$ 0.45 pc. For gas-free clusters $R_f = 0.5$ is 6.44 $\pm$ 0.13 pc and $R_f = 0.6$ is 11.26 $\pm$ 0.48 pc. The values for clusters with gas are roughly the same, showing differences lower than 0.1 pc. We observe, as for M6 clouds, that the embedded star clusters do not expand after gas expulsion and they only start to expand when stellar evolution begins. The global expansion, in this case, is bigger than M6 simulations. The larger number of massive stars at the moment to evolve as SNe is taking with them larger quantities of the gravitational potential.

Final R_f values for SEG and NOSEG clusters are again very similar with differences lower than $\sim$3 pc. NOSEG simulations, as in M6 cases, expansion is only observable when the SNe start and it is again slightly weaker than the SEG sample.

3.5.4 M5 cloud (re)-collapse

Figure 3.5.4 shows the results for M5-COL clouds with SEG initial stellar distributions. The Left and central panels in each row have the same ϵ_{SF} but different initial cloud density n_0. We add two additional plots in the right column where we compare the difference between SEG and NOSEG simulations by calculation of the ratio as $R_f = 0.5$(SEG)/$R_f = 0.5$(NOSEG) where a value close to one (dashed black line) means similar $R_f = 0.5$.

The natural behaviour of a denser cloud hosting a cluster with the same mass is observed when left and central panels are compared. The (re)-collapses are earlier in central panels (black dashed line), as the denser clouds offer more resistance to the same quantity of feedback produced by the same clusters. In comparison with the EXP sample, we keep the same densities for the clouds but the clusters are reduced in mass, which produces that the gravitational potentials of the clusters are weaker than before. The clouds have a larger fraction of the gravitational potential, and the initial cluster expansion is higher. The expansions for 1GEN (solid lines, filled symbols) are reversed when the (re)-collapses occur and this is not observed instantaneously as the stars need time to travel back to the centre. The (re)-collapse does not contract the entire cluster as it is observed for the outer layers which are less affected than the internal ones. The (re)-collapses occur at different times depending on the initial conditions, so we divide them in early (central panels) and late (left panels). In left panels, as the (re)-collapses are later, the clusters have more time to expand and the outer layers are even less affected by the (re)-collapses ($R_f \geq 0.5$). Their pairs in the central panels have less time to expand, and the outer layers are closer to the centre and they are pulled inside because of the high density of the cloud towards the centre. Just after the star

Table 3.5.1: Summary of final R_f values. The first column indicates $M_{\rm cloud}$, the second column describes the initial stellar distribution and if the clusters are embedded in gas (Yes) or gas-free clusters (No). The third column indicates the initial cloud density (n_0) for clusters with gas. Final $R_f = 0.5$ is in the fourth column and the outer R_f which is still reachable at 14 Myr is in the fifth column. The outer R_f for M5, M6 and M7 are respectively $R_f = 0.8$, $R_f = 0.7$ and $R_f = 0.6$.

$M_{\rm cloud}$	Segregation / Embedded	n_0 (cm^{-3})	$R_f = 0.5$ (pc)	outer R_f (pc)
M5	SEG/Yes	$\leq$6000	19.31$\pm$ 6.67	42.65$\pm$11.02
M5	SEG/No		3.14$\pm$ 0.46	9.14$\pm$ 0.77
M5	SEG/Yes	$\geq$7000	35.21$\pm$ 2.18	60.15$\pm$ 9.17
M5	SEG/No		2.93$\pm$ 0.10	9.63$\pm$ 0.73
M5	NOSEG/Yes	$\leq$6000	16.81$\pm$ 7.37	46.26$\pm$ 11.09
M5	NOSEG/No		2.48$\pm$ 0.20	7.92$\pm$ 0.71
M5	NOSEG/Yes	$\geq$7000	35.26$\pm$ 3.52	55.50$\pm$ 15.72
M5	NOSEG/No		2.45$\pm$ 0.04	8.00$\pm$ 0.16
M6	SEG/Yes	$\leq$4000	3.92$\pm$ 0.04	8.86$\pm$ 0.30
M6	SEG/No		3.69$\pm$ 0.15	7.63$\pm$ 0.62
M6	NOSEG/Yes	$\leq$4000	3.00$\pm$ 0.10	6.80$\pm$ 0.35
M6	NOSEG/No		2.86$\pm$ 0.13	6.36$\pm$ 0.47
M7	SEG/Yes	1000	6.47$\pm$ 0.12	11.32$\pm$ 0.45
M7	SEG/No		6.44$\pm$ 0.13	11.26$\pm$ 0.48
M7	NOSEG/Yes	1000	4.18$\pm$ 0.01	8.50$\pm$ 0.50
M7	NOSEG/No		4.33$\pm$ 0.01	9.06$\pm$ 0.60

birth, the cloud expansion produces that 2GEN (dashed lines, empty symbols) looks more expanded than 1GEN but the expansion is still faster for 1GEN which finish more extended than 2GEN for every R_f. For SEG-Late cases, 1GEN $R_f = 0.5$ reaches on average 31.58 $\pm$ 3.65 pc and 2GEN on average 29.76 $\pm$ 5.62 pc. In comparison with SEG-Early, these cases expand more, 1GEN $R_f = 0.5$ reaches on average 42.27 $\pm$ 7.2 pc and 2GEN 35.23 $\pm$ 6.20 pc. For early and late (re)-collapses, 2GEN is more concentrated at 20 Myr with smaller differences for early (re)-collapses. For 1GEN, a few cases when $\epsilon_{SF} \leq 0.03$, $R_f = 0.8$ can be larger than the cloud shell during the second expansion. The 2GEN is remaining, in every case, inside of the cloud shell, with a 2GEN more concentrated than 1GEN at the end of the simulation.

The behaviour for the NOSEG sample is very similar to simulations with SEG stellar distribution, as we observe in right panels values very close to one. We only observe a few cases where after (re)-collapse 1GEN for NOSEG simulations is more concentrated than NOSEG but this distribution is erased and returns to be close to one until the end of the simulation. The specific final $R_f = 0.5$ values are shown in Tab. 3.5.2 fourth column where we observe differences smaller than $\sim$2 pc.

3.5.5 M6 cloud (re)-collapse

Figure 3.5.5 shows the results for M6 (re)-collapsing clouds with SEG initial stellar distributions. We also add the ratio plot for SEG and NOSEG simulations but this time below every respective case. We study their behaviour as a whole independent of their initial n_0. We recognize, as in expansion simulations for 1GEN (solid lines, filled symbols) that their expansions are starting only because of stellar evolution. Again, gas expulsion is not making a recognizable effect as we observe in M5 simulations. At the moment of the (re)-collapses, 1GEN is not very affected, showing weak compression. We observe after the (re)-collapse (black dashed line), a very fast expansion of 1GEN in comparison with their behaviour in the M5 sample, which is more appreciable for $R_f > 0.3$. For 2GEN (dashed lines, empty symbols), we observe an initial faster expansion that slows down quickly. $R_f = 0.7$ shows one oscillation, but it continues its expansion at the time when SNe starts. On average, 1GEN is more strongly affected by the second expansion, but it is not the case for 2GEN. We do not observe a correlation of final expansion as we increase the initial cloud density. The clouds evolve differently and (re)-collapses are not occurring at the same time and a direct comparison is not possible.

Comparing with the NOSEG sample in the smaller sub-panels under every SEG case, we observe differences larger than the M5 sample but still close to one. Only for the case in the right bottom panel, we measure a large difference for 1GEN-NOSEG which finishes 3 times more concentrated than 1GEN-SEG. The other cases also show this final distribution but with values closer to one. On the other hand, 2GEN-SEG can finish even 2 times more concentrated than 2GEN-NOSEG for the most notorious case in the left bottom panel. The rest of the expansions are more similar as we measure ratios slightly below or above one.

For the SEG sample, 1GEN $R_f = 0.5$ at 20 Myr expands on average until 87.66 $\pm$ 22.9 pc and 2GEN 8.56 $\pm$ 1.81 pc. For the NOSEG sample, 1GEN $R_f = 0.5$ at 20 Myr expands on

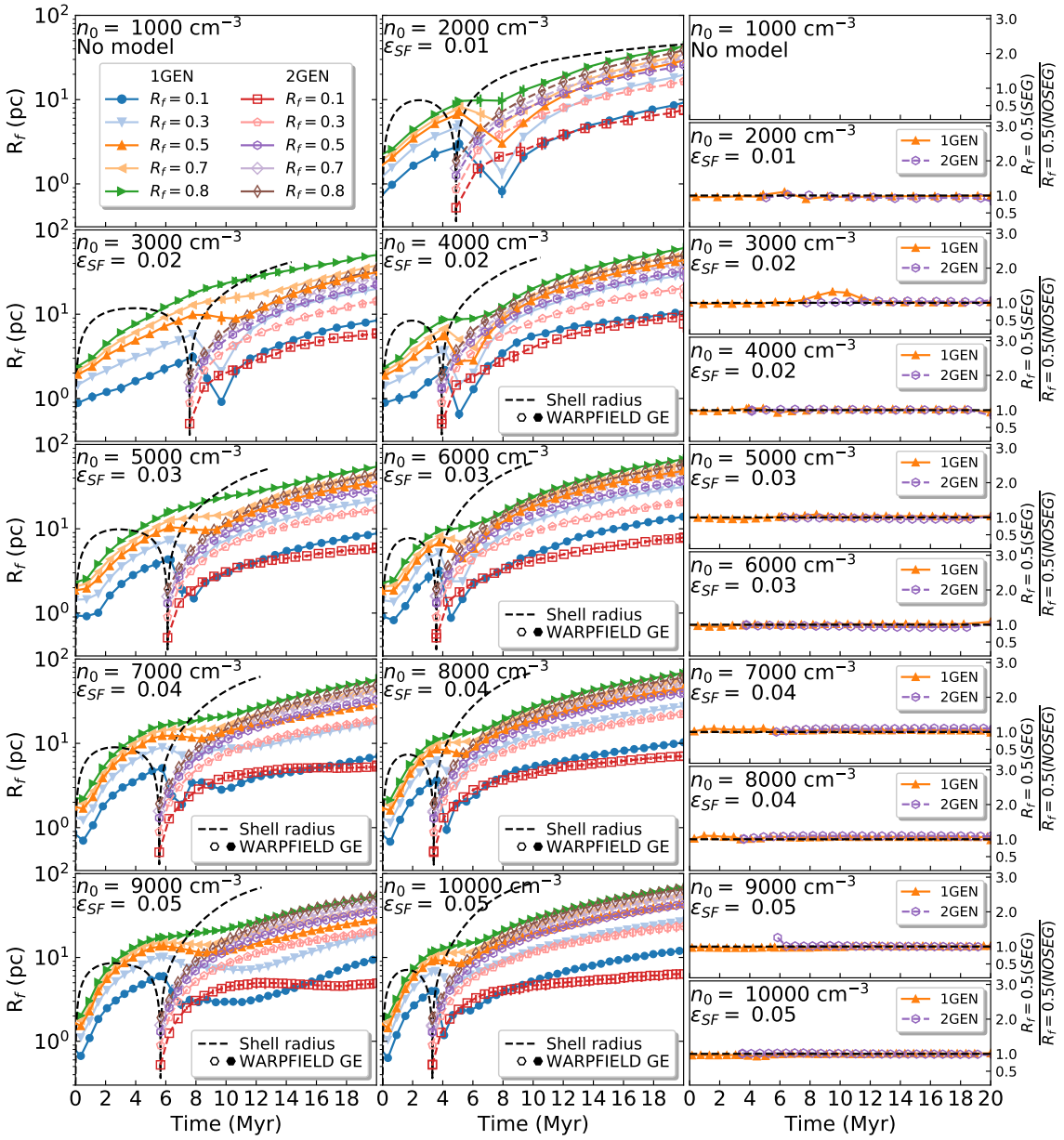

Figure 3.5.4: Left and central panels show the average Lagrangian radii of a series of clusters which have SEG initial stellar distribution under the influence of clouds that (re)-collapse with an initial mass of $M = 10^5$ M$_\odot$. The dashed black line indicates the shell radius for each of the clouds. The colour lines indicates R$_f$ 0.1, 0.3, 0.5, 0.7 and 0.8 from bottom to top. Solid lines with filled symbols are for first generation stars (1GEN) and dashed lines with open symbols for second generation stars (2GEN). Right panels compare the ratio between R$_f = 0.5$ for simulations starting with mass segregation (SEG) or not (NOSEG) as R$_f = 0.5$(SEG)/R$_f = 0.5$(NOSEG). The dashed black line in the right panels indicates a ratio equal to 1. The respective ϵ_{SF} and clouds initial density (n_0) are indicated in each panel.

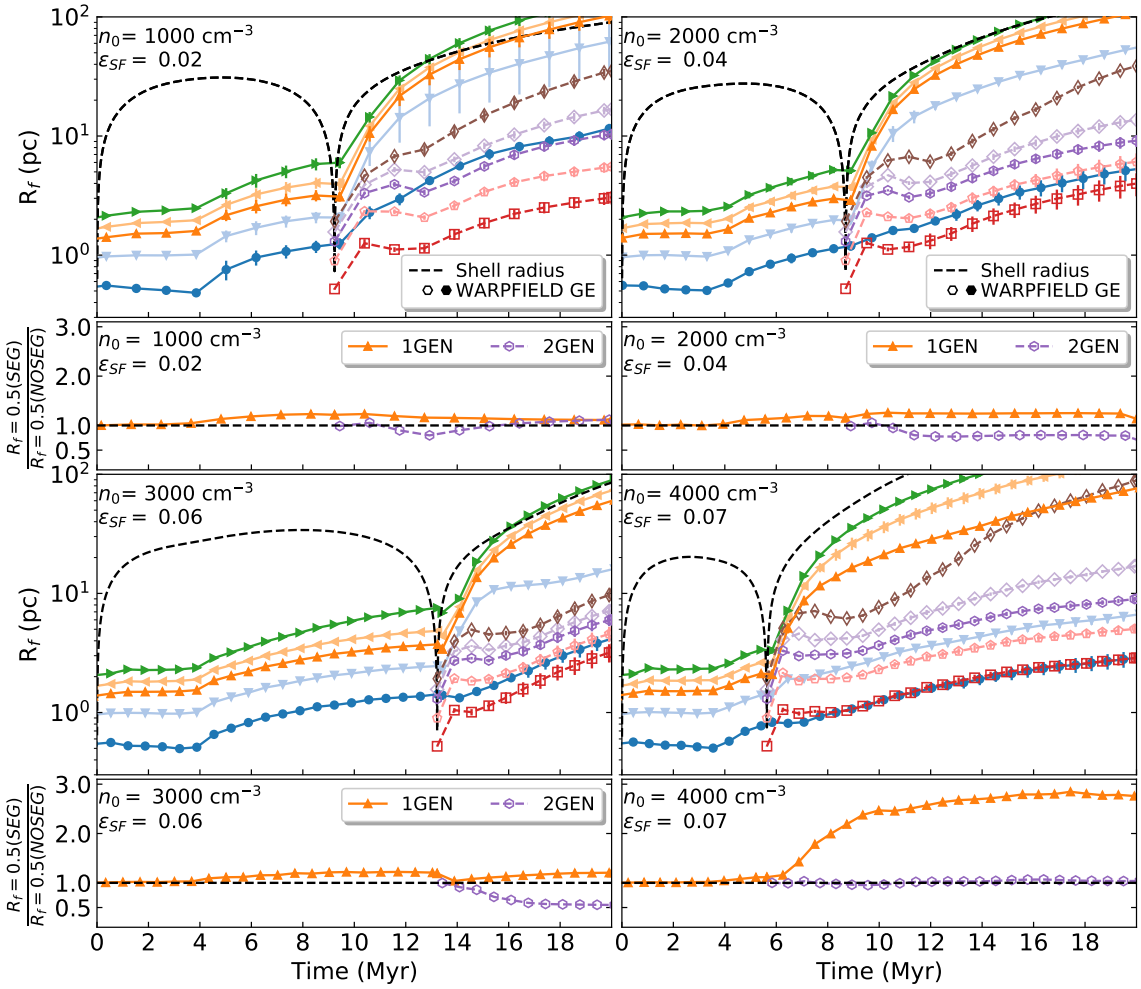

Figure 3.5.5: Colours and symbols are the same as in Fig. 3.5.4 but now for M6 sample. Ratio between $R_f = 0.5$ is now indicated bellow the respective case.

average until 65.21 $\pm$ 31.19 pc and 2GEN 10.07 $\pm$ 1.40 pc. The larger difference is observed for 1GEN where the case previously described is increasing the average final $R_f = 0.5$. For 2GEN, similar results are found and a difference of $\sim$ 2 pc is observed. We summarize these quantities in Tab. 3.5.2.

3.5.6 M7 cloud (re)-collapse

Figure 3.5.6 shows the results for M7 (re)-collapsing clouds with SEG initial stellar distributions. The ratio between SEG and NOSEG samples is added below the main panel. Initial gas expulsion is practically ignored as we observe in expansion simulations of M7 clouds. The expansions for 1GEN (solid lines, filled symbols) only start due to stellar evolution producing that $R_f = 0.7$ and 0.8 are cut off due to SNe mass loss before the (re)-collapse (black dashed

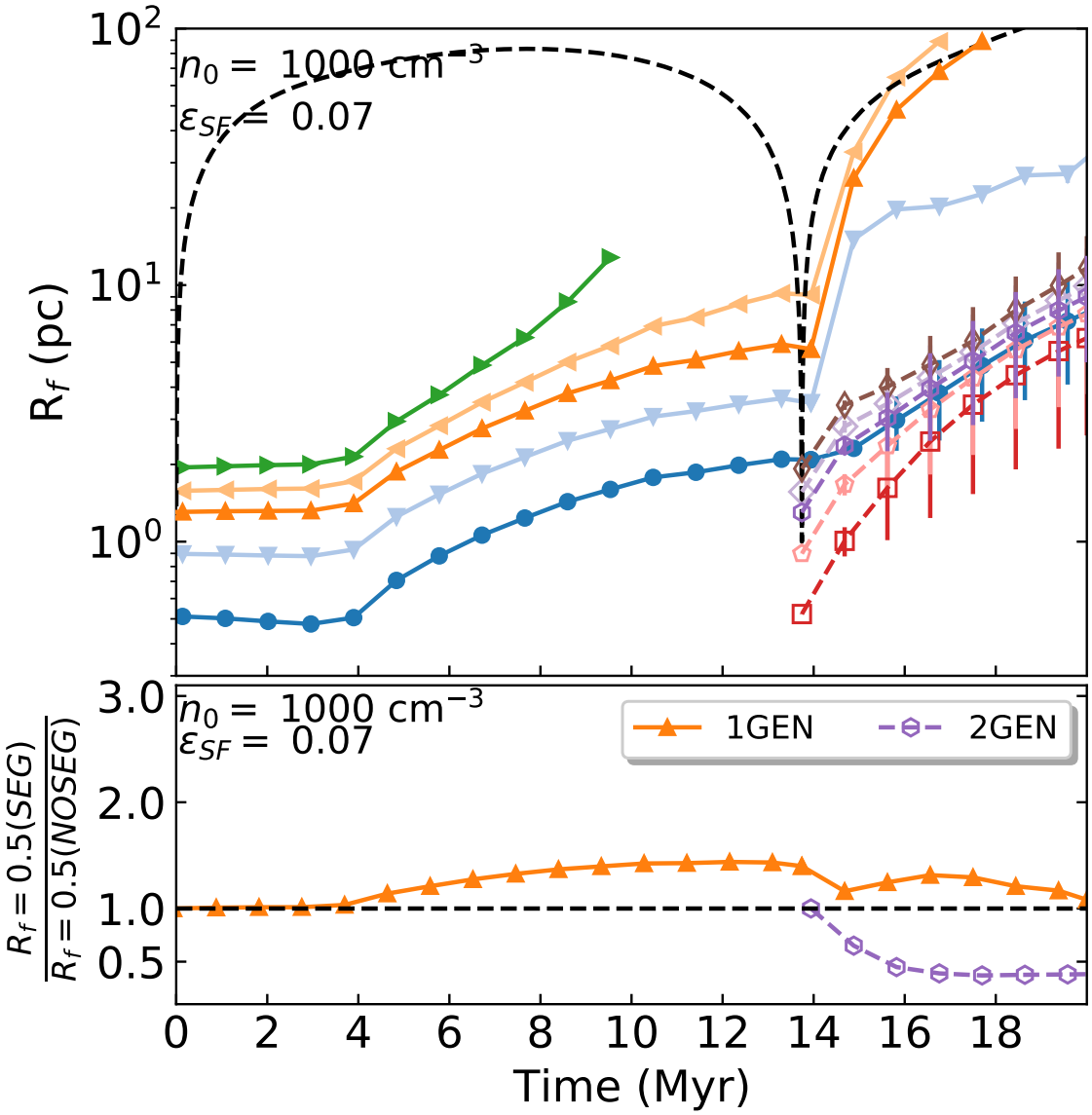

Figure 3.5.6: Colours, symbols and order are the same as in Fig. 3.5.5 but now for the M7 sample.

$M_{\rm cloud}$	Segregation	1GEN $R_f = 0.5$ (pc)	2GEN $R_f = 0.5$ (pc)
M5	SEG-Late	31.58 ± 3.65	29.76 ± 5.62
M5	SEG-Early	42.27 ± 7.22	35.23 ± 6.20
M5	NOSEG-Late	30.83 ± 3.61	28.93 ± 5.79
M5	NOSEG-Early	40.59 ± 6.41	34.54 ± 5.82
M6	SEG	87.66 ± 22.90	8.56 ± 1.81
M6	NOSEG	65.21 ± 31.19	10.07 ± 1.40
M7	SEG	131.11 ± 7.93	9.00 ± 4.00
M7	NOSEG	121.15 ± 5.85	23.48 ± 4.86

Table 3.5.2: Summary of final $R_f = 0.5$ values by generation. The first column indicates the initial mass cloud, the second column shows the initial stellar distribution and for M5 cases if they are under early or late (re)-collapse. The third and fourth columns indicate the average $R_f = 0.5$ at 20 Myr for 1GEN and 2GEN respectively.

line). At the moment of the (re)-collapse, 1GEN does not show strong shrink. After the star birth, much faster expansions for all R_f are observed. 2GEN (dashed lines, empty symbols) continuously expand since the first moment but less than 1GEN. 1GEN-NOSEG behaves initially very similar but start to differ becoming more concentrated than their 1GEN-SEG pairs. At the end of the simulation, we observe a value closer to one. 2GEN-NOSEG expand even more than 2 times compared with 2GEN-SEG.

The SEG-1GEN $R_f = 0.5$ at 20 Myr, shows large values, expanding on average until 131.11 ± 7.93 pc and SEG-2GEN 9.00 ± 4.00 pc. The NOSEG-1GEN $R_f = 0.5$ at 20 Myr, shows large values, expanding on average until 121.11 ± 5.85 pc and NOSEG-2GEN 23.48 ± 4.86 pc. We summarize these values in Tab. 3.5.2.

3.6 Potential Caveat

Our simulations, in terms of the WARPFIELD modelling, consider a wide range of mass-loss processes for massive stars including Wolf-Rayet winds and supernovae, eventually leading to remnant neutron stars ($M \sim 1.5$ $M_\odot$) or black holes (Ekström et al. 2012). We note, that the stellar evolution libraries in NBODY6++GPU differ from those in WARPFIELD. For example, WARPFIELD approximates the SNe remnants as an object with no feedback i.e., after a star explodes as SN, the quantity of energy injected from the remnant is null. In NBODY6++GPU we can mimic this process by decreasing the mass of the specific star when it reaches the SNe event according to Ekström et al. (2012). The alternative would be to replace the entire stellar evolution routines of the N-body integrator, which is beyond the scope of this study. We explore the impact of our approximation in Fig. 3.6.1, where we use the complete stellar evolution model included in NBODY6++GPU for a subset of models. We take one of the simulations for each of the cases without gas, where the cluster expansion is only triggered by stellar evolution as they start in equilibrium. We observe that until $R_f \leq 0.7$ both cases finish with similar expansion even when the experiment simulations start to expand earlier

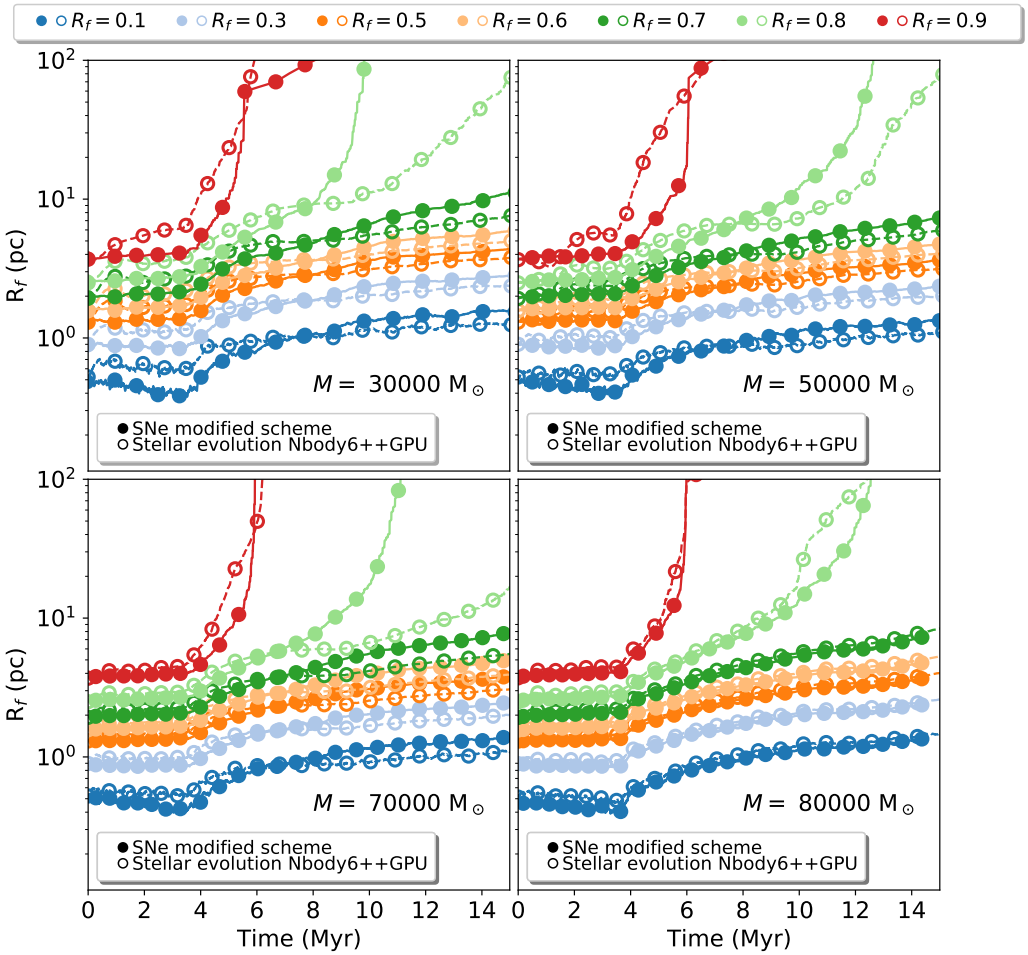

Figure 3.6.1: Example R_f evolutions for simulations using the SNe modified scheme of this chapter (filled circles) and NBODY6++GPU stellar evolution (empty circles).

as the winds are acting from the beginning. Larger differences are observed only for the R_f 0.8 and 0.9, which become unbound during the dynamical evolution. We remind the reader that our analysis in this chapter is largely based on the analysis of $R_f = 0.5$ which behaves similarly for every case.

3.7 Summary and discussion

We study the evolution of embedded start clusters with low star formation efficiency ($\epsilon_{SF} \lesssim 0.10$), which are either initially mass segregated and not. We follow the stellar component evolution by mean of N-body simulations and the gas by the 1D stellar feedback model WARPFIELD.

3.7.1 Local of massive stars

As the WARPFIELD gas modelling expansion does not take into account the behaviour of the stellar component, we first test if massive stars, which produce most of the feedback energy and momentum, remain in locations close to the cluster centre or at least inside of the swept-up dense shell expanding into the surrounding ISM. This is a central assumption for the description of the gas dynamical evolution in WARPFIELD.

We develop this study locating N-body simulations in the centre of the clouds with different initial conditions. We find that the average distances (weighted by luminosity) from the centre of the most massive stars ($M > 20$ M$_\odot$) are always lower than the shell radius calculated by WARPFIELD. The initial stellar distributions expand due to gas expulsion or stellar evolution but never enough to leave the clouds. This behaviour gives support to the radial expansion of the clouds including all feedback coming from most massive stars, and it is better observed for M6 and M7 clouds. For the expansion sample, the previous behaviour is valid for the whole simulation time. On the other hand, for the (re)-collapse sample, the most massive stars can be found outside of the shell radius when the (re)-collapsing phase is about to be reached, but only for M5 clouds. For M6 and M7 clouds, the massive stars are always inside of the shell.

3.7.2 Survival of clusters which continuously expand their clouds: classical picture.

We follow the Lagrangian radii evolution along the cluster evolution. For the expansion sample, we compare the expanding clusters using our WARPFIELD & N-body models with the same clusters without any gas influence and with embedded star clusters following the classical violent gas expulsion i.e. the gas also follow a Plummer profile being denser than the uniform density we used inside WARPFIELD. We observe that M5 simulations are affected by the gas expulsion and it is more notorious when n_0 is increased. The expansions observed for these clusters are less than the expansions produced by embedded star clusters whit the same ϵ_{SF} following the classical picture gas expulsion which is very destructive and the clusters get dissolved. The uniform gas distributions we used within WARPFIELD molecular clouds do not produce the same quantity of gravitational potential and the clusters can react better to the weaker change of the internal energy. The clusters with M5 clouds expand when the gas is expelled, as is expected, more than the gas-free cluster and much less than the clusters with the classical gas expulsion, which make them survive longer. If the initial stellar distribution is influencing on the global evolution for the expansion sample, it can be answered by comparing clusters initially segregated and non expand practically in the same

range with differences less than 5 pc. Simulations for M6 and M7 show very small differences compared to non-gas clusters, and this is because of the low density clouds. The gravitational potential produced by a M5, M6 or M7 uniform cloud with 10000 cm^{-3}, at a specific central distance inside the cloud is the same. The only difference between the clouds is their size, which is larger when the cloud is more massive. On the other hand, we use Plummer profiles for the stars with a scale length always of 1 pc. The clusters only increase in mass and not in radius, which produce stronger gravitational potentials. The clusters embedded in M6 or M7 clouds are dominating the gravitational potential, resulting in clusters not responding or practically ignoring the gas expulsion and evolving in the same way as their gas-free clusters pairs and therefore they survive.

3.7.3 Survival of clusters with clouds that (re)-collapse.

For the (re)-collapse sample, we reduce the ϵ_{SF} in 0.01, whereby the clusters do not produce enough feedback to keep the clouds in expansion and eventually (re)-collapse producing a second star birth. As before, we follow the evolution of the Lagrangian radii for our WARPFIELD & N-body models but for these cases separated by generation to have a better appreciation of the internal dynamics. We do not show any comparison model since in the classical pictures feedback is always assumed to be sufficient to take the cloud apart. The embedded star clusters before reaching the (re)-collapse phase evolve as the expansion sample. The (re)-collapses are not producing a shrink of the stellar component but this is not instantaneous. For clusters with M5 clouds, the first stellar generations are reduced in size after the clouds start to expand again. For cases with early (re)-collapses in the M5 sample, the clusters have little time to expand. The (re)-collapses have a large effect causing stars to travel closer to the gravitational centre, almost as compact as the new stellar generation's initial distribution. On the other hand, for late (re)-collapses, the clusters are also suffering contraction, but they restart the expansion from a larger central distance and in consequence, they do not get as deep as the simulations with early (re)-collapses. The following expansion is very destructive for the old generation, independent of the early or late (re)-collapse, as the change in the potential is much bigger than the initial. Every embedded star cluster starts in equilibrium, but just before the second generation birth, the clouds get very dense and concentrated in the centre dominating the gravitational potential. The following gas expansion carries out a large part of the gravitational potential, which consequently strongly expands the old stellar component. The new stellar component is added to the simulation and their velocities are scaled to achieve initial virial equilibrium. In this case, the expansion of the cloud does not cause the clusters to expand as much as the old component, but the last is continuously removing part of the gravitational potential which affects the new cluster. The level of expansion for the second stellar component is less than the old but larger than the gas-free clusters sample. The smallest differences in $R_f = 0.5$ are observed for the M5 sample. The final values differ in average but overlapping 1 sigma error independent if it is early or late gas expulsion or SEG or NOSEG initial stellar distribution.

Larger differences are observed for the M6 sample, where the different stellar components are better distinguished. For this case, simulations with different initial stellar dis-

tributions show different averages, but they also overlap in error-bars. The same trend is followed by the old stars for the M7 sample, but in this case, the younger stellar component for the non-segregated case is more extended. A second starburst with the same ϵ_{SF} is not increasing the survivability of the clusters, as this scenario is more destructive for both stellar generations. The differences for the final R_f increase as the clouds are more massive.

At 20 Myr, we observe that for independent of the initial conditions, the younger clusters are always more concentrated than the older, better recognizable for M6 and M7. This has been observed, e.g., in 30 Doradus where the cluster NG2070 is hosting a younger massive sub-cluster in its central zone. Beccari et al. (2017) found three stellar populations, each from the youngest to the oldest, more concentrated than the previous older one. Whether this scenario is a natural result of the dynamics, is a matter of discussion as it has been also observed multiple populations without preferable locations (see e.g.. De Marchi et al. 2011). We only explore the inclusion of a new stellar generation using the same ϵ_{SF}. The results can change modifying this value due to the domination of the gravitational potential. A more massive new stellar generation can improve its future behaviour if it is massive enough to resist the cloud and old star generation expansion. In the same way, a lower mass cluster feels the change of the gravitational potential and in consequence expands more. A smaller or greater value of the initial virial state could improve or decrease respectively its chances of survival but this has not been studied here.

3.8 Conclusions

We conclude that low ϵ_{SF} embedded star clusters, with sufficient wind and radiative feedback (described by WARPFIELD), which drive gas expulsion in fact survive. This challenges the classical picture where embedded star clusters with $\epsilon_{SF} < 0.10$ should not survive due to the strong change in the gravitational potential when the gas is expelled. In the case of massive clouds (M6 and M7), this result is not sensitive to the initial conditions, but on the slow non-instantaneous expulsion of gas due to gravity slowing the expansion driven by winds and stellar radiation pressure.

On the other hand, the low ϵ_{SF} embedded clusters which are not able to produce enough feedback to unbind their parent gas and (re)-collapse (thus giving birth to a second generation of stars), show different behaviour. For M6 and M7 clouds, the older generation of stars is strongly affected by the gravitational potential change after the birth of the new stellar component. The new star cluster, imposed to start in virial equilibrium, adapts better to the posterior gas expulsion thus surviving. For M5 clouds, the second expansion of the gas affects the old component less, producing an expansion at the same level as the new stellar component. Since both stellar components for the M5 clouds have similar expansions, an age mass segregation is not visible. For more massive embedded star clusters (M6 and M7), we find that the age mass segregation is a natural output from the initial conditions used in this study.

For both scenarios, we find a weak dependency on mass segregation. The expansions between clusters with or without this imposed condition do not show big differences. Nev-

ertheless, a few exceptions are found. We can not neglect that its effect can be observable in an extended parameter space.

By incorporating a more realistic stellar evolution path, we find that more massive clusters expand from the beginning and then more slowly after SNe events. This is produced by the less violent kick to neighbouring stars as the remnants is more massive which would lead to increased survival. In this context, we conclude that our results can provide an upper limit to the expansion radius of an embedded star cluster.

We find that radial feedback modelling of WARPFIELD is well suited to study cloud evolution. The most massive stars, which are the culprit to generate most of the feedback injected into the cloud, remain within the shell radius for the duration of their life. For M5 clouds this behaviour is very close to the limit, but we show that for M6 and M7 clouds the stars behave very smooth and they remain all the time captive inside the cloud shell even for a (re)-collapsing cloud. The results could change if the initial cloud density increases, but this yield also in a more massive cluster and the $\epsilon_{SF} > 0.10$ which is out of our aim. The results can also be affected including initial binaries, which add more gravitational potential and higher kinetic energy exchange which can result in stars escaping (Heggie 1975; Hills 1975). However, at least for low mass star clusters, a high fraction of binaries is required to observe large changes in cluster expansion (Farias et al. 2017).

4

30 Doradus, the double stellar birth scenario by NBODY6 & WARPFIELD

In this chapter, we study the evolution of embedded star clusters as possible progenitors to reproduce 30 Doradus, specifically the compact star cluster known as R136 and its surrounding stellar family, which is believed to be part of an earlier star formation event. We employ the high-precision stellar dynamics code NBODY6++GPU to calculate the dynamics of the stars embedded in different evolving molecular clouds modelled by the 1D cloud/clusters evolution code WARPFIELD. We explore clouds with initial masses of $M_{\rm cloud} = 3.16 \times 10^5$ M$_\odot$ that (re)-collapse allowing for the birth of a second generation of stars. We explore different star formation efficiencies in order to find the best set of parameters that can reproduce the observation measurements. Our best-fit models correspond to a first stellar generation with masses between $1.26 \times\ 10^4$ - $2.85 \times\ 10^4$ M$_\odot$ and for the second generation we find a $M \approx 6.32 \times 10^4$ M$_\odot$. Our models can match the observed stellar ages, cloud shell radius, and the fact that the second generation of stars is more concentrated than the first one. This is found independently of the cluster starting initially with mass segregation or not. By comparing our results with recent observational measurements of the mass segregation and density profile of the central zone we find close agreement, and thus provide supporting evidence for a centrally focused (re)-collapse origin to the multiple ages.

4.1 Motivation

30 Doradus, located in the Large Magellanic Cloud (LMC), is a massive star forming region. In its center, the cluster NGC 2070 hosts a younger massive subcluster, R136. It appears that the the feedback from the older stellar population in NGC 2070 was not strong enough

to take apart its parental molecular cloud. Consequently, the parent molecular cloud could retain or re-accrete part of its mass, and form R136 as a massive second generation cluster. The latter scenario has been supported by different studies. For instance, Silich and Tenorio-Tagle (2017) showed that under dense conditions ($n \gtrsim 10^5$ cm^{-3} in a cloud of 10^6 M$_\odot$), the feedback produced by stellar winds may not be as strong enough to disperse the cloud. There are other massive young clusters which show evidence for multiple generations of stars, e.g. Sandage-96 exhibits a bimodal age separation of at least 10 Myr (Palla et al. 2005, 2007; Vinkó et al. 2009) while the Orion nebula cluster has an even smaller age spread of less than 1 Myr (Beccari et al. 2017). The best evidence for multiple stellar generations in compact star clusters comes from the observations of globular clusters (see e.g.. Carretta et al. 2009). These could be a result of the (re)-collapse of gas ejecta from older generation of asymptotic giant branch stars (D'Ercole et al. 2008), fast-rotating massive stars (Decressin et al. 2007) or interactive massive binaries (de Mink et al. 2009). However, these scenarios typically predict the second generation of stars to be much less massive than the older generation, specifically for a small age difference. Hence, they are not applicable to 30 Doradus where the new stellar population at current time appears to be more massive than the old extended star cluster.

In Chapter 3, we have developed a framework by combining WARPFIELD and NBODY6++GPU which allows us to study the evolution of embedded star clusters with more than one star formation event as it is observed in 30 Doradus. Using this framework, in this chapter, we aim to find combinations of initial conditions which can lead to an object similar to NGC 2070 and its centrally concentrated younger sub-star cluster R136.

4.2 Method and Initial Conditions

4.2.1 Properties of 30 Doradus

The main cluster in the 30 Doradus region, NGC 2070, contains two stellar generations. The older population has an age of $\sim$ 3-7 Myr (Brandl et al. 1996; Walborn and Blades 1997; Selman et al. 1999; Sabbi et al. 2012; Cignoni et al. 2015) and the younger population $\sim$ 0.5-2 Myr which also appears to be more concentrated towards the centre (Massey and Hunter 1998b; Selman et al. 1999; Sabbi et al. 2012; Cignoni et al. 2015; Bestenlehner et al. 2020; Brands et al. 2022) called R136 or formally known as RMC 136. The masses of the clusters are poorly constrained. R136 has a range of mass between 2.2$\times$10^4-1$\times$10^5 M$_\odot$ (Hunter et al. 1995; Andersen et al. 2009; Cignoni et al. 2015) and the whole cluster NGC 2070 6.8$\times$10^4-5$\times$10^5 M$_\odot$ (Selman et al. 1999; Bosch et al. 2001, 2009; Cignoni et al. 2015). In this zone is observed ionized gas which forms bubbles containing hot, X-ray emitting gas (Townsley et al. 2006). Pellegrini et al. (2011b) using [SII]/Hα observations showed that the H II region around NGC 2070 has the shape of a hemispherical bowl. The whole sphere has a radius of 40 - 60 pc and R136 has an offset approximately 12 pc from its centre. The shell radius surrounding R136 as the centre is $\sim$ 30 - 70 pc. We summarize these values in Tab. 4.2.1.

4.2.2 Modeling approach

Our goal is to find the cloud-cluster parameter space capable of reproducing the properties of 30 Doradus sensitive to cluster evolution. To address this problem, we study a range of molecular clouds and cluster masses, resulting in different ϵ_{SF}. The evolution of the clouds is followed using the code WARPFIELD 2.1 (Rahner et al. 2017). As the clouds expand, the gravitational potential is changing, which is introduced into the N-body calculation of the stellar dynamics as a time-evolving external potential. The dynamics of the star clusters is followed using the code NBODY6++GPU (Wang et al. 2015) modified for our purpose in order to read in information from the WARPFIELD code. We note that WARPFIELD calculates the overall feedback produced by a star cluster located in the centre of the cloud. The energy injected from the stars to the cloud produces its expansion, resulting in one of the following outcomes:

(i) The cluster injects enough feedback dispersing the cloud.

(ii) The cluster does not inject enough feedback and after an initial period of expansion, gravity overtakes and the cloud collapse again and gives birth to a new stellar generation.

(iii) The subsequent evolution can follow (i) or (ii), which means the process could be repeated multiple times leading to the formation of multiple stellar populations until the cloud is finally dispersed.

Using WARPFIELD, we create clouds with masses of 3.16×10^5 $M_\odot$ following uniform profiles which host star clusters of different masses. From the observational data, the R136 appears to be more massive than the old cluster. We fix the new cluster to have a value of $\epsilon_{SF} = 0.20$ and we try for older stellar component ϵ_{SF} between 0.01 and 0.10. To emulate our star clusters, we follow Plummer density profiles with $R_{\rm pl} = 1$ pc and the stellar mass is changed to achieve the ϵ_{SF} required. We randomly create 10 different Plummer distributions using MCLUSTER (Küpper et al. 2011) following a Kroupa (2001) IMF. The masses are randomly located along the different Plummer distributions to obtain two samples. Each sample consists in 10 clusters with mass segregation and 10 non-segregated. To be consistent with WARPFIELD calculations, we are not using the stellar evolution features from NBODY6++GPU. We are evolving massive stars until they reach their maximum ages according to Ekström et al. (2012) as WARPFIELD follows. The size of the cluster is a free parameter for WARPFIELD, which determines the radial 1d feedback. We use $R_{\rm pl} = 1$ pc as is commonly assumed for young clusters in the range of mass used in this work (Pfalzner et al. 2016).

From WARPFIELD outputs, we obtain the gravitational potential evolving in time as we describe in Sec. 3.2. A value of $\alpha = 0.5$ is also used for our initial object, i.e., the first stellar component and the gas start in equilibrium but for the second generation of stars, after an exploration of different α states, we can reproduce closely the observations of R136 presented by Khorrami et al. (2021) (hereafter K2021) by using an $\alpha = 0.3$ which is the one reported in this chapter.

Table 4.2.1: Summary of observational parameters to match with our models.

Property	Value
Age first stellar generation	3-7 Myr
Age second stellar generation	0.5-2 Myr
Mass second stellar generation	2.2×10^4-1×10^5 $M_\odot$
Total mass NGC 2070	6.8×10^4-5×10^5 $M_\odot$
Shell radius	30 - 70 pc

4.2.3 Analysis

One key parameter characterizing the dynamical state of a star cluster is the level of mass segregation, which we quantify using the $\Lambda_{\rm MSR}$ parameter (see Sec. 2.2.2). We compute $\Lambda_{\rm MSR}$ for all stars in the system and for the first and second stellar generations separately.

The procedure to match with the properties of NGC 2070 followed in this work is summarized as:

(i) We let evolve an initial N-body cluster (1GEN), in equilibrium with the gas ($\alpha_{\rm 1GEN} = 0.5$). The simulation continues until the moment when WARPFIELD indicates that there is a second starburst ((re)-collapse).

(ii) We stop the simulation and we add a second N-body cluster (2GEN).

(iii) We scale the velocities of the stars for 2GEN to get $\alpha_{\rm 2GEN} = 0.3$.

(iv) We continue the simulation until reach 8 Myr, which is already 1 Myr older than the current age of NGC 2070.

We use 5 different Plummer distributions to represent the 1GEN and another 5 for the 2GEN. In this study we consider the two cases: both stellar generations either start with mass segregation or without. We compare the central distance for the massive stars and the Lagrangian radii for each generation. We also study $\Lambda_{\rm MSR}$ parameter as a function of simulation time. We are looking for simulations that evolve to match the properties in Tab. 4.2.1, and a $\Lambda_{\rm MSR} < 1$ when the massive stars of 1GEN and 2GEN are compared, i.e., the older massive stars more dispersed than the younger as NGC 2070 exhibits. For all parameters, we show the average of 5 different realizations.

4.3 Results

4.3.1 WARPFIELD clouds

We first constrain our parameter space by finding WARPFIELD clouds which can reproduce the ages of the two stellar populations and the shell radius. We explore different values of ϵ_{SF} from 0.01 until 0.10 for the first cluster and a fixed ϵ_{SF} = 0.20 for the second star cluster. These choices allow us to match the observed mass of R136. We summarize the successful WARPFIELD models in Tab. 4.2.2 where the first and second columns indicate the

Table 4.2.2: Summary of parameter space explored in this study. The first column shows the initial density of the clouds which initially have a mass of 3.16×10^5 $M_\odot$. The ϵ_{SF} for the embedded star clusters are shown in the second column and the time when the clouds (re)-collapse are shown in column third. The temporal duration over which the models match with observations is shown in column fourth. The average separation of the central distance for massive stars between generations at the moment of the match is shown in columns five and sixth for simulations with mass segregation and without, respectively.

n_0	$\epsilon_{SF\ 1}$	(re)-collapse	Δ time	D[1GEN] - D[2GEN] (pc)	
(cm^{-3})	$\epsilon_{SF\ 2}$	time (Myr)	(Myr)	SEG	NOSEG
6000	0.04-0.20	2.63	0.60	2.93 ± 0.61	3.37 ± 0.58
6000	0.05-0.20	3.35	0.70	3.28 ± 0.73	3.60 ± 0.92
7000	0.05-0.20	2.62	0.50	3.60 ± 0.39	3.61 ± 0.73
7000	0.06-0.20	3.38	0.70	2.78 ± 0.44	3.76 ± 0.64
8000	0.05-0.20	2.21	0.50	3.69 ± 0.46	3.72 ± 0.65
8000	0.06-0.20	2.62	0.50	3.09 ± 0.52	3.19 ± 0.41
8000	0.07-0.20	3.40	0.70	2.59 ± 0.46	2.48 ± 0.93
9000	0.04-0.20	1.76	0.40	3.79 ± 0.46	3.72 ± 0.62
9000	0.05-0.20	1.95	0.40	3.85 ± 0.44	3.91 ± 0.45
9000	0.06-0.20	2.22	0.50	3.13 ± 0.36	3.10 ± 0.38
9000	0.07-0.20	2.63	0.50	2.53 ± 0.63	2.73 ± 0.60
9000	0.08-0.20	3.48	0.70	1.94 ± 0.31	3.12 ± 0.70
10000	0.06-0.20	1.94	0.40	3.45 ± 0.45	3.36 ± 0.44
10000	0.07-0.20	2.22	0.40	2.98 ± 0.48	3.53 ± 0.53
10000	0.08-0.20	2.65	0.50	2.17 ± 0.59	2.95 ± 0.51
10000	0.09-0.20	3.61	0.70	1.97 ± 0.59	2.86 ± 0.71

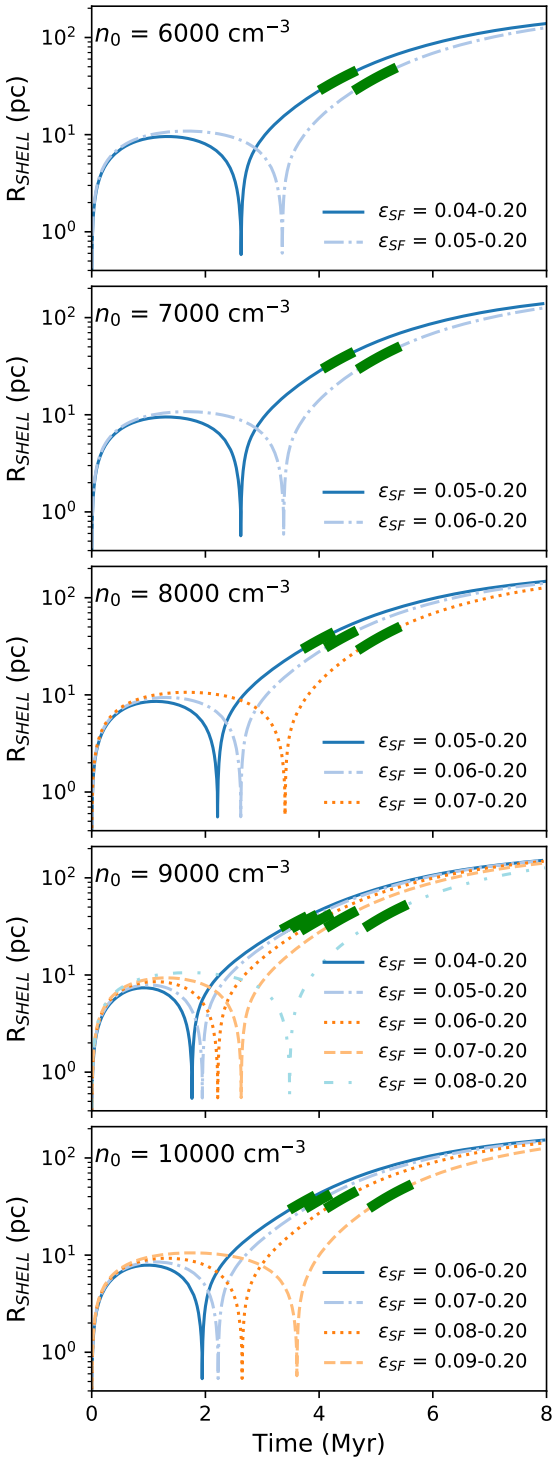

Figure 4.2.1: Shell radius evolving in time from WARPFIELD models. Different line styles represent the respective ϵ_{SF}. The ranges of time when the models match with NGC 2070 properties are highlighted by a green thick line.

initial density and the ϵ_{SF} pair, respectively. The shell radii evolution for each of the cases in our parameter space obtained from WARPFIELD simulations are shown in Fig. 4.2.1. Every panel shows a cloud with different initial density. We have for every initial density more than one ϵ_{SF} pair which are represented with different line styles. Initially, the clouds expand due to stellar feedback exerted by the central cluster. After that, depending on the initial density and the cluster mass, the shell radii reach a maximum followed by a (re)-collapse. The (re)-collapse times are shown in Tab. 4.2.2, column third. The moment of (re)-collapse increases as we use larger ϵ_{SF} for each cloud. This is expected as a more massive cluster keeps the cloud expansion for a longer time due to higher feedback. After the second starburst, the shells expand again and for all cases, the expansions continue until we stop the simulation. We highlight with a thicker green line the zone where the stellar ages and the shell radius match the properties (see Tab. 4.2.1). For all cases, the left sides of the matching zones start when the minimum shell radius is found (~ 30 pc) and the right limit when the 2GEN maximum age is reached. The temporal duration (Δ) of these zones are summarized in Tab. 4.2.2, column fourth with values between 0.4 and 0.7 Myr. Two clusters together produce a faster expansion of the shell, as a larger amount of feedback is added to the cloud. If less massive 2GEN clusters ($\epsilon_{SF} < 0.20$) are taken into account, these zones are much shorter as the shells need more time to reach the minimum size, approaching or even passing the maximum 2GEN age. The inclusion of mass segregation does not change the WARPFIELD cloud evolution, as the 1D model simply assumes all feedback is injected from the cluster centre. This is an appropriate assumption as the shell radius exceeds the cluster radius during most evolutionary phases, except at the very end of (re)-collapse when a new stellar generation is formed (see Sec. 3.3.1).

4.3.2 Massive stars

In Fig. 4.3.1, we compare the central distance evolving in time for massive stars ($M > 20\mathrm{M}_\odot$) by stellar generation. We show the central distance evolution for each of the cases weighted by its luminosity according to Gräfener et al. (2011) to achieve more specific information about the location of the most massive stars which predominate in brightness and quantity of feedback. Simulations starting with mass segregation (SEG) are shown with circles and with no mass segregation (NOSEG) are denoted by squares. The evolution for 1GEN is denoted by red filled symbols and 2GEN by blue empty symbols. The green zone is the matching zone described in Sec. 4.3.1 and the shell radius is represented by a black dashed line. We also indicate when the first SN occurs for each generation with orange and cyan dashed lines, respectively. This is $t \sim t_0 + 3.5$ Myr, where $t_0 = 0$ Myr for 1GEN and for 2EGN is the time when the cloud (re)-collapses. The clusters cover a range of masses for 1GEN of $1.30 \times 10^4\ \mathrm{M}_\odot \leq M_{\mathrm{1GEN}} \leq 2.85 \times 10^4\ \mathrm{M}_\odot$. On the low mass limit, the small number of stars is not enough to cover the whole IMF mass range and this is only complete for $\epsilon_{SF} \geq 0.06$. On the other hand, for 2GEN we have $M_{\mathrm{2GEN}} \approx 5.90 \times 10^4$, which completes the IMF sample.

For SEG simulations, we observe that 1GEN massive stars (solid line, filled red circles) reach outer positions due to cloud expansion affecting them. At the moment of the (re)-collapse, a strong gravitational potential on the centre is produced due to the high density of

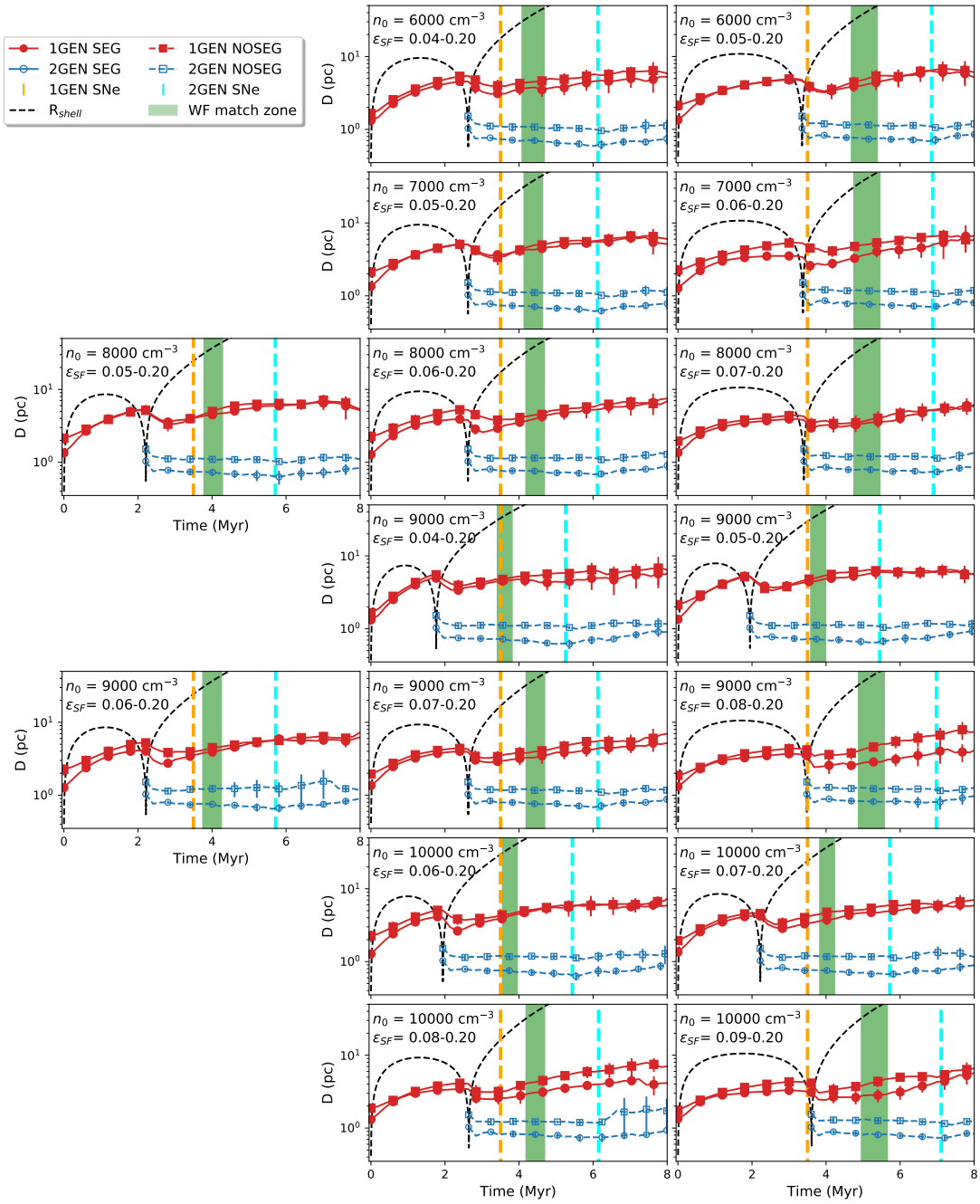

Figure 4.3.1: Central distance of massive stars ($M > 20$ M$_\odot$) vs time. The first generation (1GEN) is denoted by red filled symbols and a red solid line. The second generation (2GEN) is denoted by blue empty symbols and dashed blue lines. Simulations starting with (SEG) or without (NOSEG) mass segregation are represented by circles or squares, respectively. The Black dashed line is the shell radius. The green zone indicates where the ages of 1GEN and 2GEN match with the shell radius. The times when SNe start for each generation are denoted by orange and cyan vertical dashed lines, respectively. The information of the initial cloud density (n_0) and star formation pairs (ϵ_{SF}) are given in every panel.

the cloud and 1GEN expansion is reversed. After the starburst and with the second cloud expansion, the massive stars are found travelling inward toward the centre. A small contraction of the distribution of the older stars is observed, which is followed by a steady expansion until the end of the simulation. We do not observe a clear effect of the SNe as they mostly start with the clusters already in expansion. On the other hand, 2GEN massive stars (dashed line, empty blue circles) start more concentrated, as described by their initial mass configuration. For 2GEN clusters birthed with $\alpha = 0.3$, the stellar distributions contract and stabilize in a more concentrated state compared to 1GEN, until the moment when SNe start. At 8 Myr, we observe the expansion of these younger stars is less than the older, practically ignoring the change in gravitational potential, and remaining always more concentrated than 1GEN.

For NOSEG simulations, 1GEN massive stars (solid line, filled red squares) begin, as expected, less concentrated than SEG clusters. We note, however, that they show similar dynamical evolution to clusters with initial segregation. The same description can be applied for 2GEN (dashed line, empty blue squares) with central distances always larger than each SEG pair. The effect of the SNe is less visible and after this point, SEG and NOSEG curves approach common values at late times. As before, we observe mass segregation between the different aged populations.

At the moment when the different curves cross the green zone, the older massive stars are more expanded than the younger massive stars. They show different separations and their values are summarized in Tab. 4.2.2 in columns four and five for SEG and NOSEG cases, respectively. The separation cover values between 1.68-4.10 pc. No trend is observed for the different initial density clouds and ϵ_{SF} pairs. Our best and worst models are for SEG sample correspond to $n_0 = 9000$ cm^{-3} with ϵ_{SF} = 0.04-0.20 and $n_0 = 10000$ cm^{-3} with ϵ_{SF} = 0.09-0.20, respectively. For NOSEG sample, our best model is for $n_0 = 6000$ cm^{-3} with ϵ_{SF} = 0.05-0.20 and $n_0 = 10000$ cm^{-3} with ϵ_{SF} = 0.09-0.20, respectively. Even when we refer to them as "worst model", they still show an age-mass segregation. We also find similar low value in SEG sample for $n_0 = 8000$ cm^{-3} with ϵ_{SF} = 0.06-0.20.

4.3.3 All stars distribution

We also study the spatial location of the whole stellar distribution with different Lagrangian radii (R_f). In specific, we use $R_f = 0.1$, 0.3, 0.5 and 0.7 separated by generation. We show the results of R_f in Fig. 4.3.2, where 1GEN is represented by filled symbols and 2GEN by empty symbols. Each R_f has a different symbol and colour described in the legend. SEG and NOSEG simulations are represented by a solid and a dashed line, respectively. The shell radius, the matching zone and the SNe beginning are represented as before. In order to do not over-plot the symbols, we shift the SEG and NOSEG results in ± 0.10 Myr resulting in SEG information first.

As we work with Plummer distribution, SEG and NOSEG mass distributions show initially the same values for the different R_f. After this point, we observe that the global evolution followed by both stellar distributions is very similar, being difficult to make a difference without the shift applied to every snapshot. At the moment of the (re)-collapse, the 1GEN stars are not immediately travelling inwards, as it is also observed when only massive stars

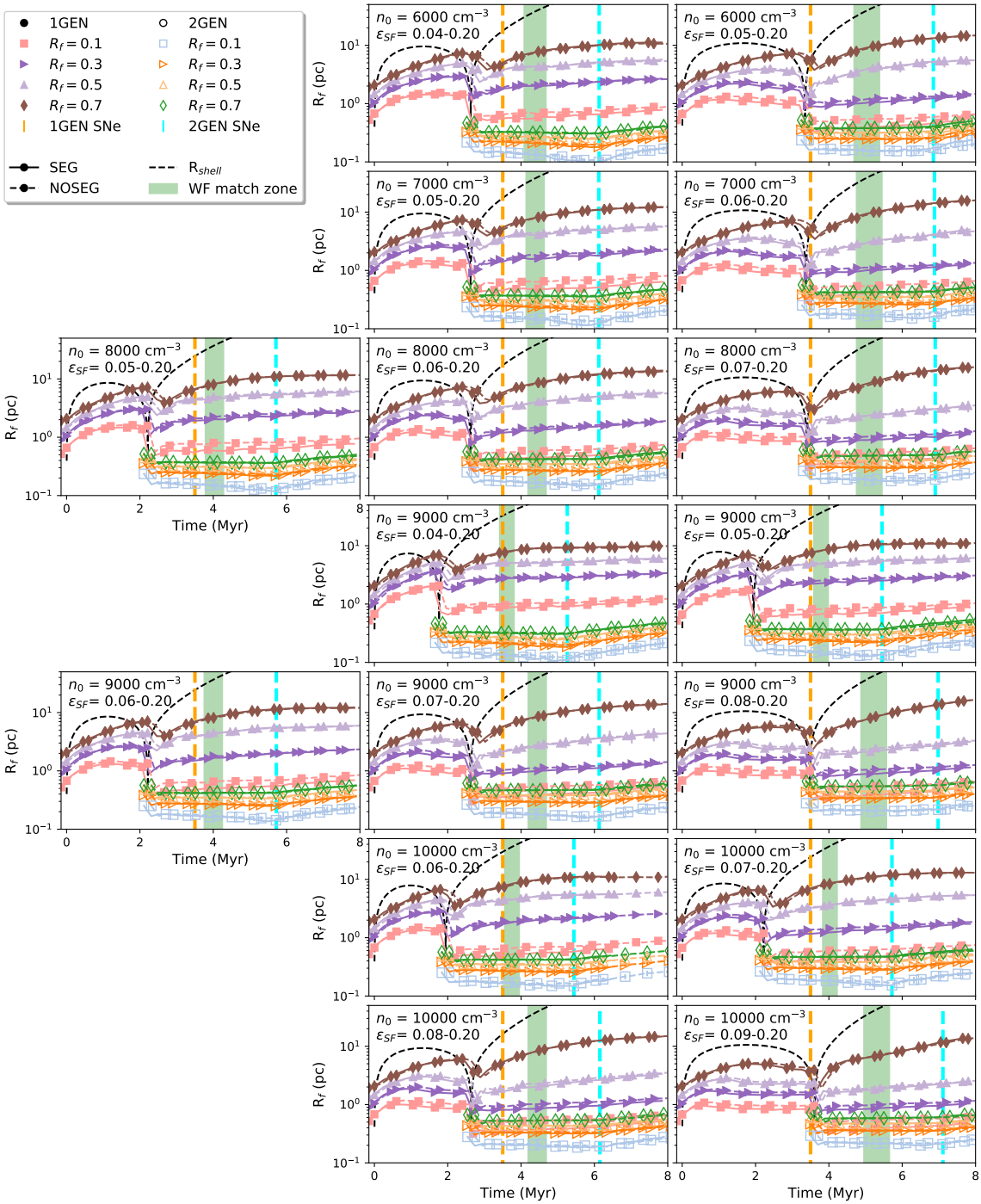

Figure 4.3.2: Lagrangian radii (R_f) vs time. The first generation (1GEN) is denoted by filled symbols and the second generation (2GEN) is denoted by empty symbols. Simulations starting with (SEG) or without (NOSEG) mass segregation are represented by solid lines or dashed lines, respectively. Shell radius, matching zone and SNe times are as Fig. 4.3.1. Each R_f colour is given in the legend.

are analyzed because of the strong gravitational potential produced by the high gas density towards the centre. The different R_f, for the older stellar component, only shrink shortly after the new starburst, as the stars need time to change their velocities that were heading outward. After a small contraction, the expansion is resumed until the end of the simulation. The effect of SNe for the old star generation is not appreciable due to the larger expansion produced by the cloud dispersal. For 2GEN, the cloud expansion is not producing big changes in the stellar distribution as they show roughly constant values after the initial contraction due to our initial virial state, until the point when SNe start when in most cases, a new rate of expansion is observed. The behaviour described above is valid for all our sample. About the final star locations, only until $R_f = 0.1$ of 1GEN (pink filled squares) and in some cases $R_f = 0.3$ (purple right triangles) can be comparable with $R_f = 0.7$ 2GEN (green empty diamonds). The rest of 1GEN R_f are always further away from the main concentration of stars. For the case of $R_f = 0.3$ 1GEN can only be comparable with 2GEN R_f when $\epsilon_{SF} \geq 0.08$, being deeper as the 1GEN stellar mass increases. The shell radius (black dashed line) is always larger than the bigger R_f. It is only smaller when the (re)-collapse phase is reached, but it reaches a larger position very fast after the second starburst. Every panel shows that the new start cluster which is representing R136 is more concentrated than the old stellar component during the whole simulation so during the green zone when WARPFIELD matches the other properties, the N-body simulations also match the observed stellar distribution.

4.3.4 Mass segregation

We use the $\Lambda_{\rm MSR}$ to compare different combinations of star samples from 1GEN, 2GEN or mixed. We consider SEG and NOSEG models separately as we find large differences compared to the analysis above. We measure the mass segregation ratio for the following six combinations:

- Comparison of first generation massive stars (1GEN$_{mas}$) with the first generation low mass stars (1GEN$_{low}$) (red down filled triangles).
- Comparison of 1GEN$_{mas}$ with the rest of the stars (ALL) (pink filled squares).
- Comparison of 1GEN$_{mas}$ together with the second generation massive stars (2GEN$_{mas}$) with ALL (purple filled right triangles).
- Comparison of 2GEN$_{mas}$ with second generation low mass stars (2GEN$_{low}$) (blue down empty triangles).
- Comparison of 2GEN$_{mas}$ with ALL (light blue empty squares).
- Comparison of 1GEN$_{mas}$ with 2GEN$_{mas}$ (orange empty right triangles).

For the SEG sample, we show in Fig. 4.3.3 the previously described combination of $\Lambda_{\rm MSR}$ evolving in time with the panels following the same order as the previous plots. As before the moments when the first SN takes place for 1GEN and 2GEN are indicated by orange and blue vertical dashed lines respectively. The highest level of mass segregation introduced in this sample is detected for the initial conditions at 0 Myr. After this, the gas expulsion occurs and the clusters expand, which produces a reduction in the level of mass segregation. We observe that closely before the second starburst, when the cloud is collapsing and slowly

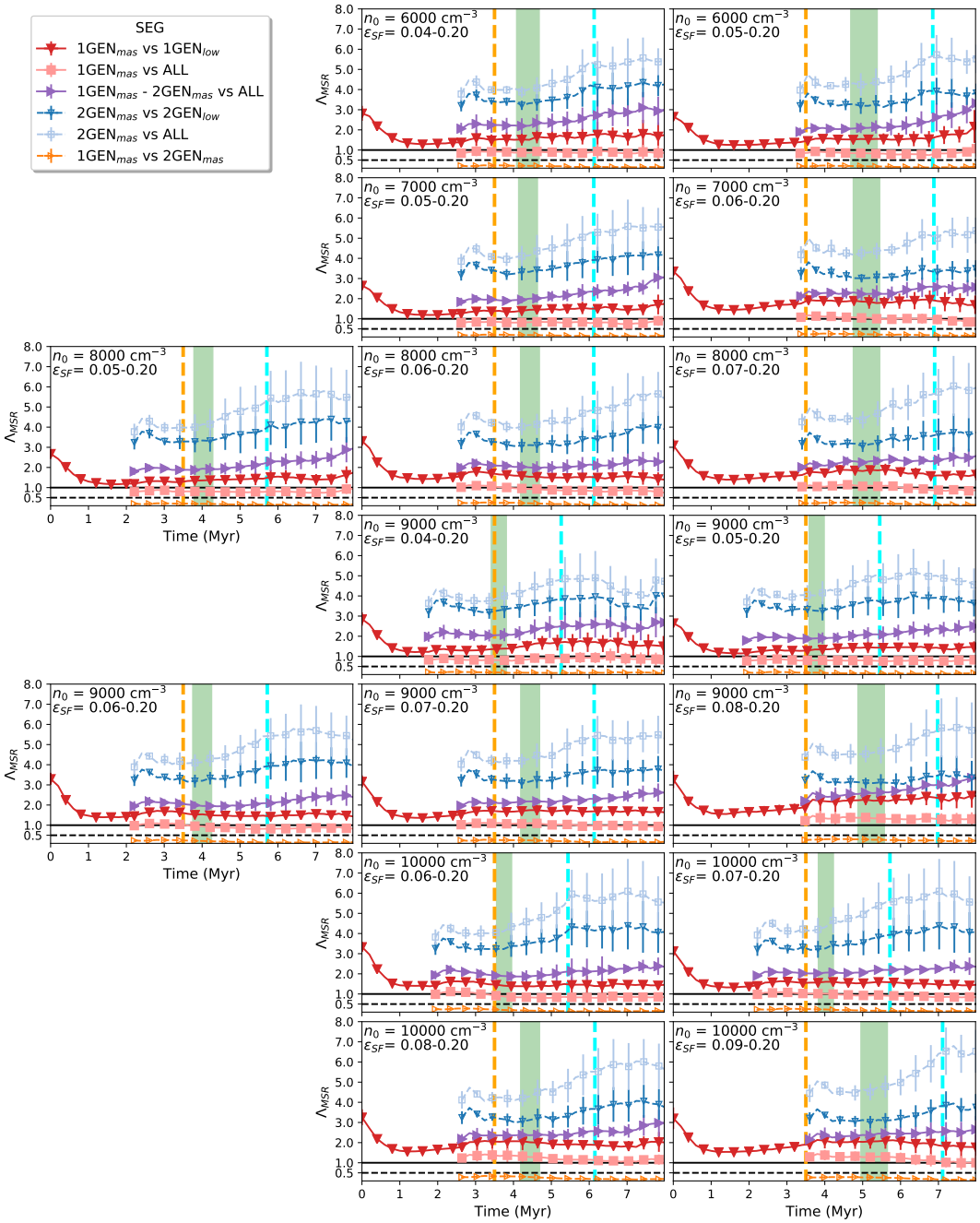

Figure 4.3.3: Mass segregation ($\Lambda_{\rm MSR}$) evolution vs time for simulations starting with mass segregation (SEG) and panels ordered as before. Massive stars from the first generation (1GEN) or second generation (2GEN) are denoted as 1GEN$_{mas}$ and 2GEN$_{mas}$, respectively. Low mass stars are referred as 1GEN$_{low}$ or 2GEN$_{low}$. The rest of the stars excluding the sample of comparison are refereed as ALL. The solid black line shows a value of $\Lambda_{\rm MSR}$ $= 1$ and the dashed black line shows a value of $\Lambda_{\rm MSR} = 0.5$. The vertical orange and blue lines indicate when the first event of SN takes place for 1GEN and 2GEN respectively. The symbols and colours for each comparison sample are shown in the legend.

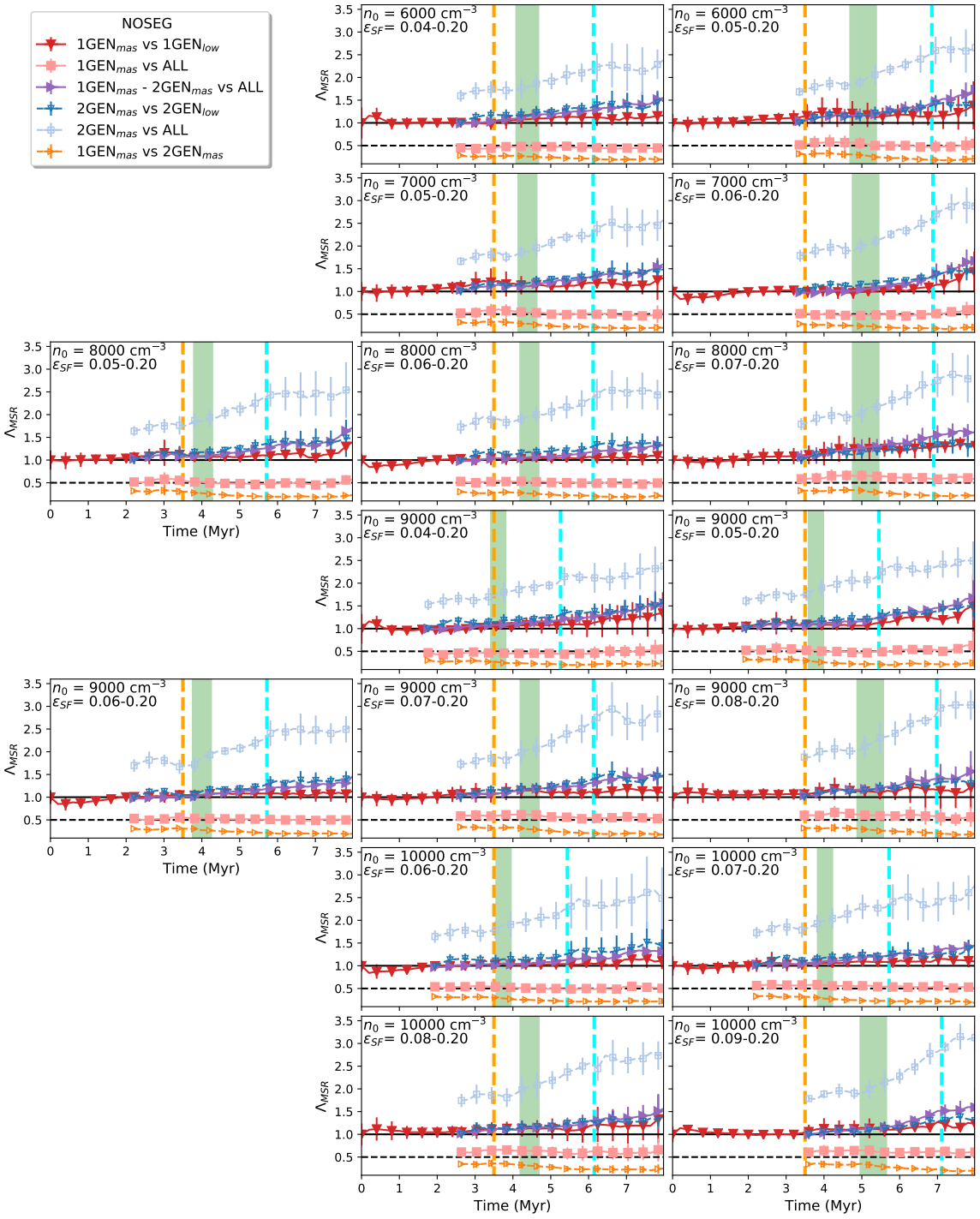

Figure 4.3.4: Same as in Fig. 4.3.3 but now for simulations starting without mass segregation (NOSEG).

bringing stars from outer locations, the level of mass segregation improves in a small degree and around this value is where it stabilizes and remains until the end of the simulation. The rest of the combinations can only start to be measured after the (re)-collapse as they include stars from 2GEN and our observations are based in comparison to the sample just described. Taking again the 1GEN massive stars but now compared to the rest of the stars (1GEN$_{mas}$ vs ALL) shown as pink filled squares, a lower $\Lambda_{\rm MSR}$ is measured with values close to one or at least always below the comparison sample. All massive stars compared to the rest of the stars results (1GEN$_{mass}$ - 2GEN$_{mass}$ vs ALL) are shown with purple right triangles. In this sample, the starting level of mass segregation is higher ($\Lambda_{\rm MSR} \gtrsim 2$), which is followed by a decrease but always higher than the comparison sample. The youngest massive stars compared to their respective low mass stars (2GEN$_{mas}$ vs 2GEN$_{low}$) are shown with empty blue down triangles. The initial level of $\Lambda_{\rm MSR}$ starts with the level of mass segregation introduced as an initial parameter, which is reduced as before, but not as much, then it oscillates and finishes at the end of the simulation with a value close to the initial. The massive stars of 2GEN are compared with the rest of the stars (2GEN$_{mass}$ vs ALL), and the results are shown with light blue empty squares. $\Lambda_{\rm MSR}$ shows higher values as it is including stars from 1GEN which are more expanded than the youngest low mass stars, then it oscillates as the previous sample finishing with values higher than the initial. In some of the cases, the final $\Lambda_{\rm MSR}$ can be similar to the initial if 1 σ error is taken into account. The last combination is the most important for the goal of this study as it describes if the older massive stars are more expanded than the second generation. We denote this comparison as 1GEN$_{mas}$ vs 2GEN$_{mas}$ and it is shown as orange empty right triangles. We observe a very stable value of inverse mass segregation for all the cases remaining close to the level of mass segregation at the moment when the second stellar generation is introduced to the simulation. At the end of the simulation, we measure values of $\Lambda_{\rm MSR}$ comparable or even less to the initial. The moments of the first SNe for each generation are shown with a dashed vertical orange and blue line respectively. The SNe of the 1GEN are not producing a big change on the value of $\Lambda_{\rm MSR}$ but for the cases which include 2GEN as the comparison sample alone, the SNe are producing instabilities on the $\Lambda_{\rm MSR}$ parameter producing that the rate of increase is reduced and in some cases, when more SNe events are possible, even a decreasing trend towards the end. At the moment when the other observational parameters match the values in the literature (green zone), for all cases, the youngest stellar generation, which is representing R136, is more concentrated than the older stars.

For the NOSEG sample, we show the result for the same combinations described before in Fig. 4.3.4. Initially, we find $\Lambda_{\rm MSR} = 1$ as we set up the simulation. Some small decreases or increases are observed but quickly returning to one. After the (re)-collapse, small increases are observed in $\Lambda_{\rm MSR}$, with the simulations ending at values slightly above one, with maximum values during the simulation typically $\Lambda_{\rm MSR} \sim 1.5$. $\Lambda_{\rm MSR}$ remains close to 1.0 as a result of the fairly uniform global expansion of the cluster (see Sec. 4.3.3). From this, we may infer that massive stars are scattered almost at the same level as the low mass stars. When we start to measure 1GEN$_{mas}$ vs ALL after the (re)-collapse, we observe that $\Lambda_{\rm MSR} < 1$, as the old stellar component has already expanded, it finds a new cluster more concentrated in the centre and in consequence $\Lambda_{\rm MSR}$ detects inverse mass segregation. The

level of mass segregation remains stable until the end of the simulation with a value of $\sim$ 0.5. The massive stars of both generation compared with the low mass component shows as 1GEN$_{mass}$ - 2GEN$_{mass}$ vs ALL starts with a $\Lambda_{\rm MSR} \sim 1.0$ but continuously increasing with values closely above the $\Lambda_{\rm MSR}$ for 1GEN$_{mas}$ vs 1GEN$_{low}$. At the end of the simulation, we detect a minimum mass segregation of 1.5 and taking into account 1 σ error a few maximum values of 2. The 2GEN$_{mas}$ vs 2GEN$_{low}$ comparison shows initially a $\Lambda_{\rm MSR} = 1.0$, as we set up followed by a slow increase until the end of the simulation following closely the previous sample overlapping in the average level of mass segregation finishing with similar values. Comparing all the stars with the massive stars of the new cluster, as 2GEN$_{mass}$ vs ALL, an initial level of mass segregation of at least 1.5 is detected followed by a continuous increase until the end of the simulation. The final $\Lambda_{\rm MSR}$ at 8 Myr are always larger than 2 with most of the cases showing $\Lambda_{\rm MSR} \sim 2.5$ and a few maximum average values of 3. The comparison of the old and young massive component defined as 1GEN$_{mas}$ vs 2GEN$_{mas}$ shows inverse mass segregation with $\Lambda_{\rm MSR} < 0.5$ during the whole time of measurement. This value slowly decreases, reaching a level of mass segregation even smaller than the initial. The SNe effect follows the same description as the SEG case showing also instabilities from the moment the SNe for the 2GEN start to take place. At the moment when this last comparison sample is inside the green zone, all the cases show inverse mass segregation as we are aiming to achieve.

4.3.5 Stellar distributions

To have a better appreciation of how are the different stellar components evolving at different times, we show in Fig. 4.3.5 and 4.3.6 two examples of one simulation with an initial cloud density of $n_0 = 1000$ cm^{-3}, with SEG and NOSEG respectively. We transform mass to luminosity for each star according to Gräfener et al. (2011) and calculate $\sum_{\rm v}$ in (L$_\odot$/pc^2). The initial embedded star cluster has a $\epsilon_{SF} = 0.07$ and the second cluster has a $\epsilon_{SF} = 0.20$. We show 3 snapshots at different times, from top to bottom, at 0 Myr, at 2.22 Myr which is the (re)-collapse moment and at 4.22 Myr when the simulation match all the properties for NGC 2070. The panels show the stellar components separated from left to right 1GEN$_{mass}$ (1GEN massive stars), 1GEN$_{low}$ (1GEN low mass stars), 2GEN$_{mass}$ (2GEN massive stars) and 2GEN$_{low}$ (2GEN low mass stars) with their respective $\Lambda_{\rm MSR}$ and Time (age).

In Fig. 4.3.5 top panels show the show the initial stellar configuration starting with a $\Lambda_{\rm MSR} = 1.02$ (NOSEG) as we force to have. In the second row, the 1GEN is more spread, especially for the 1GEN$_{mass}$ which shows, at this stage, inverse mass segregation. At this moment, the 2GEN is added to the simulation also with a $\Lambda_{\rm MSR} = 1.01$. The comparison between the stellar generations shows a $\Lambda_{\rm MSR} = 0.43$ i.e., already inverse age mass segregation. The simulation evolves until 4.22 Myr and its stellar components are shown in the bottom panels. The 1GEN, in general, is much more spread than 2GEN. The value of $\Lambda_{\rm MSR}$ has not considerably changed and still shows inverse mass segregation as we are aiming to find.

In Fig. 4.3.6 we show the same panels' arrangement previously described but now for stellar distribution starting with mass segregation (SEG). The $\Lambda_{\rm MSR}$ values at different snap-

shots show the fixed initial mass segregation. The 1GEN reduces its $\Lambda_{\rm MSR}$ value as a result of the initial expansion. At the moment of the inclusion of the 2GEN, the comparison between both stellar generations shows a cluster highly inverse segregated with a $\Lambda_{\rm MSR} = 0.29$. When the simulation reaches the properties of NGC 2070, the bottom panels show a spread 1GEN and a more concentrated 2GEN also showing inverse mass segregation. The level of mass segregation is reduced but still producing the object we intend to find.

For SEG and NOSEG cases, we end up with a 2GEN more concentrated than the 1GEN. In the first case, only taking into account the more luminous stars (more massive) this can be less distinguishable as the luminosity is more evenly distributed. In the second case, the initial mass segregation helps the most luminous stars to be located closer to each other producing a central zone more luminous. At 4.22 Myr, in both cases, the 1GEN has already suffered SNe events plus the initial cloud expansion which can remove stars from the central zone reducing the core zone luminosity.

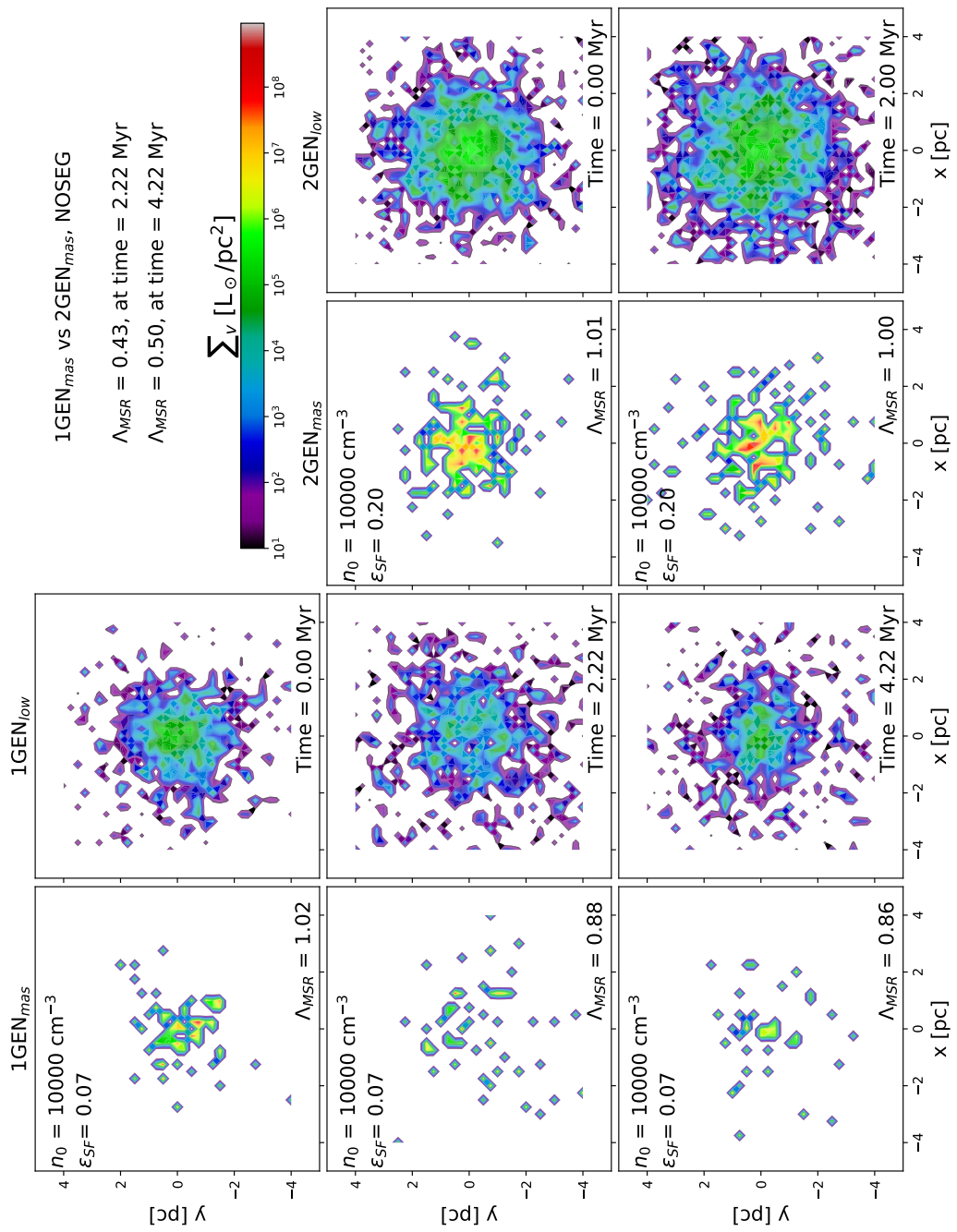

Figure 4.3.5: Simulation central zone snapshots at three different times, from top to bottom: first star burst, second star burst and at the moment when the simulation match the properties of R136 and $R_{\rm shell} = 37.1$ pc. The left two panels show the 1GEN stellar component separated by massive (left) and low mass stars (right). The right two panels also show the different stellar components but for the 2GEN. Both stellar generations start with NOSEG distribution.

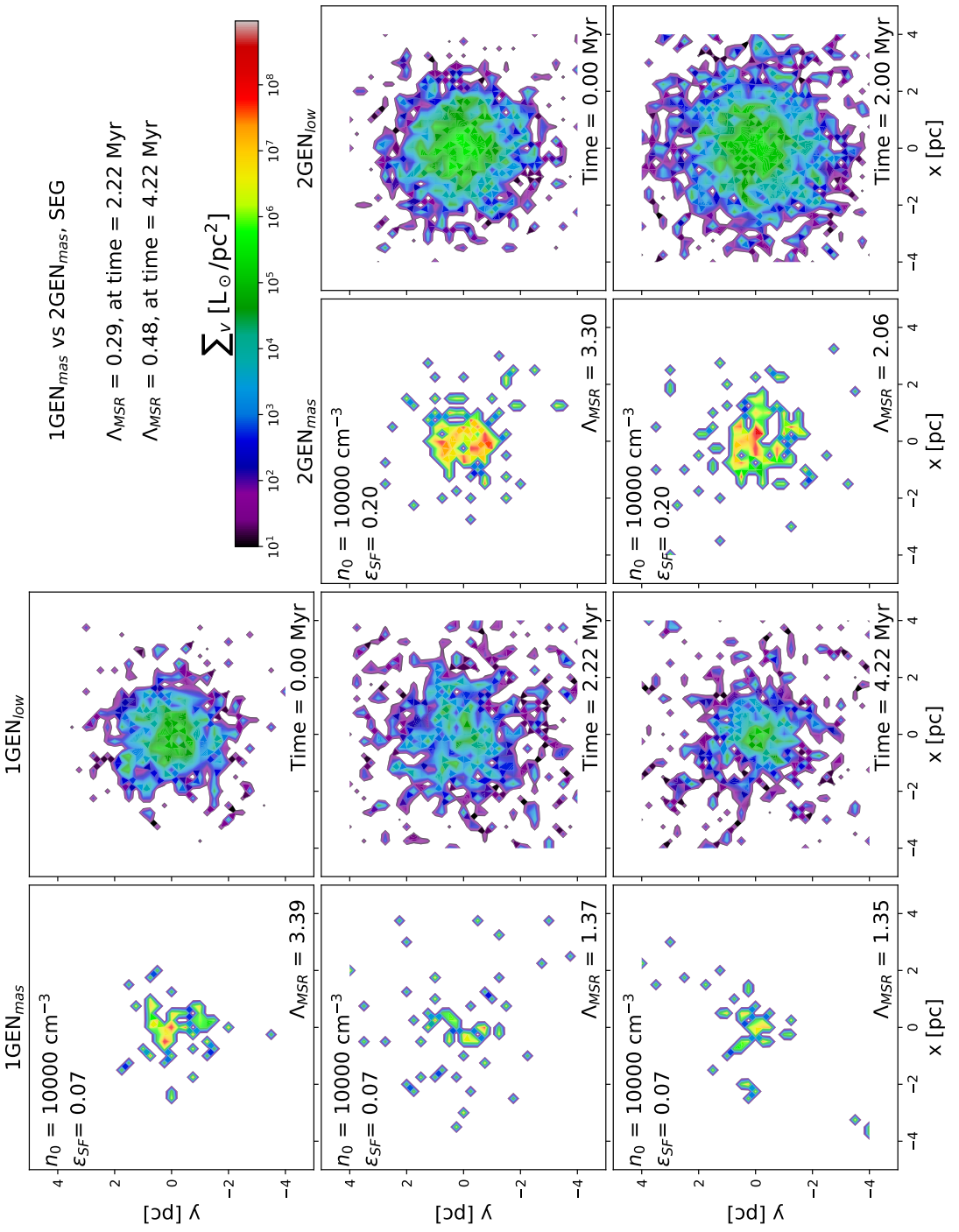

Figure 4.3.6: Same as Fig. 4.3.5 but for both stellar generations starting with SEG distribution.

4.4 Observational measurements

We compute the $\Lambda_{\rm MSR}$ and density profile of the central zone of our simulations for snapshots at 1.0, 1.5 and 2.0 Myr, trying to match with the observational measurements done by K2021. In our simulations, we have accurate positions, masses and ages for all the particles which for an observational study is not achievable. K2021 presented a detection mass sensitivity which is low in the central zone and it is increasing towards the outer parts. We blind our sample according to the probability of detection presented by them (see Figure 11, bottom panel in K2021). In our simulations, we have two stellar components which would be difficult to distinguish directly in an observation, especially in the small and concentrated central zone. In order to study both cases, we proceed excluding and including the old stars. We find no significant differences between our models, hence, we present the best match which corresponds to the simulations starting with a cloud of n_0 = 10000 cm^{-3} and initial clusters with ϵ_{SF}= 0.07 followed, after the (re)-collapse, by our representation of R136 with ϵ_{SF}= 0.20. We present our results using the same plots and units presented by K2021 for a direct comparison.

4.4.1 Central mass segregation

We measure the $\Lambda_{\rm MSR}$ parameter following the methodology in K2021 including their completeness limitation and observational biases. In Fig. 4.4.1, top panels, we show the $\Lambda_{\rm MSR}$ calculated for different sample sizes of chosen random stars ($N_{\rm MST}$). The cyan zone represents the 1 sigma range from K2021. In the left panel, where the old stars are excluded, our simulations show a flatter trend than the observational results. The central values of $\Lambda_{\rm MSR}$ match the central zone for some cases only for $N_{\rm MST} \leq 100$ and for larger $N_{\rm MST}$ we can only reach the cyan zone through the 1 sigma error. In the right panel, where we include the stars from the old component, shows an even flatter curve, with central values below and above the cyan zone. For this case, some of the central $\Lambda_{\rm MSR}$ values are matching for $N_{\rm MST} \leq 150$. The 1 sigma ranges as well, for most of the cases, reach the observational zone but with less spread as we increase the $N_{\rm MST}$. The differences between the different 2GEN ages or initial mass segregation are small. In the bottom panels, we measure the level of mass segregation for different radii. We can only match the cyan zone for $R \geq 0.4$ pc, taking into account the 1 sigma error. At a $R = 0.2$ pc, our results show a $\Lambda_{\rm MSR}$ close to 1 but K2021 shows a larger value of mass segregation, being the only radius where we measure the largest differences between our studies as the cyan zone is never reached either excluding or not the older component. The different time snapshots show similar average values or at least intersect the 1 sigma error.

4.4.2 Central density profile

We measure the 2D mass density profiles for a given radius as it was done by K2021 and we summarize the results in Fig. 4.4.2 top panel. The different curves are the mass density profiles shown in K2021 at different estimated ages. Our results are matching the curve close to the centre ($R < 0.2$ pc) and staying slightly above until $R \sim 1$ pc where again match

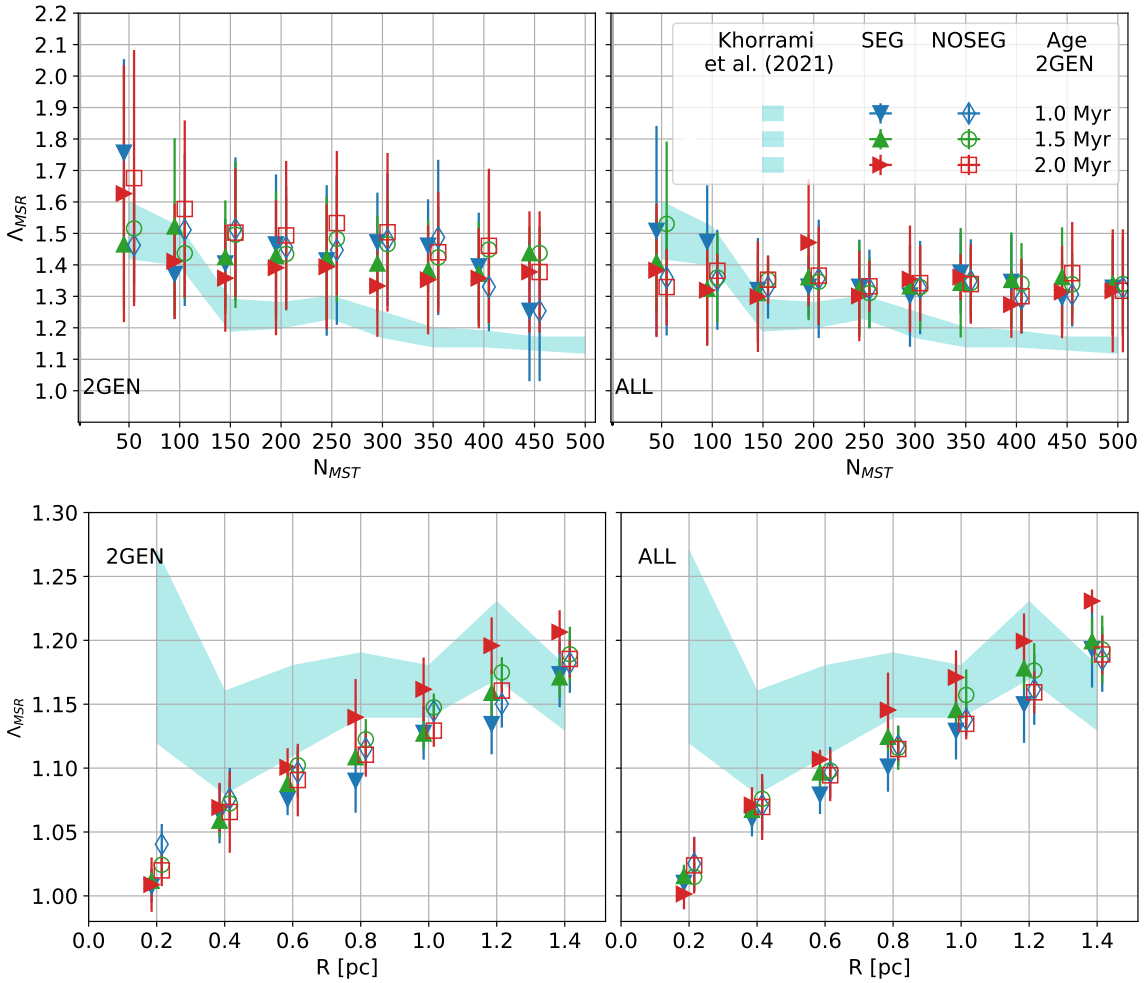

Figure 4.4.1: Top panel shows the level of mass segregation ($\Lambda_{\rm MSR}$) measured for different sample sizes of chosen random stars ($N_{\rm MST}$). The bottom panel shows $\Lambda_{\rm MSR}$ for different radii. The left and right panels show the results excluding (2GEN) or including (ALL) the old stellar component, respectively. The cyan zones are the observational values from K2021. The different time snapshots and initial mass segregation are indicated by different symbols as the legend denotes. The initial conditions for this case are a cloud of n_0 = 10000 cm^{-3} and star clusters according to ϵ_{SF}= 0.07-0.20.

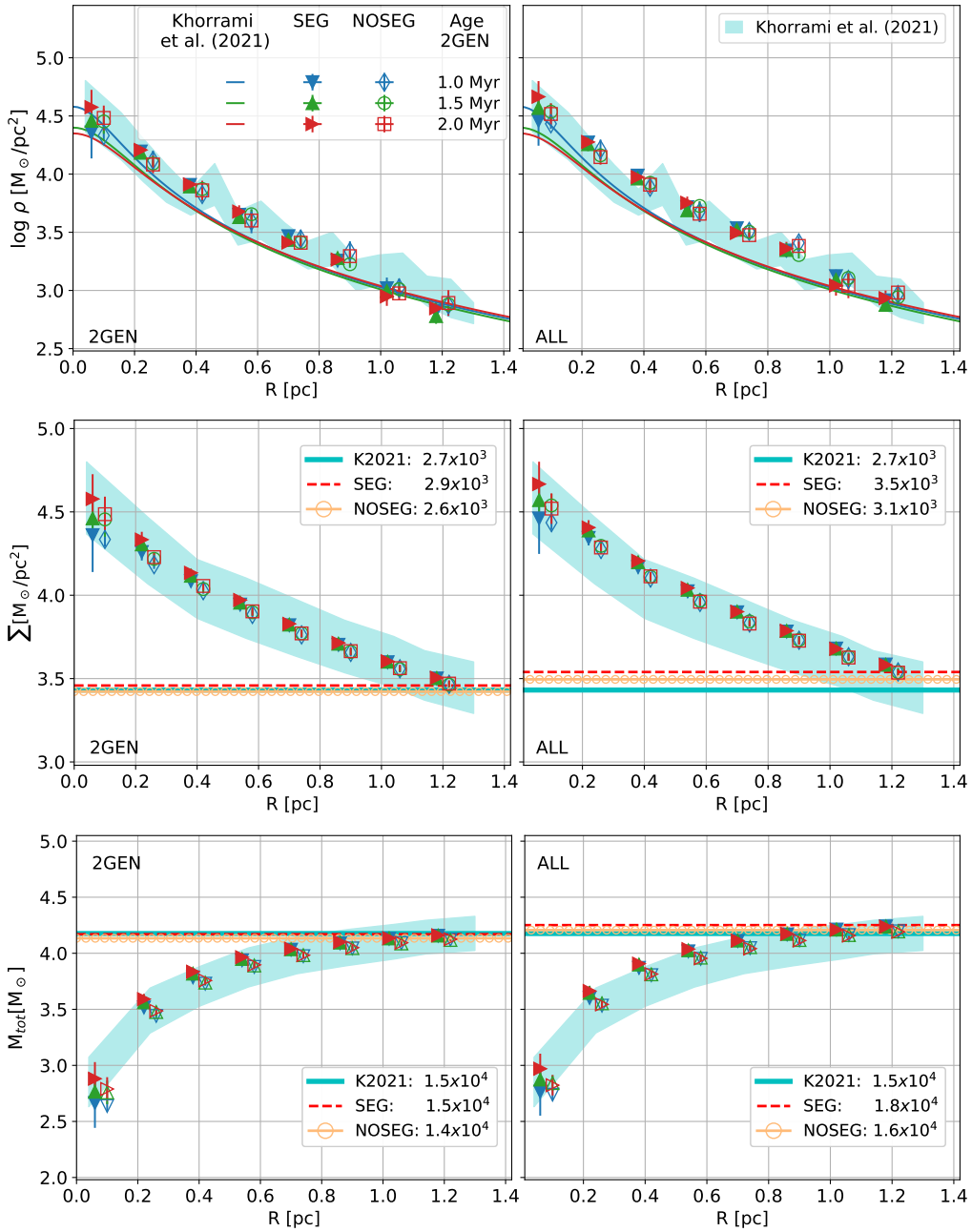

Figure 4.4.2: Top panels show the projected mass density (ρ) of the central zone. The different curves show the fitting lines from the observational study (K2021). The central panels show the surface density ($\sum$) within a given radius. The bottom panels show the total stellar mass ($M_{\rm tot}$) within a given radius. The left and right panels show the results excluding (2GEN) or including (ALL) the old stellar component. The cyan lines in the central and bottom panels are the observational values from K2021 and the red line and orange circles are the respective values for simulations starting with mass segregation and not, respectively. The different time snapshots and initial mass segregation are indicated by different symbols as the legend denotes. The initial conditions for this case are n_0 = 10000 cm^{-3} and ϵ_{SF}= 0.07-0.20.

the solid lines. The same behaviour is shown when the old component is excluded or not. We do not observe big differences for any time snapshots or initial mass segregation. The results shown in K2021 are also not matching the curves perfectly as we can see from the cyan zone which denotes the spread of the results measured by the authors. In the central panels, we show the surface density for different given radii. We find that our results follow similar curves but the final values show differences. The final mass density found by K2021 is $\sum = 2.7 \times 10^3$ M$_\odot$/pc^2 and our best match in this case is given in the left panel with small differences as -0.1×10^3 M$_\odot$/pc^2 and $+0.2 \times 10^3$ M$_\odot$/pc^2 for NOSEG and SEG simulations respectively. In the right panel, where all stars are included, higher surface densities in the order of $\geq +0.4$ M$_\odot$/pc^2. The results are in both cases inside the cyan zone but when the old component is included the values approach the top limit. In the bottom panels, we show the stellar mass for given radii. As before, the closest values are observed in the left panels. K2021 estimated a total mass of M$_{\rm tot} = 1.5 \times 10^4$ M$_\odot$ and our results can match this value for SEG simulations and with a difference of less than 10% (-0.1×10^4 M$_\odot$) for NOSEG simulations. In the right panel, NOSEG simulations also find a close value with a difference of less than 10% ($+0.1 \times 10^4$ M$_\odot$). Simulations starting with mass segregation enclose more mass, resulting in a value above the observation measurement of $+0.3 \times 10^4$ M$_\odot$. We also observe that in the right panel our results are closer to the top limits of the cyan zone.

4.5 Discussion

In this chapter we demonstrate that the stellar distribution observed in NGC 2070 is consistent with an older stellar cluster, dynamically relaxed, hosting in its centre a youngest more massive star cluster known as R136. We achieve this through N-body simulations coupled with a semi-analytic 1D model for evolution of cloud/cluster systems.

We evolve a molecular cloud initially with $M_{\rm cloud} = 3.16 \times 10^5$ M$_\odot$ trying initial uniform densities (n_0) between 6000-10000 cm^{-3} holding different star clusters leading in ϵ_{SF} between 0.04-0.09. We scale the velocities in order to obtain dynamical equilibrium ($\alpha = 0.5$). All the combinations shown in this chapter include clusters which produce insufficient feedback to dissolve the cloud, despite being massive and young. As a consequence, the cloud (re)-collapses and a second starburst occurs. We fix this second star cluster to have a ϵ_{SF} = 0.20. The last imposition is made in order to have more time to match the ages of both stellar generations and the shell radius. After several attempts exploring the best parameter space to reproduce the properties of R136, we find that a second star cluster starting in dynamical equilibrium is not able to match observations. We explore different α, and we find that the best dynamical state for the new stellar component is $\alpha = 0.3$ i.e., the second cloud expansion is holding a new cluster that is initially contracting. The dynamics of the second cluster is affected by the dynamics of an expanded older less massive stellar component and the expanding cloud which is removing gravitational potential. We also explore if our results can vary if both stars clusters start with mass segregation or not. In this chapter, we only include a summary of the results for the successful α.

We study NGC 2070 as a whole measuring the average distances to the centre for only

the massive stars ($M > 20$ M$_\odot$) weighted by their luminosity. We find for all the cases that the new massive stars stay captive closer to the centre and the remaining older massive stars are at further locations as is observed in NGC 2070. It is important to mention that this is not saying that there are no old massive stars close to the centre, in fact, we detect them but they are not that many to reduce the average central distance. We observe that the different stellar components can be more easily recognized if the star clusters start with mass segregation as the new massive stars are found much more concentrated than their pairs. At later stages, the expansion of the new stellar component is larger and we achieve this as a consequence of the SNe which have more time to be produced. The massive stars which belong to the clusters starting with mass segregation are found, on average, closer to the centre due to their initial imposed configurations and this difference is more visible for the newer massive stars.

We continue studying the Lagrangian radii of both stellar components. We observe that independent of the initial level of mass segregation, the old stellar component is always found to be more extended than the new cluster. The initial contraction for the second stellar generation because of our imposed virial ratio is visible along all the layers. Its expansion is stronger when the new SNe start to be produced at later stages of our simulations but does not influence the matching scenarios as this occurs later than the moment when all the NGC 2070 properties are intersecting. The clusters which start with mass segregation are slightly more concentrated than their pairs and this is observable through our complete sample.

To quantify our model in a physical way, we measure the level of mass segregation for the different cases using the $\Lambda_{\rm MSR}$ parameter. As the new stellar component is more concentrated than the old star cluster, we expect to find a $\Lambda_{\rm MSR} < 1$, when we compare the massive stars from the older generation with the new massive stars. We show the results in separated plots this time as the initial $\Lambda_{\rm MSR}$ differ highly when we start with mass segregation ($\Lambda_{\rm MSR} >> 1$) or not ($\Lambda_{\rm MSR} \sim 1$). The old cluster which starts with mass segregation loses this configuration due to the cloud expansion and at the moment of the inclusion of the new star cluster, their $\Lambda_{\rm MSR} \gtrsim 1$ i.e., a cluster without mass segregation as their pairs which at the same moment also exhibit the same distribution. After the inclusion of the new clusters, the comparison between the different samples shows similar behaviours. At the moment when the properties in WARPFIELD are matched every combination of initial conditions show a value $\Lambda_{\rm MSR} \sim 0.5$ for the cases without initial mass segregation or even less when we start with segregated clusters. Along our whole parameter space, the NGC 2070 stellar configuration is detected regardless of any of the conditions on the initial conditions here used.

We also compare to the study of K2021, who present observations of the central region of NGC 2070 where the younger cluster R136 is located and discuss the resulting radial mass segregation and density profiles. We proceed as closely as possible to their approach and we find a good match with the observations. Unlike the results on mass segregation previously exposed, we exclude any star with a central distance larger than 1.4 pc, as the observational study has done. We can closely match the descending trend for the $\Lambda_{\rm MSR}$ parameter as we increase the size of the sample ($N_{\rm MST}$). Using only the new stellar component which in this

work represent R136, we do not match the exact central values for every case, but our 1 sigma error bars are always close to the observational values. Adding the remaining stars from the old stellar component in this zone, we can match the central values. This means some older stars can also be contaminating the observational study. We measure $\Lambda_{\rm MSR}$ at different central distances and we find an increasing trend. The increasing trend is also found by K2021, with only one exception at a central distance of 0.2 pc. This discrepancy is found with or without the old stellar component. Our central values are slightly below the observational results but always intersected by 1 sigma error bars. It has been detected, very close to the R136 centre, a star with a mass $\sim$ 300 $M_\odot$, but in this work, we did not extend our initial mass function further than $\sim$ 120 $M_\odot$ as expecting to find this massive star in our simulation also very close to the centre can be challenged due to the stochastic dynamical interactions. This star in the very centre taken into account by observers improves the value of mass segregation at R $\leq$ 0.2 pc showing the biggest difference between our works. In the referenced study, the values of mass segregation cover a range of $1.0 \leq \Lambda_{\rm MSR} \leq 1.28$ which is very small for this parameter and it can vary easily depending on the random star selection (Allison et al. 2009b). For radial density profiles, we find good agreement between observations and our simulations. We can match very accurately the observational values with our central values. We can only match these radial profiles if at the moment of the introduction of the new star cluster, instead of being in equilibrium, it is contracting. We try with different virial ratios ($\alpha \leq 0.5$) and the best agreement with observations is $\alpha = 0.3$ which are the results presented in this chapter. We find this independent of the initial mass segregation, initial cloud density, and star formation efficiency pairs.

4.6 Conclusions

We conclude that an evolving molecular cloud with an initial mass of 3.16×10^5 $M_\odot$ giving birth to two stellar generations can well reproduce the observational characteristics of the central region of 30 Doradus in the Large Magellanic Cloud. Our model of an older first-generation star cluster with a mass between 1.26×10^4 $M_\odot$ and 2.85×10^4 $M_\odot$, starting in virial equilibrium, followed by a younger second-generation cluster of $\approx 6.32 \times 10^4$ $M_\odot$, starting contracting with a virial ratio of 0.3, can match the stellar configuration observed in NGC 2070 consisting in an old expanded cluster hosting in its centre a youngest more massive star cluster known as R136. The resulting new stellar component shows close agreement with mass segregation observations of R136 excepting the very central zone ($R < 0.2$ pc) where a $\sim$ 300 $M_\odot$ is located which has been not included in this work. Whether we include remnants from the old component or not, our simulations match the density profile of the central zone of NGC 2070. Therefore, this result is independent of the probable contamination by old stars in K2021.

We caution that there may be other configurations that lead to an equally good match to the observational constraints. The approach presented here is kept simple in order to allow for the investigation of a large parameter space. Subsequent studies based on complex and computationally more expensive 3D radiation-hydrodynamic simulation can use our best fit

model as starting point.

We observe that the second stellar generation, representing R136, remains more concentrated than the first generation, which can be well understood as a natural outcome of the stellar dynamical evolution in the time-varying potential. We mention, that the WARPFIELD model could in principle produce more massive star clusters that also match the ages and shell radius of NGC 2070, however, in these cases the spatial distribution of stars is typically too extended to be compatible with the observational constraints.

5

Summary and future work

Along this thesis we have approach to the observed fact that star clusters are not surviving after gas expulsion. According to the classical picture, embedded star clusters which are gas dominated, i.e., low star formation efficiency, do not survive after they disrupt their molecular clouds. In this chapter, we summarize the main results and discuss about future work.

5.1 Summary

5.1.1 Substructured star clusters embedded in statistics background potentials

In the first part of this thesis, we review the approximations proposed in Farias et al. (2015, 2018b) contemplated for star clusters with equal mass particles. We show that with more realistic initial conditions it is still possible to predict the mass-bound fraction remaining for low-mass embedded star clusters after gas expulsion. With the inclusion of different masses (more similar to the observed Universe) and mass segregation, we obtain mass bound fractions, on average, slightly smaller than the predictions, but still with 1 sigma significance. Our results show that mass segregation does not strongly increase or decrease the chances of embedded star clusters surviving the gas expulsion phase, as the level of mass segregation in substructured star clusters is rapidly reduced by the internal stellar dynamics (Allison et al. 2010; Domínguez et al. 2017).

5.1.2 Spherical star clusters embedded in evolving molecular clouds

In the second part of this thesis, we study whether simulated star clusters embedded in giant molecular clouds with extremely low star formation efficiencies also overcome the gas expulsion process with one or two-star formation events. We develop a framework where the semi-analytic 1D molecular cloud model WARPFIELD is bridged with the N-body code NBODY6++GPU. We study the evolution in time of different embedded star clusters where WARPFIELD simulates the evolving molecular clouds and continuously updates the background potentials which NBODY6++GPU includes in the dynamics of the corresponding simulated star clusters.

Our results with one star formation event show that embedded star clusters can survive the gas expulsion phase. The star clusters experience expansion as the molecular clouds are expelled but in comparison with embedded star clusters, as the classical picture shows, they stabilize their sizes and only keep expanding as supernova events occur.

Our results of star clusters with two-star formation events show that they can also survive this different molecular cloud evolution. The older star clusters experience the initial gas expansions as in the classical picture but are stopped and reversed at the moment when the molecular clouds (re)-collapse and produce the second-star burst. The consecutive molecular cloud disruptions expand both stellar generations finishing more extended than the single generation clusters but still less than the clusters suffering the violent gas expulsion that the classical picture presents.

Both scenarios fulfill the star formation efficiency range of 0.01 to 0.10, which does not agree with the values found in the literature where no survival star clusters should be expected.

5.1.3 Observation framework test

As a continuation of the study presented in the second part of this thesis, we use the framework developed in chapter 3 to reproduce the embedded star cluster NGC 2070. This object contains a younger stellar generation, in its centre, which is surrounded by an older population. As the literature proposes the scenario of cloud (re)-collapse, we test whether is possible to reproduce its properties: first and second stellar mass, molecular cloud shell radius and young stellar component more concentrated than the old stellar generation. Following recent studies, we also try to match the radial mass density profile with the specific values of mass segregation.

We develop a grid of N-body simulations covering different combinations of initial conditions. We can reproduce the global properties of NGC 2070 and the detailed central structure recently studied by Khorrami et al. (2021). An initial molecular cloud with a mass of $M_{\rm cloud} = 10^{5.5}$ $M_\odot$ hosting a star cluster with a star formation efficiency range between 0.04-0.09. After an initial expansion and the posterior (re)-collapse, we test a new starburst produced with a star formation efficiency of 0.20, mimicking the central object in NGC 2070: R136. Both star components expand the cloud until the moment that the cloud radius and the stellar ages are showing values according to the literature. To match the central stel-

lar structure of our simulations with the observations, we test different virial states for the younger star cluster finding that instead of a new stellar component in equilibrium with the molecular cloud and the old cluster, a collapsing initial state has to be imposed. With this setup and by using our developed framework, we successfully found a possible progenitor for NGC 2070.

5.2 Future work

Although, as a result of this thesis, we could show that embedded star clusters can survive the gas expulsion phase along the complete range of star formation efficiency, the story does not end. In this work we explore initial conditions very close to the classical picture to be able to compare and understand how the inclusion of more realistic initial conditions are impacting in the final output. In other words, by using WARPFIELD and considering the multiple stellar generations output, we investigate a simplistic approach to remain close to the classical picture and many possible variations are yet left to be explored.

In chapter 4, we briefly explored how different star formation efficiencies and virial state for each of the stellar components can behave. We use a second stellar component more massive and initially shrinking instead to start in virial equilibrium to closely reproduce the density profile and mass segregation of R136. Yet, more extensive investigations are necessary to learn whether the age mass segregation is a common output for multiple generations embedded star clusters or not. Another parameter that can be explored is the virial ratio state of the younger stellar component as an imposed condition to increase or decrease the star clusters' survival chances. This does not have a simple answer, as e.g., a second starburst producing a star cluster which is initially strongly shrinking can improve its chances to survive gas expulsion but probably very destructive for the older stellar component which as expands also removes gravitational potential also affecting the younger star cluster.

In reality, star clusters with multiple stellar generations are not limited to be only two. For instance, Beccari et al. (2017) claimed to detect three stellar populations in the Orion Nebula Cluster where each from the youngest to the oldest are more concentrated than the previous older one. The framework developed in chapter 3 can be applied to find possible progenitors for these kind of objects and constraints possible initial conditions for more detailed and expensive simulations.

Last but not least, our results suggest that every star cluster embedded in WARPFIELD giant molecular clouds with uniform density profiles survives gas expulsion. This result can be revised by using more dense clouds and different density profiles as, e.g., Parmentier and Pfalzner (2013) proposed which has been already shown to improve the star clusters survival when the gas is instantaneously removed (Shukirgaliyev et al. 2017). By using Parmentier and Pfalzner (2013) density profile and WARPFIELD clouds evolution more accurate studies can be developed.

Acknowledgments

I would like to dedicate the final note to my thesis to all the people who have made this PhD in astronomy possible and unforgettable, and who have supported me over the past four years.

References

Abel, N. P. and Ferland, G. J. (2006). Determining the H^+ Region / PDR Equation of State in Star-forming Regions. *ApJ*, 647, 367.

Adams, F. C. (2000). Theoretical Models of Young Open Star Clusters: Effects of a Gaseous Component and Gas Removal. *ApJ*, 542, 964.

Allison, R. J., Goodwin, S. P., Parker, R. J., de Grijs, R., Portegies Zwart, S. F., and Kouwenhoven, M. B. N. (2009a). Dynamical Mass Segregation on a Very Short Timescale. *ApJL*, 700, L99.

Allison, R. J., Goodwin, S. P., Parker, R. J., Portegies Zwart, S. F., and de Grijs, R. (2010). The early dynamical evolution of cool, clumpy star clusters. *MNRAS*, 407, 1098.

Allison, R. J., Goodwin, S. P., Parker, R. J., Portegies Zwart, S. F., de Grijs, R., and Kouwenhoven, M. B. N. (2009b). Using the minimum spanning tree to trace mass segregation. *MNRAS*, 395, 1449.

Andersen, M., Zinnecker, H., Moneti, A., McCaughrean, M. J., Brandl, B., Brandner, W., Meylan, G., and Hunter, D. (2009). The Low-Mass Initial Mass Function in the 30 Doradus Starburst Cluster. *ApJ*, 707, 1347.

Bastian, N. and Goodwin, S. P. (2006). Evidence for the strong effect of gas removal on the internal dynamics of young stellar clusters. *MNRAS*, 369, L9.

Baumgardt, H. and Kroupa, P. (2007). A comprehensive set of simulations studying the influence of gas expulsion on star cluster evolution. *MNRAS*, 380, 1589.

Beccari, G., Petr-Gotzens, M. G., Boffin, H. M. J., Romaniello, M., Fedele, D., Carraro, G., De Marchi, G., de Wit, W. J., Drew, J. E., Kalari, V. M., Manara, C. F., Martin, E. L., Mieske, S., Panagia, N., Testi, L., Vink, J. S., Walsh, J. R., and Wright, N. J. (2017). A tale of three cities. OmegaCAM discovers multiple sequences in the color-magnitude diagram of the Orion Nebula Cluster. *A&A*, 604, A22.

Bestenlehner, J. M., Crowther, P. A., Caballero-Nieves, S. M., Schneider, F. R. N., Simón-Díaz, S., Brands, S. A., de Koter, A., Gräfener, G., Herrero, A., Langer, N., Lennon, D. J., Maíz Apellániz, J., Puls, J., and Vink, J. S. (2020). The R136 star cluster dissected with Hubble Space Telescope/STIS - II. Physical properties of the most massive stars in R136. *MNRAS*, 499, 1918.

Boily, C. M. and Kroupa, P. (2003a). The impact of mass loss on star cluster formation - I. Analytical results. *MNRAS*, 338, 665.

Boily, C. M. and Kroupa, P. (2003b). The impact of mass loss on star cluster formation - II. Numerical N-body integration and further applications. *MNRAS*, 338, 673.

Bonatto, C. and Bica, E. (2006). Methods for improving open cluster fundamental parameters applied to M 52 and NGC 3960. *A&A*, 455, 931.

Bonnell, I. A. and Bate, M. R. (2006). Star formation through gravitational collapse and competitive accretion. *MNRAS*, 370, 488.

Bonnell, I. A., Bate, M. R., Clarke, C. J., and Pringle, J. E. (1997). Accretion and the stellar mass spectrum in small clusters. *MNRAS*, 285, 201.

Bonnell, I. A., Bate, M. R., Clarke, C. J., and Pringle, J. E. (2001). Competitive accretion in embedded stellar clusters. *MNRAS*, 323, 785.

Bonnell, I. A. and Davies, M. B. (1998). Mass segregation in young stellar clusters. *MNRAS*, 295, 691.

Bosch, G., Selman, F., Melnick, J., and Terlevich, R. (2001). The ionising cluster of 30 Doradus. IV. Stellar kinematics. *A&A*, 380, 137.

Bosch, G., Terlevich, E., and Terlevich, R. (2009). Gemini/GMOS Search for Massive Binaries in the Ionizing Cluster of 30 Dor. *AJ*, 137, 3437.

Brandl, B., Sams, B. J., Bertoldi, F., Eckart, A., Genzel, R., Drapatz, S., Hofmann, R., Loewe, M., and Quirrenbach,

A. (1996). Adaptive Optics Near-Infrared Imaging of R136 in 30 Doradus: The Stellar Population of a Nearby Starburst. *ApJ*, 466, 254.

Brands, S. A., de Koter, A., Bestenlehner, J. M., Crowther, P. A., Sundqvist, J. O., Puls, J., Caballero-Nieves, S. M., Abdul-Masih, M., Driessen, F. A., García, M., Geen, S., Gräfener, G., Hawcroft, C., Kaper, L., Keszthelyi, Z., Langer, N., Sana, H., Schneider, F. R. N., Shenar, T., and Vink, J. S. (2022). The R136 star cluster dissected with Hubble Space Telescope/STIS. III. The most massive stars and their clumped winds. *arXiv e-prints*, page arXiv:2202.11080.

Brinkmann, N., Banerjee, S., Motwani, B., and Kroupa, P. (2017). The bound fraction of young star clusters. *A&A*, 600, A49.

Carretta, E., Bragaglia, A., Gratton, R. G., Lucatello, S., Catanzaro, G., Leone, F., Bellazzini, M., Claudi, R., D'Orazi, V., Momany, Y., Ortolani, S., Pancino, E., Piotto, G., Recio-Blanco, A., and Sabbi, E. (2009). Na-O anticorrelation and HB. VII. The chemical composition of first and second-generation stars in 15 globular clusters from GIRAFFE spectra. *A&A*, 505, 117.

Chen, L., de Grijs, R., and Zhao, J. L. (2007). Mass Segregation in Very Young Open Clusters: A Case Study of NGC 2244 and NGC 6530. *AJ*, 134, 1368.

Cignoni, M., Sabbi, E., van der Marel, R. P., Tosi, M., Zaritsky, D., Anderson, J., Lennon, D. J., Aloisi, A., de Marchi, G., Gouliermis, D. A., Grebel, E. K., Smith, L. J., and Zeidler, P. (2015). Hubble Tarantula Treasury Project. II. The Star-formation History of the Starburst Region NGC 2070 in 30 Doradus. *ApJ*, 811, 76.

De Marchi, G., Panagia, N., and Sabbi, E. (2011). Clues to the Star Formation in NGC 346 across Time and Space. *ApJ*, 740, 10.

de Mink, S. E., Pols, O. R., Langer, N., and Izzard, R. G. (2009). Massive binaries as the source of abundance anomalies in globular clusters. *A&A*, 507, L1.

Decressin, T., Meynet, G., Charbonnel, C., Prantzos, N., and Ekström, S. (2007). Fast rotating massive stars and the origin of the abundance patterns in galactic globular clusters. *A&A*, 464, 1029.

D'Ercole, A., Vesperini, E., D'Antona, F., McMillan, S. L. W., and Recchi, S. (2008). Formation and dynamical evolution of multiple stellar generations in globular clusters. *MNRAS*, 391, 825.

di Francesco, J., Sadavoy, S., Motte, F., Schneider, N., Hennemann, M., Csengeri, T., Bontemps, S., Balog, Z., Zavagno, A., André, P., Saraceno, P., Griffin, M., Men'shchikov, A., Abergel, A., Baluteau, J. P., Bernard, J. P., Cox, P., Deharveng, L., Didelon, P., di Giorgio, A. M., Hargrave, P., Huang, M., Kirk, J., Leeks, S., Li, J. Z., Marston, A., Martin, P., Minier, V., Molinari, S., Olofsson, G., Persi, P., Pezzuto, S., Russeil, D., Sauvage, M., Sibthorpe, B., Spinoglio, L., Testi, L., Teyssier, D., Vavrek, R., Ward-Thompson, D., White, G., Wilson, C., and Woodcraft, A. (2010). Small-scale structure in the Rosette molecular cloud revealed by Herschel. *A&A*, 518, L91.

Dib, S. and Henning, T. (2019). Star formation activity and the spatial distribution and mass segregation of dense cores in the early phases of star formation. *A&A*, 629, A135.

Dinnbier, F. and Walch, S. (2020). How fast do young star clusters expel their natal gas? Estimating the upper limit of the gas expulsion time-scale. *MNRAS*, 499, 748.

Domínguez, R., Fellhauer, M., Blaña, M., Farias, J. P., and Dabringhausen, J. (2017). How fast is mass segregation happening in hierarchically formed embedded star clusters? *MNRAS*, 472, 465.

Doran, E. I., Crowther, P. A., de Koter, A., Evans, C. J., McEvoy, C., Walborn, N. R., Bastian, N., Bestenlehner, J. M., Gräfener, G., Herrero, A., Köhler, K., Maíz Apellániz, J., Najarro, F., Puls, J., Sana, H., Schneider, F. R. N., Taylor, W. D., van Loon, J. T., and Vink, J. S. (2013). The VLT-FLAMES Tarantula Survey. XI. A census of the hot luminous stars and their feedback in 30 Doradus. *A&A*, 558, A134.

Ekström, S., Georgy, C., Eggenberger, P., Meynet, G., Mowlavi, N., Wyttenbach, A., Granada, A., Decressin, T., Hirschi, R., Frischknecht, U., Charbonnel, C., and Maeder, A. (2012). Grids of stellar models with rotation. I. Models from 0.8 to 120 $M_{\odot}$ at solar metallicity (Z = 0.014). *A&A*, 537, A146.

Elmegreen, B. G. and Krakowski, A. (2001). A Search for Environmental Influence on Stellar Mass. *ApJ*, 562, 433.

Er, X.-Y., Jiang, Z.-B., and Fu, Y.-N. (2013). Mass segregation of embedded clusters in the Milky Way. *Research in Astronomy and Astrophysics*, 13, 277.

Farias, J. P., Fellhauer, M., Smith, R., Domínguez, R., and Dabringhausen, J. (2018a). Gas expulsion in highly substructured embedded star clusters. *MNRAS*, 476, 5341.

Farias, J. P., Fellhauer, M., Smith, R., Domínguez, R., and Dabringhausen, J. (2018b). Gas expulsion in highly substructured embedded star clusters. *MNRAS*, 476, 5341.

Farias, J. P., Smith, R., Fellhauer, M., Goodwin, S., Candlish, G. N., Blaña, M., and Dominguez, R. (2015). The difficult early stages of embedded star clusters and the importance of the pre-gas expulsion virial ratio. *MNRAS*, 450, 2451.

Farias, J. P., Tan, J. C., and Chatterjee, S. (2017). Star Cluster Formation from Turbulent Clumps. I. The Fast Formation Limit. *ApJ*, 838, 116.

Fellhauer, M. and Kroupa, P. (2005). Star Cluster Survival in Star Cluster Complexes under Extreme Residual Gas Expulsion. *ApJ*, 630, 879.

Ferland, G. J., Chatzikos, M., Guzmán, F., Lykins, M. L., van Hoof, P. A. M., Williams, R. J. R., Abel, N. P., Badnell, N. R., Keenan, F. P., Porter, R. L., and Stancil, P. C. (2017). The 2017 Release Cloudy. *RMxAA*, 53, 385.

Fryxell, B., Olson, K., Ricker, P., Timmes, F. X., Zingale, M., Lamb, D. Q., MacNeice, P., Rosner, R., Truran, J. W., and Tufo, H. (2000). FLASH: An Adaptive Mesh Hydrodynamics Code for Modeling Astrophysical Thermonuclear Flashes. *ApJS*, 131, 273.

Geyer, M. P. and Burkert, A. (2001). The effect of gas loss on the formation of bound stellar clusters. *MNRAS*, 323, 988.

Girichidis, P., Federrath, C., Allison, R., Banerjee, R., and Klessen, R. S. (2012). Importance of the initial conditions for star formation - III. Statistical properties of embedded protostellar clusters. *MNRAS*, 420, 3264.

Goodwin, S. P. (1997). Residual gas expulsion from young globular clusters. *MNRAS*, 284, 785.

Goodwin, S. P. and Whitworth, A. P. (2004). The dynamical evolution of fractal star clusters: The survival of substructure. *A&A*, 413, 929.

Gräfener, G., Vink, J. S., de Koter, A., and Langer, N. (2011). The Eddington factor as the key to understand the winds of the most massive stars. Evidence for a Γ-dependence of Wolf-Rayet type mass loss. *A&A*, 535, A56.

Gutermuth, R. A., Megeath, S. T., Myers, P. C., Allen, L. E., Pipher, J. L., and Fazio, G. G. (2009). A Spitzer Survey of Young Stellar Clusters Within One Kiloparsec of the Sun: Cluster Core Extraction and Basic Structural Analysis. *ApJS*, 184, 18.

Heggie, D. C. (1975). Binary evolution in stellar dynamics. *MNRAS*, 173, 729.

Hillenbrand, L. A. (1997). On the Stellar Population and Star-Forming History of the Orion Nebula Cluster. *AJ*, 113, 1733.

Hillenbrand, L. A. and Hartmann, L. W. (1998). A Preliminary Study of the Orion Nebula Cluster Structure and Dynamics. *ApJ*, 492, 540.

Hills, J. G. (1975). Effect of binary stars on the dynamical evolution of stellar clusters. II. Analytic evolutionary models. *AJ*, 80, 1075.

Hills, J. G. (1980). The effect of mass loss on the dynamical evolution of a stellar system - Analytic approximations. *ApJ*, 235, 986.

Hunter, D. A., Shaya, E. J., Holtzman, J. A., Light, R. M., O'Neil, Earl J., J., and Lynds, R. (1995). The Intermediate Stellar Mass Population in R136 Determined from Hubble Space Telescope Planetary Camera 2 Images. *ApJ*, 448, 179.

Hurley, J. R., Pols, O. R., and Tout, C. A. (2000). Comprehensive analytic formulae for stellar evolution as a function of mass and metallicity. *MNRAS*, 315, 543.

Johnstone, D., Wilson, C. D., Moriarty-Schieven, G., Joncas, G., Smith, G., Gregersen, E., and Fich, M. (2000). Large-Area Mapping at 850 Microns. II. Analysis of the Clump Distribution in the ρ Ophiuchi Molecular Cloud. *ApJ*, 545, 327.

Khorrami, Z., Langlois, M., Vakili, F., Clark, P. C., Buckner, A. S. M., Gonzalez, M., Crowther, P., Wünsch, R., Palouš, J., Boccaletti, A., Lumsden, S., and Moraux, E. (2021). Extreme adaptive optics astrometry of R136. Searching for high proper motion stars. *A&A*, 649, L8.

Kirk, H., Johnstone, D., and Tafalla, M. (2007). Dynamics of Dense Cores in the Perseus Molecular Cloud. *ApJ*, 668, 1042.

Klessen, R. (2001). Star Formation from Turbulent Fragmentation. In Montmerle, T. and André, P., editors, *From Darkness to Light: Origin and Evolution of Young Stellar Clusters*, volume 243 of *Astronomical Society of the Pacific Conference Series*, page 139.

Koenig, X. P., Leisawitz, D. T., Benford, D. J., Rebull, L. M., Padgett, D. L., and Assef, R. J. (2012). Wide-field Infrared Survey Explorer Observations of the Evolution of Massive Star-forming Regions. *ApJ*, 744, 130.

Könyves, V., André, P., Men'shchikov, A., Schneider, N., Arzoumanian, D., Bontemps, S., Attard, M., Motte, F., Didelon, P., Maury, A., Abergel, A., Ali, B., Baluteau, J. P., Bernard, J. P., Cambrésy, L., Cox, P., di Francesco, J., di Giorgio, A. M., Griffin, M. J., Hargrave, P., Huang, M., Kirk, J., Li, J. Z., Martin, P., Minier, V., Molinari, S., Olofsson, G., Pezzuto, S., Russeil, D., Roussel, H., Saraceno, P., Sauvage, M., Sibthorpe, B., Spinoglio, L., Testi, L., Ward-Thompson, D., White, G., Wilson, C. D., Woodcraft, A., and Zavagno, A. (2010). The Aquila prestellar core population revealed by Herschel. *A&A*, 518, L106.

Kroupa, P. (2001). On the variation of the initial mass function. *MNRAS*, 322, 231.

Kroupa, P. (2002). The Initial Mass Function of Stars: Evidence for Uniformity in Variable Systems. *Science*, 295, 82.

Küpper, A. H. W., Maschberger, T., Kroupa, P., and Baumgardt, H. (2011). Mass segregation and fractal substructure in young massive clusters - I. The McLuster code and method calibration. *MNRAS*, 417, 2300.

Lada, C. J., Alves, J., and Lada, E. A. (1996). Near-Infrared Imaging of Embedded Clusters: NGC 1333. *AJ*, 111, 1964.

Lada, C. J. and Lada, E. A. (2003). Embedded Clusters in Molecular Clouds. *ARA&A*, 41, 57.

Larson, R. B. (1982). Mass spectra of young stars. *MNRAS*, 200, 159.

Lee, P. L. and Goodwin, S. P. (2016). Surviving gas expulsion with substructure. *MNRAS*, 460, 2997.

Margulis, M., Lada, C., and Dearborn, D. (1984). The Formation and Early Dynamical Evolution of Open Clusters. In *BAAS*, volume 16, page 409.

Marks, M. and Kroupa, P. (2012). Inverse dynamical population synthesis. Constraining the initial conditions of young stellar clusters by studying their binary populations. *A&A*, 543, A8.

Massey, P. and Hunter, D. A. (1998a). Star Formation in R136: A Cluster of O3 Stars Revealed by Hubble Space Telescope Spectroscopy. *ApJ*, 493, 180.

Massey, P. and Hunter, D. A. (1998b). Star Formation in R136: A Cluster of O3 Stars Revealed by Hubble Space Telescope Spectroscopy. *ApJ*, 493, 180.

Maury, A. J., André, P., Men'shchikov, A., Könyves, V., and Bontemps, S. (2011). The formation of active protoclusters in the Aquila rift: a millimeter continuum view. *A&A*, 535, A77.

McMillan, S., Portegies Zwart, S., van Elteren, A., and Whitehead, A. (2012). Simulations of Dense Stellar Systems with the AMUSE Software Toolkit. In Capuzzo-Dolcetta, R., Limongi, M., and Tornambè, A., editors, *Advances in Computational Astrophysics: Methods, Tools, and Outcome*, volume 453 of *Astronomical Society of the Pacific Conference Series*, page 129.

McMillan, S. L. W., Vesperini, E., and Portegies Zwart, S. F. (2007). A Dynamical Origin for Early Mass Segregation in Young Star Clusters. *ApJL*, 655, L45.

Megeath, S. T., Gutermuth, R., Muzerolle, J., Kryukova, E., Hora, J. L., Allen, L. E., Flaherty, K., Hartmann, L., Myers, P. C., Pipher, J. L., Stauffer, J., Young, E. T., and Fazio, G. G. (2016). The Spitzer Space Telescope Survey of the Orion A and B Molecular Clouds. II. The Spatial Distribution and Demographics of Dusty Young Stellar Objects. *AJ*, 151, 5.

Murray, N. (2011). Star Formation Efficiencies and Lifetimes of Giant Molecular Clouds in the Milky Way. *ApJ*, 729, 133.

Murray, S. D. and Lin, D. N. C. (1996). Coalescence, Star Formation, and the Cluster Initial Mass Function. *ApJ*, 467, 728.

Palla, F., Randich, S., Flaccomio, E., and Pallavicini, R. (2005). Age Spreads in Star-forming Regions: The Lithium Test in the Orion Nebula Cluster. *ApJL*, 626, L49.

Palla, F., Randich, S., Pavlenko, Y. V., Flaccomio, E., and Pallavicini, R. (2007). Old Stars in Young Clusters: Lithium-depleted Low-Mass Stars of the Orion Nebula Cluster. *ApJL*, 659, L41.

Parker, R. J. and Goodwin, S. P. (2015). Comparisons between different techniques for measuring mass segregation. *MNRAS*, 449, 3381.

Parker, R. J., Goodwin, S. P., Wright, N. J., Meyer, M. R., and Quanz, S. P. (2016). Mass segregation in star clusters is not energy equipartition. *MNRAS*, 459, L119.

Parker, R. J., Wright, N. J., Goodwin, S. P., and Meyer, M. R. (2014). Dynamical evolution of star-forming regions. *MNRAS*, 438, 620.

Parmentier, G. and Pfalzner, S. (2013). Local-density-driven clustered star formation. *A&A*, 549, A132.
Pavlík, V., Kroupa, P., and Šubr, L. (2019). Do star clusters form in a completely mass-segregated way? *A&A*, 626, A79.
Pellegrini, E. W., Baldwin, J. A., Brogan, C. L., Hanson, M. M., Abel, N. P., Ferland, G. J., Nemala, H. B., Shaw, G., and Troland, T. H. (2007). A Magnetically Supported Photodissociation Region in M17. *ApJ*, 658, 1119.
Pellegrini, E. W., Baldwin, J. A., and Ferland, G. J. (2011a). Structure and Feedback in 30 Doradus. II. Structure and Chemical Abundances. *ApJ*, 738, 34.
Pellegrini, E. W., Baldwin, J. A., and Ferland, G. J. (2011b). Structure and Feedback in 30 Doradus. II. Structure and Chemical Abundances. *ApJ*, 738, 34.
Pellegrini, E. W., Baldwin, J. A., Ferland, G. J., Shaw, G., and Heathcote, S. (2009). Orion's Bar: Physical Conditions Across the Definitive $H^+/H^0/H_2$ Interface. *ApJ*, 693, 285.
Pelupessy, F. I., van Elteren, A., de Vries, N., McMillan, S. L. W., Drost, N., and Portegies Zwart, S. F. (2013). The Astrophysical Multipurpose Software Environment. *A&A*, 557, A84.
Pfalzner, S., Kirk, H., Sills, A., Urquhart, J. S., Kauffmann, J., Kuhn, M. A., Bhandare, A., and Menten, K. M. (2016). Observational constraints on star cluster formation theory. I. The mass-radius relation. *A&A*, 586, A68.
Plummer, H. C. (1911). On the problem of distribution in globular star clusters. *MNRAS*, 71, 460.
Raboud, D. and Mermilliod, J. C. (1998). Evolution of mass segregation in open clusters: some observational evidences. *A&A*, 333, 897.
Rahner, D., Pellegrini, E. W., Glover, S. C. O., and Klessen, R. S. (2017). Winds and radiation in unison: a new semi-analytic feedback model for cloud dissolution. *MNRAS*, 470, 4453.
Rahner, D., Pellegrini, E. W., Glover, S. C. O., and Klessen, R. S. (2019). WARPFIELD 2.0: feedback-regulated minimum star formation efficiencies of giant molecular clouds. *MNRAS*, 483, 2547.
Sabbi, E., Lennon, D. J., Gieles, M., de Mink, S. E., Walborn, N. R., Anderson, J., Bellini, A., Panagia, N., van der Marel, R., and Maíz Apellániz, J. (2012). A Double Cluster at the Core of 30 Doradus. *ApJL*, 754, L37.
Schmeja, S., Kumar, M. S. N., and Ferreira, B. (2008). The structures of embedded clusters in the Perseus, Serpens and Ophiuchus molecular clouds. *MNRAS*, 389, 1209.
Selman, F., Melnick, J., Bosch, G., and Terlevich, R. (1999). The ionizing cluster of 30 Doradus. III. Star-formation history and initial mass function. *A&A*, 347, 532.
Shukirgaliyev, B., Parmentier, G., Berczik, P., and Just, A. (2017). Impact of a star formation efficiency profile on the evolution of open clusters. *A&A*, 605, A119.
Shukirgaliyev, B., Parmentier, G., Berczik, P., and Just, A. (2020). Star Clusters in the Galactic tidal field, from birth to dissolution. In Bragaglia, A., Davies, M., Sills, A., and Vesperini, E., editors, *IAU Symposium*, volume 351 of *IAU Symposium*, pages 507–511.
Shukirgaliyev, B., Parmentier, G., Just, A., and Berczik, P. (2018). The Long-term Evolution of Star Clusters Formed with a Centrally Peaked Star Formation Efficiency Profile. *ApJ*, 863, 171.
Silich, S. and Tenorio-Tagle, G. (2017). Gas expulsion versus gas retention: what process dominates in young massive clusters? *MNRAS*, 465, 1375.
Smith, R., Fellhauer, M., Goodwin, S., and Assmann, P. (2011). Surviving infant mortality in the hierarchical merging scenario. *MNRAS*, 414, 3036.
Townsley, L. K., Broos, P. S., Feigelson, E. D., Garmire, G. P., and Getman, K. V. (2006). A Chandra ACIS Study of 30 Doradus. II. X-Ray Point Sources in the Massive Star Cluster R136 and Beyond. *AJ*, 131, 2164.
Tutukov, A. V. (1978). Early Stages of Dynamical Evolution of Star Cluster Models. *A&A*, 70, 57.
Vinkó, J., Sárneczky, K., Balog, Z., Immler, S., Sugerman, B. E. K., Brown, P. J., Misselt, K., Szabó, G. M., Csizmadia, S., Kun, M., Klagyivik, P., Foley, R. J., Filippenko, A. V., Csák, B., and Kiss, L. L. (2009). The Young, Massive, Star Cluster Sandage-96 After the Explosion of Supernova 2004dj in NGC 2403. *ApJ*, 695, 619.
Walborn, N. R. and Blades, J. C. (1997). Spectral Classification of the 30 Doradus Stellar Populations. *ApJS*, 112, 457.
Wall, J. E., McMillan, S. L. W., Mac Low, M.-M., Klessen, R. S., and Portegies Zwart, S. (2019). Collisional N-body Dynamics Coupled to Self-gravitating Magnetohydrodynamics Reveals Dynamical Binary Formation. *ApJ*, 887, 62.

Wang, L., Spurzem, R., Aarseth, S., Nitadori, K., Berczik, P., Kouwenhoven, M. B. N., and Naab, T. (2015). NBODY6++GPU: ready for the gravitational million-body problem. *MNRAS*, 450, 4070.

Wang, P., Li, Z.-Y., Abel, T., and Nakamura, F. (2010). Outflow Feedback Regulated Massive Star Formation in Parsec-Scale Cluster-Forming Clumps. *ApJ*, 709, 27.

Whitmore, B. C., Zhang, Q., Leitherer, C., Fall, S. M., Schweizer, F., and Miller, B. W. (1999). The Luminosity Function of Young Star Clusters in "the Antennae" Galaxies (NGC 4038-4039). *AJ*, 118, 1551.

Wright, N. J., Parker, R. J., Goodwin, S. P., and Drake, J. J. (2014). Constraints on massive star formation: Cygnus OB2 was always an association. *MNRAS*, 438, 639.

Yu, J., de Grijs, R., and Chen, L. (2011). Rapid Dynamical Mass Segregation and Properties of Fractal Star Clusters. *ApJ*, 732, 16.

Zinnecker, H. (1982). Prediction of the protostellar mass spectrum in the Orion near-infrared cluster. *Annals of the New York Academy of Sciences*, 395, 226.